

DMIC FILE COPY

AD-A167 360

DTNSRDC-ASED-CR-C2-86

20000801165

**Wind Tunnel Test of
the Modified Goldschmied Model
with Propulsion and Empennage:
Analysis of Test Results**

Fabio R. Goldschmied, P.E.
1782 McClure Road
Monroeville, PA 15146

1 February 1986

Final Report for Period 3 March 1981–30 November 1982

Approved for public release; distribution is unlimited.

Prepared for:

David W. Taylor Naval Ship R&D Center
Aviation and Surface Effects Department
Bethesda, MD 20084-5000

DTIC
ELECTED
S D
MAY 1 1986
A

**Reproduced From
Best Available Copy**

86 4 30 050

UNCLASSIFIED

SECURITY CLASSIFICATION OF THIS PAGE

REPORT DOCUMENTATION PAGE

1a REPORT SECURITY CLASSIFICATION UNCLASSIFIED		1b RESTRICTIVE MARKINGS			
2a SECURITY CLASSIFICATION AUTHORITY		3 DISTRIBUTION/AVAILABILITY OF REPORT APPROVED FOR PUBLIC RELEASE; DISTRIBUTION IS UNLIMITED.			
2b DECLASSIFICATION/DOWNGRADING SCHEDULE					
4 PERFORMING ORGANIZATION REPORT NUMBER(S) FRG-82-1		5 MONITORING ORGANIZATION REPORT NUMBER(S) DTNSRDC/ASED-CR-02-86			
6a NAME OF PERFORMING ORGANIZATION Fabio R. Goldschmied P.E.	6b OFFICE SYMBOL (if applicable)	7a NAME OF MONITORING ORGANIZATION David W. Taylor Naval Ship R&D Center Code 1603			
6c ADDRESS (City, State, and ZIP Code) 1782 McClure Road Monroeville, PA 15146		7b ADDRESS (City, State, and ZIP Code) Bethesda, MD 20084-5000			
8a NAME OF FUNDING/SPONSORING ORGANIZATION	8b OFFICE SYMBOL (if applicable)	9 PROCUREMENT INSTRUMENT IDENTIFICATION NUMBER N-00167-81-C-0075			
8c ADDRESS (City, State, and ZIP Code)		10 SOURCE OF FUNDING NUMBERS			
		PROGRAM ELEMENT NO	PROJECT NO	TASK NO	WORK UNIT ACCESSION NO
11 TITLE (Include Security Classification) Wind Tunnel Test of the Modified Goldschmied Model with Propulsion and Empennage: Analysis of Test Results					
12 PERSONAL AUTHOR(S) Fabio R. Goldschmied					
13a TYPE OF REPORT Final	13b TIME COVERED FROM 3/3/81 TO 11/30/82	14 DATE OF REPORT (Year, Month, Day) 1986, February		15 PAGE COUNT 114	
16 SUPPLEMENTARY NOTATION					
17 COSATI CODES		18 SUBJECT TERMS (Continue on reverse if necessary and identify by block number) Aerodynamics Boundary-layer Control Hydrodynamics Jet Propulsion Wind Tunnel Testing			
19 ABSTRACT (Continue on reverse if necessary and identify by block number) An extensive test program was carried out in the 8x10 low-speed wind-tunnel of DTNSRDC for the experimental verification of the integrated hull/BLC/propulsion vehicle design concept. The 1957 Goldschmied wind-tunnel model was overhauled with a new suction-slot inlet configuration, a suction/propulsion fan, a new aftbody and a tailboom/empennage assembly. The fan air power coefficient of the operational model with empennage ranged in steady flight from 0.0130 (free transition) to 0.0155 (transition tripped at 10% length) at the volume Reynolds number of two millions. Also considerable excess thrust could be generated with an average incremental propulsive efficiency of 72%.					
(Continued on reverse side)					
20 DISTRIBUTION AVAILABILITY OF ABSTRACT <input checked="" type="checkbox"/> UNCLASSIFIED UNLIMITED <input type="checkbox"/> SAME AS RPT <input type="checkbox"/> DTIC USERS		21 ABSTRACT SECURITY CLASSIFICATION UNCLASSIFIED			
22a NAME OF RESPONSIBLE INDIVIDUAL Benjamin J. Neumann		22b TELEPHONE (Include Area Code) (202) 227-1177		22c OFFICE SYMBOL 1603	

UNCLASSIFIED

SECURITY CLASSIFICATION OF THIS PAGE

BLC

(Block 19 continued)

As compared to wind-tunnel tests of conventional streamlined bodies with empennage at exactly the same volume Reynolds number, the integrated design offers 50% less equivalent drag for both free and tripped transitions.

The empennage provided neutral static stability over the complete test range of 8 degrees; the ratio of total fin planform over volume equivalent was 0.404. It was found that efficient and stable boundary-layer control could only be achieved by the combination of Ringloeb cusp at the slot's leading-edge with suction flow and with the presence of the tailboom.

The fan (or pump) design is an essential part of the system design: a procedure was developed for the determination of the optimum fan design parameters from the vehicle's wind-tunnel test data. As an example, a tested NACA axial rotor/stator stage could be employed with 93% adiabatic efficiency for the vehicle with empennage and tripped transition.

Finally, it is of fundamental interest that the basic body, without empennage and with free transition, was observed in steady flight with a jet total-pressure equal to free-stream's and a jet velocity ratio of 0.675 over free-stream velocity.

Hypersonic Aerodynamics
Hypodynamics, Jet propulsion

UNCLASSIFIED

SECURITY CLASSIFICATION OF THIS PAGE

REPORT FRG-82-1

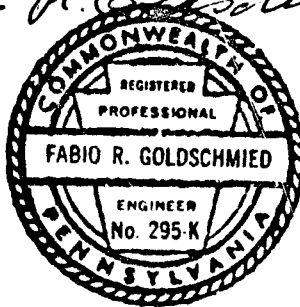
WIND TUNNEL TEST OF THE MODIFIED GOLDSCHMIED MODEL WITH
PROPELLION AND EMPENNAGE : ANALYSIS OF TEST RESULTS

FABIO R. GOLDSCHMIED

FEBRUARY 1, 1982

The views and conclusions contained in this document are those of the author and should not be interpreted as necessarily representing the official policies, either expressed or implied, of the U.S. Government.

Fabio R. Goldschmied



FABIO R. GOLDSCHMIED P.E.

1782 McCLORE ROAD

MONROEVILLE PA 15146

Accession For	
NTIS GRA&I	<input checked="" type="checkbox"/>
DTIC TAB	<input type="checkbox"/>
Unannounced	<input type="checkbox"/>
Justification	
By _____	
Distribution/ _____	
Availability Codes _____	
Dist	Avail and/or Special
A1	

TABLE OF CONTENTS

	Page
SUMMARY	iii
LIST OF TABLES	v
LIST OF FIGURES	vi
NOMENCLATURE	x
I - INTRODUCTION	1
II - TEST PROGRAM	4
III - ANALYSIS OF FAN AIR POWER COEFFICIENTS	7
IV - YAWING MOMENTS ANALYSIS	17
V - CORRELATION OF FAN COEFFICIENTS AND SELECTION OF FAN DESIGN PARAMETERS	20
VI - ANALYSIS OF BOUNDARY-LAYER CONTROL PARAMETERS	26
VII - ANALYSIS OF PROPULSION JET	31
VIII - PRELIMINARY ANALYSIS OF ERNATE CONFIGURATIONS	35
IX - CONCLUSIONS AND RECOMMENDATIONS	43
REFERENCES	45

SUMMARY

An extensive wind-tunnel program (over 800 test points) was carried out in the 8 x 10 Low-speed facility of the David Taylor Naval Ship R&D Center for the experimental verification of the integrated hull/boundary-layer control/propulsion/empennage vehicle design concept.

The 1957 Goldschmied model was overhauled with new slot inlet configuration, suction/propulsion fan, new aftbody and tailboom/empennage assembly.

The fan air power coefficient of the operational model with empennage ranges from 0.0130 (free-transition) to 0.0155 (transition tripped at 10% length) at the volume Reynolds number of 2 millions. It was found that considerable excess thrust can be generated with an average 72% propulsive efficiency.

As compared to wind-tunnel tests of conventional streamlined bodies at exactly the same volume Reynolds number, the integrated vehicle design requires ~50% less power for both free-transition and tripped transition cases.

The boundary-layer control mechanism, necessary to overcome the pressure-step at 86% length, has been thoroughly analyzed; it has been found that three elements are required to achieve both efficient and stable boundary-layer control: the Ringloeb cusp at the slot leading-edge, the slot suction flow, and finally, the tailboom. Correlations have been developed between the boundary-layer Reynolds number, the minimum slot suction flow coefficient for full aftbody attachment and the slot inlet total-pressure loss ratio.

The propulsion jet has been carefully analyzed: the jet velocity ratio over free-stream velocity ranges from 0.675 to 0.767,

the jet total-pressure ratio over free-stream dynamic pressure ranges from approximately 1.00 to 1.16 and the jet-discharge static-pressure coefficient ranges from 0.505 to 0.715. Of particular significance is the free-transition body without empennage, which has been observed to fly in steady-state with a jet velocity ratio of 0.675 and a jet total-pressure ratio of approximately 1.0: this demonstrates the basic meaning of aerodynamic integration.

The cruciform empennage provided exactly neutral static stability with an average tan air power coefficient increment of only 0.0019 and with a total fin planform area ratio of 0.404 over volume equivalent. As compared to the conventional empennage of streamlined bodies, the power saving is over 46%.

Since the vehicle design cannot be completed without the fan (or pump) design, a procedure has been developed for the selection of the best fan design parameters from the vehicle coefficients. A new fan speed parameter has been defined, relating fan RPM, free-stream velocity and hull volume. As an example, a fan has been selected for the operational model with empennage and with tripped transition from a tested NACA axial rotor/stator stage with 93.5% adiabatic efficiency.

A preliminary analysis of alternate configurations has been carried out, exploring the effect of increasing the fineness ratio with constant-pressure Reichardt-type forebodies. It appears that the 7.5 fineness ratio vehicle would need only 72% slot suction flow and therefore much lower fan air power, as compared to the present 2.70 fineness ratio vehicle of equal volume at the same speed.

LIST OF TABLES

- I — Summary of Test Configurations
- II — Fan Air Power Coefficients
- III — Thrust Efficiency Summary
- IV — Air Power Contribution of Empennage at $\alpha = 0^\circ$
- V — Fan Design Parameters
- VI — Experimental Fan Performance
- VII — Summary of Slot Pressure Steps
- VIII — Summary of Zero Axial Force Suction Flow Coefficients
- IX — Summary of Jet Static-Pressure Coefficients
- X — Allowable Range of Flow Coefficients
- XI — Jet Velocity Ratio and Total-Pressure Ratio
- XII — Geometrical Coordinates of Body CD8 (Case 1 of Ref. 19)
- XIII — Geometrical Coordinates of Body R8 (Case 4 of Ref. 19)
- XIV — Geometrical Coordinates of Body R4 (Case 8 of Ref. 19)
- XV. — Summary of Suction Flow Parameters

LIST OF FIGURES

1. Survey of Vehicle Total Power Coefficients
2. Photo of 1957 Forebody on Vertical Strut
3. Photo of Intermediate Hull Section with Central Ring Assembly
and Fan Inlet Flare
4. Photo of Intermediate Hull Section Attached to Forebody
5. Photo of Dynamic Air Engineering Inc. Suction/Propulsion Fan
6. Photo of Fan Installed in Central Ring, with Intermediate Hull
Section Attached to Forebody
7. Photo of Jet Discharge Nozzle Assembly
8. Photo of Jet Discharge Nozzle Mounted on Fan; Fan Installed in
Central Ring, with Intermediate Hull Section Attached to Forebody
9. Photo of End Section of Hull, Showing Sharp Edge of Ringloeb Cusp
10. Photo of Installation of End Section of Hull
11. Photo of Open-Jet Aftbody
12. Starboard Photo View of Complete Test Model with Open-Jet Aftbody
(Configuration 0)
13. Stern Photo View of Complete Test Model with Open-Jet Aftbody
(Configuration 0)
14. Photo of Wind-Tunnel Installation of Test Model with Open-Jet Aftbody
(Configuration 0)
15. Photo of Wind-Tunnel Installation of Test Model with Tailboom Aftbody
(Configuration 1)

16. Photo of Wind-Tunnel Installation of Test Model with Tailboom Aftbody and Empennage (Configuration 2), Showing also the Wake-Rake Assembly
17. Bow Photo View of Wind-Tunnel Installation of Test Model with Transition Trip at 10% Length, Showing also Wake-Rake Assembly
18. Photo of Wake-Rake Assembly
19. Fan Air Power Coefficient Vs. Axial Force Coefficient - Configuration 00
20. Fan Air Power Coefficient Vs. Axial Force Coefficient - Configuration 50
21. Fan Air Power Coefficient Vs. Axial Force Coefficient - Configuration 10
22. Fan Air Power Coefficient Vs. Axial Force Coefficient - Configuration 01
23. Fan Air Power Coefficient Vs. Axial Force Coefficient - Configuration 51
24. Fan Air Power Coefficient Vs. Axial Force Coefficient - Configuration 11
25. Fan Air Power Coefficient Vs. Axial Force Coefficient - Configuration 02
26. Fan Air Power Coefficient Vs. Axial Force Coefficient - Configuration 52
27. Fan Air Power Coefficient Vs. Axial Force Coefficient - Configuration 12
28. Fan Air Power Coefficient Vs. Axial Force Coefficient - Configurations 60 and 61
29. Fan Air Power Coefficient Vs. Volume Reynolds Number - Configurations 00, 01 and 02 (Free Transition)
30. Fan Air Power Coefficient Vs. Volume Reynolds Number - Configurations 50, 51 and 52 (Transition at 58% Length)
31. Fan Air Power Coefficient Vs. Volume Reynolds Number - Configurations 10, 11 and 12 (Transition at 10% Length)
32. Fan Air Power Coefficient Vs. Volume Reynolds Number - Configurations 02, 52 and 12 (Model with Empennage)
33. Correlation of Yawing Moment Coefficient at $\alpha = 3^\circ$ with Slot Suction Coefficient - Configurations 11 and 12

34. Correlation of Yawing Moment Coefficient at $\alpha = 6^\circ$ with Slot Suction Coefficient - Configurations 11 and 12
35. Correlation of Yawing Moment Coefficient at $\alpha = 8^\circ$ with Slot Suction Coefficient - Configurations 11 and 12
36. Correlation of Yawing Moment Coefficient with Angle of Attack - Configurations 11 and 12
37. Correlation of Slot Suction Flow with Fan Air Power
38. Correlation of Slot Suction Flow with Fan Pressure Rise
39. Chart of Fan Design Parameters - Selection of Operating Point
40. Experimental Performance of NACA Axial Stage
41. Photo of Experimental NACA Rotor
42. Correlation of Slot Pressure-Step with Suction Flow - Configurations 00 and 01
43. Correlation of Slot Pressure-Step with Suction Flow - Configurations 01 and 11
44. Correlation of Slot Pressure-Step with Suction Flow - Configurations 02 and 12
45. Correlation of Minimum Full-Attachment Suction Parameter with Boundary-Layer Reynolds Number
46. Correlation of Slot-Inlet Pressure-Loss Ratio at the Minimum Full-Attachment Suction with Boundary-Layer Reynolds Number
47. Correlation of Jet Static-Pressure Coefficient with Slot Pressure-Step - Configurations 00 and 10
48. Correlation of Jet Static-Pressure Coefficient with Slot Pressure-Step - Configurations 01 and 11

49. Correlation of Jet Static-Pressure Coefficient with Slot Pressure-Step - Configurations 02 and 12
50. Correlation of Jet Velocity-Ratio with Jet Total-Pressure Ratio - Configurations 01, 11, 02 and 12
51. Plot of Boundary-Layer Control Suction Parameter Vs. Slot Velocity Ratio - Two-Dimensional Taylor Theory
52. Correlation of Estimated Suction Parameters with Fineness Ratio for Reichardt Forebodies
53. Correlation of Suction and Power Coefficients with Fineness Ratio for Reichardt Forebodies

NOMENCLATURE

A = Cross-sectional Area of Body

AF = Tail Area - Total Planform Area of All Fins

AR = b^2/AF = Tail Aspect Ratio

b = Tail Fin Span

c₁ = Fin Tip Chord

c₂ = Fin Root Chord

C_D = Drag Coefficient

CQ = $Q/U_0 V^{0.66}$ = Suction Flow Coefficient

CQ₅ = Suction Flow Coefficient (Flow measured at Sta. 5)

CS = $Q/U_1 \delta_1 V^{0.33}$ = Slot Suction Parameter

C_θ = $Q/2\pi r_1 U_1 \theta_1$ = Boundary-Layer Control Parameter

CH = P/q = Total-Pressure Coefficient

CH₂₅ = $\Delta P_{25}/q$ = Total-Pressure Differential between Sta. 5 and 2

CH₁₂ = $\Delta P_{12}/q$ = Total-Pressure Differential between Sta. 2 and 1

CHP₂₅ = CQ₅ × CH₂₅ = Fan Air Power Coefficient between Sta. 5 and 2

CP = Static-Pressure Coefficient

CP₅ = Static-Pressure Coefficient at Jet Discharge (Sta. 5)

ΔCP = Static-Pressure Differential across Slot

CY = MY/qV = Experimental Yawing Moment Coefficient

D = Maximum Body Diameter

D₀ = Fan Diameter

D₅ = Jet Diameter (Sta. 5)

$F = L/D$ = Fineness Ratio
 H_5 = Jet Total-Pressure (Sta. 5)
 $KV = V/\pi R^2 L$ = Prismatic Coefficient
 L = Body Length
 L_1 = Body Length up to Suction Slot
 MY = Experimental Yawing Moment about Strut Axis
 n = Fan Speed, RPS
 P = Fan Pressure
 $q = \frac{1}{2} \rho U_0^2$ = Free-Stream Dynamic Pressure
 Q = Suction Flow
 Q_5 = Suction Flow Measured at Sta. 5
 r = Body Radius at Axial Location x
 r_1 = Body Radius at Suction Slot
 R = Maximum Body Radius
 $R_\delta = U_1 \delta_1 / v$ = Boundary-Layer Reynolds Number
 $R_L = U_0 L / v$ = Length Reynolds Number
 $R_V = U_0 V^{0.33} / v$ = Volume Reynolds Number
 t = Tailboom Length
 $u = \pi D_0 n$ = Fan Tip Speed
 U_0 = Free-Stream Velocity
 U_1 = Velocity Upstream of Suction Slot at Sta. 1
 U_6 = Velocity Downstream of Suction Slot
 U_5 = Velocity of Jet Discharge at Sta. 5
 V = Body Useful Volume
 W = Fan Weight Flow

α = Angle of Attack or Yaw
 δ_1 = Boundary-Layer Thickness at Sta. 1
 η = Efficiency
 θ_1 = Boundary-Layer Momentum Thickness at Sta. 1
 Λ = Angle of Sweep of Tail Fins
 μ = Ratio of Inlet Fan Pressure to std. NACA atm
 ν = Kinematic Viscosity of Free-Stream Flow
 ζ = Ratio of Inlet Fan Total-Temperature to std. NACA atm
 ρ = Mass Density of Free-Stream Flow
 σ = $U_0/n\nu^{0.33}$ = Fan Speed Parameter
 ϕ = $0.405Q/D_0^3n$ = Fan Flow Parameter
 ψ = $0.203P/\rho D_0^2n^2$ = Fan Total-Pressure Parameter

NOTE: All pressure symbols refer to gauge pressure.

I - INTRODUCTION

An investigation of an engine/airframe, propulsion/BLC/hull design synthesis was proposed in 1954 by Goldschmied (1) to ONR for airship application. The inviscid body design and the boundary-layer control analysis were performed in 1954 under ONR Contract N0nr 1412(00)L1; propulsion was not yet considered in detail. This work is reported in Ref. 2. Later a wind-tunnel model was designed and built, and in 1956 a series of wind-tunnel tests was performed at the David W. Taylor Model Basin, at length Reynolds numbers up to 1.2×10^7 , comparing the new design directly with a conventional airship hull. The experimental results have been reported by Cerreta (3) in 1957.

An extensive review of the wind-tunnel test data and a new propulsion analysis were undertaken by Goldschmied in 1965-66 as personal research at the University of Utah. This work was presented at the Second Joint Propulsion Conference in 1966 and was later published as the first paper in the new AIAA Journal of Hydronautics in 1967 (4).

In 1969 a new series of wind-tunnel tests was undertaken under Contract 5253(62-2332)69R with the specific goal of developing an under-water vehicle with minimum installed power; the 1957 wind-tunnel model was refurbished, better instrumentation was added and a variety of suction slot inlet configurations was tested at angles of attack up to 6° . Unfortunately, the funding was terminated before propulsion could be installed in the test model, despite very promising results with substantial improvements over the 1957 test. The test results were reported in 1977 (5).

After 1970, extensive theoretical work was carried out for the optimization of simple streamlined shapes of given volume at specified speeds, over a wide range of Reynolds numbers. This work was published

by Parsons, Goodson and Goldschmied (6) in 1974; it was shown that very little drag gains could be made for bodies with all-turbulent boundary-layers and with realistic pressure recovery on the aftbody, according to the criterion of Ref. 20.

In 1976 Goldschmied made a presentation on vehicle system design for total propulsion power optimization at the Rand Low-Speed Boundary-Layer Transition Workshop (7) and in 1977 he presented an overview on LTA power optimization at the LTA Technology Conference (8).

Later, a study was carried out on the potential of passive BLC for high-altitude LTA application and it was published in 1978 (9); the Ringloeb cusp was used for the passive BLC means and some good experimental evidence was culled from the 1957 data (3) and from the 1969 data (5).

The key point still remained that the complete power integration with self-propulsion had not been demonstrated experimentally and negative arguments could still be made by critics.

To establish the conventional state-of-the-art, in Fig. 1 there is plotted the total power coefficient of the vehicle with empennage fins and propulsion vs. length Reynolds number. As indicated, the drag increment of the fins (adequate for dynamic stability only) is taken to be 0.003 and the propulsive efficiency is taken to be 85% for all cases. It can be seen that the worst case is the torpedo; the next is the 4.2:1 tripped airship, followed by the tripped Model 4176. The best is the theoretically optimized X-35 laminar body of Parsons, Goodson and Goldschmied (6). The Hess optimized turbulent body was derived by Hess (10)(11) while the I-36 optimized turbulent body was derived by Parsons, Goodson and Goldschmied (6). The "Dolphin" point is experimental, as reported by Carmichael (12). The two Goldschmied points are shown, indicating the total power coefficient as predicted from the available wind-tunnel test data without self-propulsion. It can be observed that the tripped point requires only 50% of the power of the Hess optimized turbulent body and only 33% of the torpedo power; the free-transition point requires less power than the theoretical X-35 laminar body (6).

At this point in the technological development, the Advanced Fluid Dynamic Research (AFDR) Program was funded by DARPA to demonstrate the feasibility of developing low installed-power vehicles for a broad spectrum of operational underseas missions, where laminar boundary-layers would not be practical. In 1981 a sphere with a single suction slot for BLC was successfully tested in the 8 ft × 10 ft Low-speed Wind-tunnel at DTNSRDC for several transition locations and with three slot widths; the experimental work was reported by Leitner and McCabe (13). The suction slot was placed at 135° from the nose, on the basis of a boundary-layer analysis carried out by the Goldschmied engineering office. As in the past, self-propulsion was not provided in the sphere test model. The BLC suction and the drag coefficients were in good agreement with the theoretical predictions.

The Goldschmied engineering office was tasked by DTNSRDC under Contract N-00167-80-M-4800 to analyze the 1957 and 1969 test data and to redesign the 1957 test model so as to incorporate the 1969 suction slot inlet improvements and so as to install a self-propulsion fan and an empennage adequate for neutral static stability.

The complete integration of hull design, boundary-layer control, propulsion and empennage could then be demonstrated experimentally in the wind-tunnel and dispel any doubts.

Following the completion of the analysis and redesign, the Goldschmied engineering office was tasked under Contract N-00167-81-C-0075 to carry out the detailed mechanical design and the fabrication of the model modifications, including the fan procurement and installation. Additional tasks included analysis of the test results and preliminary design of alternate configurations.

II - TEST PROGRAM

The test program was quite extensive as it comprised over 800 test points, organized in 86 test runs. Three configurations were tested, each with free transition, with transition tripped at 58% length (hull maximum diameter location) and with transition tripped at 10% length.

The first configuration, termed 0, followed the best 1969 slot design and aftbody contour, with the aftbody terminated at the axial location which would yield the required stern jet diameter D_5 . The free transition configuration was termed 00, the 58% trip configuration was termed 50 and 10% trip configuration was termed 10. In Fig. 2 there are shown two photos of the stripped 1957 forebody mounted on the vertical strut; this is the starting point of the reconstruction of the test model. It can be pointed out that this old forebody was far from the gleaming polished condition which is required for laminar flow: the aluminum skin was eroded, corroded and also dented.

In Fig. 3 there is shown the photo of the next item to be assembled, i.e. the intermediate hull section with the central ring assembly and fan inlet flare; the ring is used to support the fan, the jet nozzle and the aftbody assemblies.

Figure 4 shows a photo of the forebody and intermediate hull section together; also to be noticed is the Scanivalve mounting bracket. Figure 5 shows a photo of the 6" dia. suction/propulsion fan; this fan is manufactured by Dynamic Air Engineering, Inc. as Model M5862AP-6A with two rotors, each with two blades, running at 11,700 RPM. At peak efficiency the performance is as follows:

$Q = 700 \text{ CFM}$	Flow
$P = 9.5 \text{ " WG}$	Total-Pressure
$n = 52\%$	Total-Efficiency.

It was found experimentally that flow straighteners had to be added both upstream and downstream in order to obtain approximately the rated performance. Figure 6 shows a photo of the fan installed in the central ring. The next item is the jet discharge nozzle, as shown in Fig. 7; to be noted is the extensive pressure instrumentation carried by this assembly. In Fig. 8 there is shown a photo of the discharge nozzle mounted on the fan, which in its turn is installed in the central ring; to be noted are the three pressure rakes mounted at the discharge of the nozzle. In Fig. 9 there is shown a photo of the end section of the hull; the sharp edge of the Ringloeb cusp can be readily seen. It can be noted that in the 1969 tests this cusp was modeled with clay and that the edge, therefore, was anything but sharp. In Fig. 10 there is shown a photo of this end hull section as assembled in the test model.

Finally, in Fig. 11 there is shown a photo of the aftbody which is the last item for the assembly of Configuration 0. Figure 12 shows the photo of the starboard view of Configuration 0 in the shop, while Fig. 13 shows the photo of the stern view. Figure 14 shows the photo of the wind-tunnel installation of Configuration 0.

The second configuration, termed 1, had a different aftbody. The free transition configuration was termed 01, the 58% trip configuration was termed 51 and the 10% trip configuration was termed 11. Figure 15 shows the photo of the wind-tunnel installation of Configuration 1: it can be seen that the suction-slot trailing-edge is slightly different and that a thin tailboom (supported by four vanes) is mounted at the jet exit.

The third configuration, termed 2, had the second aftbody and a tailboom/empennage assembly. The free transition configuration was termed 02, the 58% trip configuration was termed 52 and the 10% trip configuration was termed 12. Figure 16 shows a photo of Configuration 2, where the wake-rake installation can also be seen; the tip-to-tip empennage span equals the hull's maximum diameter, following the DTNSRDC design constraint, while the tailboom length is half the hull's maximum diameter.

To conclude the photographic presentation of the test model, Fig. 17 shows the photo of the bow view of the test model, showing the roughness strip at 10% length for transition trip, with the wake-rake in the background. Finally, Fig. 18 presents a detailed photo of the wake-rake employed in this wind-tunnel test program.

A summary table of the eleven test configurations is presented below:

TABLE I - SUMMARY OF TEST CONFIGURATIONS

Conf. #	Transition % Length	Aftbody Design	Tailboom and Empennage	Ringloeb Cusp at Slot L.E.	B.L.C. Components
00	Free	Original	No	Yes	Cusp & Suction
50	58%	Original	No	Yes	Cusp & Suction
10	10%	Original	No	Yes	Cusp & Suction
01	Free	New	No	Yes	Cusp & Suction
51	58%	New	No	Yes	Cusp & Suction
11	10%	New	No	Yes	Cusp & Suction
02	Free	New	Yes	Yes	Cusp, Suction & Tailboom
52	58%	New	Yes	Yes	Cusp, Suction & Tailboom
12	10%	New	Yes	Yes	Cusp, Suction & Tailboom
60	58%	Original	No	No	Suction
61	58%	New	No	No	Suction

The test program, wind-tunnel description, data reduction procedures and all related information are reported by Howe and Neumann (14) and will not be repeated here.

III - ANALYSIS OF FAN AIR POWER COEFFICIENTS

The most important result of this test analysis is the determination of the air power coefficient of the fan at the point of steady flight (zero axial force). The fan flow Q is measured in a very reliable manner at the jet discharge nozzle (station 5) by three total-pressure rakes, with one wall static tap and two static probes; two other wall static taps were available but not used. The mean inlet total-pressure is also measured by three rakes just before the fan inlet plenum (Station 2), after taking all the inlet losses from the sharp Ringloeb cusp and from the short 90° turn of the inlet duct (one rake is shown in the photo of Fig. 11); the mean outlet total pressure is measured by the three rakes at the jet discharge (Station 5). (The rakes are shown in the photos of Figs. 8, 10, 13 and 14.) The fan air power is the product of the flow and of the total-pressure differential; the fan efficiency is not included at this point, i.e. the fan is assumed to be 100% efficient. Actually the propulsor efficiency would vary with the vehicle application: for a large LTA the fan efficiency would be as high as 93%, while for a small underwater vehicle the pump efficiency could be as low as 83%.

The axial force coefficient was determined by two methods simultaneously, i.e. the wake integrated momentum as measured by a fixed rake and the calibrated strut force as measured by the wind-tunnel balance. Since the test instrumentation is adequately presented by Howe and Neumann (14), only a general discussion is given here.

Unfortunately, neither method yielded credible results in both the drag and the thrust areas for all test configurations at all speeds. Generally, the wake momentum methods yield the most reliable results if the wake-rake is carefully centered with the actual wake and the axisymmetric flowfield is well covered by a rotatable rake, swinging back

and forth over the 360° azimuth range. In this test, however, the rake was fixed (i.e. non-rotatable) and it was centered geometrically along the model's centerline; it was not checked for wake centering. Furthermore, when the empennage was mounted on the model, the rake arms were aligned directly behind the tail fins; thus, in the absence of an azimuth sweep by the rake, the low pressure reading sensed directly behind the fins was taken as an azimuth average by the data reduction procedure. The overall result is that the wake data are always equal to, or less than, the correct values. The wake data can never be higher than the correct values; if thrust is indicated, the correct value must be a thrust of equal or higher magnitude, and correspondingly if drag is indicated, the correct value must be a drag of equal or higher magnitude. It has been observed in Figs. 19-28 that in the drag area the wake data are all quite low by a factor of two or three because the wake has been shifted down substantially by the strut B.L.C. interference effect: wake centering would be imperative here.

On the other hand, it has been observed in Figs. 19-28 that the wake data appear quite acceptable in the thrust area for all test configurations at all speeds.

For the determination of the equilibrium point (zero axial force), the wake data in the thrust area have been used in this analysis to establish a mean experimental line, which would then intersect the zero force axis.

In regard to the strut force data, the strut wind-tunnel calibration does not account at all for the strut/B.L.C. interference effects. When suction is absent, the strut force yields the only reliable drag data, since the flow is separated on the aftbody over the complete azimuth range. When suction is started, the aftbody flow may not be fully attached over the complete azimuth range until very high fan powers are applied; this is reflected by the strut force data points being all shifted in a roughly parallel manner to higher fan power coefficients.

The point of complete aftbody attachment is indicated by a drastic change of the strut force data mean line slope. This "intersection" point is indicated in Figs. 19-28; it occurs in either the drag or the thrust areas and it may differ with wind-tunnel speed.

There is excellent agreement between wake data and strut force data after the intersection points for Configurations 00, 50, 51, 10, 11 and 12; the agreement is fair for Configuration 01 and poor for Configurations 02, 52, 60 and 61.

The strut/B.L.C. interaction effect is a complex closed-loop phenomenon, yielding intermittent time-dependent shifts from separated to attached aftbody flow and vice versa. The wind-tunnel balance apparently reacts to this with a bistable behavior near the neutral point (zero force) as it was noticed repeatedly by test observers.

The only way to break this closed-loop would be to apply suction on the strut at the hull intersection line, since the B.L.C. mechanism is particularly sensitive to the strong U-shape vortex originating at the strut/hull intersection. The feedback loop is provided by the hull pressure step at the slot location, which can only be achieved with adequate B.L.C. action.

Figures 19 through 28 present the fan air power coefficient plotted against the axial force coefficient (drag or thrust). The open points represent wake momentum data while the solid points represent strut force measurements. It appears quite clearly that the wake momentum method is the one to yield reliable data for the determination of the steady-state point.

The wake data points have some scatter in the thrust area and a great amount of scatter in the drag area; a mean line can be drawn in the thrust area to represent the experimental trend quite reliably. The intersection of this mean line with the zero force axis yields the steady-state air power coefficient value; the concomitant Reynolds number will be taken as the average of the test range. In order to show the volume Reynolds number effects within the limited range of this test

program ($1.20 \times 10^6 < R_v < 2.0 \times 10^6$), it is possible to consider a pair of test points at the same Reynolds number: the test point with the lowest thrust coefficient and the point with the lowest drag coefficient, straddling the zero force axis. The intersection of the line joining the two points with the zero force axis yields the steady-state air power coefficient at that Reynolds number.

Figures 19, 22 and 25 present the free transition cases (Configurations 00, 01 and 02); certain similarities can be seen among the three plots. For the two lower Reynolds numbers in the drag area, the strut force points are well organized in linear fashion from the fully separated (zero B.L.C.) drag to the steady-state air power point, while in the thrust area the strut force points are again well organized along a line substantially parallel to the mean line through the wake points. In Fig. 19 the power difference is constant, $\Delta CHP \approx 0.003$; in Fig. 22 the power difference again is constant, $\Delta CHP \approx 0.005$, while in Fig. 25 the difference is not constant, with $\Delta CHP \approx 0.008$ near the zero force axis.

In the drag area, it can be seen that all the wake points seem to have obviously low axial force coefficient values; this must be due to the wake-rake being fixed at the geometric center plane while the wake actually was shifting downward because of the strut/hull interaction. At the highest Reynolds number, in the drag area, it can be seen that the strut/hull interference mechanism causes the strut force points to be substantially higher, with $\Delta CHP \approx 0.007$; only with adequate B.L.C. suction, in the high thrust area, is this mechanism brought under control.

Figures 20, 23 and 26 represent the cases where transition was tripped at 58% length (Configurations 50, 51 and 52). The first item to be noticed is that the interference mechanism is stronger because the boundary-layer is thicker and that all strut force points in the drag area are higher; the worst case is Configuration 50 in Fig. 20, while the best case is Configuration 51 in Fig. 23. In the thrust area the

situation is very similar to that for the free-transition cases; $\Delta CHP \approx 0.0035$ for Configuration 50, $\Delta CHP \approx 0.004$ for Configuration 51, and $\Delta CHP \approx 0.009$ for Configuration 52 between the wake thrust line and the strut force thrust line.

In Fig. 28 there are presented the results of further tests with transition tripped at 58% length: here the Ringloeb cusp was eliminated by a clay fillet, so as to illustrate this cusp effect. Configuration 50 was renamed Configuration 60 and Configuration 51 was renamed Configuration 61. For both configurations, elimination of the cusp has caused all the strut force points, both in the drag and in the thrust areas, to lie along a single line from zero B.L.C. to full fan power. This is very different from the evidence of Figs. 20, 23 and 26 and it plainly demonstrates the effectiveness of the Ringloeb cusp in achieving stable boundary-layer control.

In regard to the steady-state air power, Configuration 61 has the same value as Configuration 51, while Configuration 60 shows a reduction as compared to Configuration 50 (0.0106 as against 0.0146).

Figures 21, 24 and 27 represent the cases where transition was tripped at 10% length (Configurations 10, 11 and 12) to simulate the worst possible operational conditions. It can be seen that in the drag area the strut force points are extremely high and that any agreement between strut force points and wake points is achieved only at or near full fan power at maximum thrust. The absurdity of the strut force data can be illustrated as follows: considering that the conventional naval airship, tripped at 10% length, has a drag coefficient of 0.0284 at the same Reynolds number, as reported by Cerreta (3), in Fig. 21 it can be seen that a fan air power coefficient of 0.020 is needed to achieve the same drag coefficient of 0.0284 which the airship achieves without any power at all. At the same time, the steady-state wake power coefficient is 0.0208. Figures 24 and 27 show that at air power coefficients over 0.040, in the maximum thrust area, the strut force measurements indicate consistently higher thrust than the wake measurements

for the same air power value; this is not the case for Fig. 21. There is considerably more scatter of the wake points in the thrust area for all three figures; this tends to indicate that the aftbody flow was not fully attached for the 10% trip cases. Further discussion of this important point is given below, on the basis of the correlation of the slot pressure-step with the slot suction coefficient as shown in Figs. 42, 43 and 44.

A summary of the steady-state fan air power coefficients, as determined from Figs. 19-28, is given below in Table II and is presented in the plots of Figs. 29, 30, 31 and 32.

TABLE II - FAN AIR POWER COEFFICIENTS AT ZERO AXIAL FORCE

Configuration	Figure	Volume Reynolds Number - R_V	Fan Air Power Coefficient	Symbol
00	19	1.29×10^6	0.0144	○
00	19	1.49	0.0134	○
00	19	1.94	0.0130	○
00	19	Mean Line-1.615	0.0135	●
50	20	1.25×10^6	0.0148	△
50	20	1.43	0.0136	△
50	20	1.60	0.0144	△
50	20	Mean Line-1.425	0.0146	▲
10	21	1.28×10^6	0.0209	▽
10	21	1.53	0.0228	▽
10	21	1.62	0.0232	▽
10	21	1.66	0.0196	▽
10	21	Mean Line-1.470	0.0208	▼
01	22	1.26×10^6	0.0150	◇
01	22	1.63	0.0138	◇
01	22	1.94	0.0120	◇
01	22	Mean Line-1.600	0.0124	◆

TABLE II - Cont'd.

Configuration	Figure	Volume Reynolds Number - R_V	Fan Air Power Coefficient	Symbol
51	23	1.26×10^6	0.0156	□
51	23	1.45	0.0152	□
51	23	1.62	0.0138	□
51	23	Mean Line-1.44	0.0160	■
11	24	1.26×10^6	0.0170	▽
11	24	1.45	0.0157	▽
11	24	1.63	0.0151	▽
11	24	1.91	0.0160	▽
11	24	Mean Line-1.585	0.0170	▼
02	25	1.28×10^6	0.0170	▽
02	25	1.69	0.0160	▽
02	25	1.97	0.0132	▽
02	25	Mean Line-1.625	0.0144	▶
52	26	1.27×10^6	0.0186	□
52	26	1.45	0.0160	□
52	26	1.63	0.0144	□
52	26	Mean Line-1.450	0.0174	■
12	27	1.28×10^6	0.0190	○
12	27	1.46	0.0188	○
12	27	1.63	0.0170	○
12	27	Mean Line-1.455	0.0170	●
60	28	1.47×10^6	0.0106	△
60	28	Mean Line-1.47	0.0106	◆
61	28	1.28×10^6	0.0092	◊
61	28	1.48	0.0164	▽
61	28	1.66	0.0122	▽
61	28	Mean Line-1.470	0.0159	▼

Figure 29 presents a summary of all the free-transition cases (Configurations 00, 01 and 02); first of all, it can be seen that Configuration 00 agrees with Configuration 01 at the lower Reynolds numbers but that it merges with Configuration 02 at the higher Reynolds numbers, then it can be noted that the plots for Configuration 01 and for Configuration 02 are essentially parallel, with a constant difference of $\Delta C_{HP} \approx 0.0020$ which represents the empennage contribution to power.

For the complete vehicle with empennage (Configuration 02) the free-transition air power coefficient is 0.0130, extrapolated to the volume Reynolds number benchmark of 2×10^6 ; the corresponding power coefficient for the body without empennage (Configuration 01) is 0.0115.

Figure 30 presents a summary of all the cases with transition tripped at 58% length (Configurations 50, 51 and 52). Here again Configuration 50 starts below Configuration 51 at low Reynolds numbers but reaches Configuration 52 at the higher Reynolds numbers. The plots of Configuration 51 and of Configuration 52 converge to a parallel trend, with a difference of $\Delta C_{HP} \approx 0.0010$, which represents the empennage contribution to the total power coefficient of the vehicle.

Figure 31 presents a summary of all the cases with transition tripped at 10% length (Configurations 10, 11 and 12). Here it can be seen that Configuration 10 has a very high power coefficient, well over that of Configuration 11 and of Configuration 12 over the entire test range. The plots of Configuration 11 and of Configuration 12 are essentially parallel, with a difference of $\Delta C_{HP} \approx 0.0015$ which represents the empennage contribution to the total power coefficient of the vehicle.

Figure 32 presents the summary for the complete vehicle configuration with empennage for all three transitions (Configurations 02, 52 and 12). At the benchmark volume Reynolds number of 2×10^6 , the fan air power coefficient will range from 0.0130 to 0.0155, depending on the operational mission environment.

Finally, it is of great interest to consider the capability of generating excess thrust beyond that required for steady-state flight, for purposes such as towing, fast acceleration, etc.

It is seen that considerable excess thrust was generated in the many tests, as shown in Figs. 19 through 28; thrust coefficients over 0.020 were achieved at full fan power. In Table III below there are listed the increment of fan air power coefficient required to achieve a constant thrust coefficient increment of 0.010 and the ratio of thrust over power, denoting propulsive efficiency.

TABLE III – THRUST EFFICIENCY SUMMARY

Configuration	Power Coefficient Increment	Thrust Coefficient Increment	Propulsive Efficiency
00	0.0132	0.010	0.757
50	0.0134	0.010	0.746
10	0.0138	0.010	0.724
01	0.0153	0.010	0.653
51	0.0140	0.010	0.714
11	0.0198	0.010	0.505
02	0.0131	0.010	0.763
52	0.0138	0.010	0.724
12	0.0264	0.010	0.378
60	0.0147	0.010	0.680
61	0.0140	0.010	0.714

With the exception of Configuration 11 and of Configuration 12, the average propulsive efficiency of all the other configurations is 72%; this compares quite well with the 60% propulsive efficiency of a typical propeller pod, which could be used to generate excess thrust. The reason for the different thrust performance of Configuration 11 and Configuration 12 has not yet been explored.

In conclusion, some exact comparisons remain to be made between the experimental fan air power coefficients achieved in this program and the power coefficients of conventional streamlined bodies in a wind-tunnel at the same volume Reynolds number and with comparable transition (free or tripped). Abbott (21) presents the wind-tunnel drag results for two streamlined bodies with and without empennage fins. Model A was a simplified version of the U.S. Airship "Akron" with a fineness ratio of 5.9; the aluminum surface was very smooth, i.e. it was a case of free transition. The ratio $V^{0.33}/L = 9.34/37.39 = 0.250$.

The comparison will be made against Configuration 02 at $R_v = 1.956 \times 10^6$, where Configuration 02 has $CHP = 0.0132$; at $R_L = 1.965/0.250 \times 10^6 = 7.86 \times 10^6$, the drag coefficient of Model A with empennage, free-transition, is $C_D = 0.0240$ plus $\Delta C_D = 0.003$ for the empennage, yielding a total $C_D = 0.0270$.

The equivalent drag ratio is: $0.0132/0.0270 = 0.488$. Another model was also tested by Abbott, with aluminum surface polished all over; this was model M with a fineness ratio of 4.5. The $V^{0.33}/L$ ratio was $13.06/45.44 = 0.287$; transition was free, since the surface was polished. The same comparison will be made: at $R_L = 1.965/0.287 = 6.84 \times 10^6$, the drag coefficient of Model M is $C_D = 0.0245$ plus $\Delta C_D = 0.003$ for the empennage, yielding a total $C_D = 0.0275$.

The equivalent drag ratio is: $0.0132/0.0275 = 0.480$. The wind-tunnel test of a tripped airship model is reported by Cerreta (3): Model XZS2G-1 with a fineness ratio of 4.189 and with transition tripped at 10% length. The $V^{0.33}/L$ ratio was 0.3075. At $R_L = 4.65 \times 10^6$, corresponding to $R_v = 1.43 \times 10^6$, the drag coefficient was $C_D = 0.0284$; adding $\Delta C_D = 0.003$ for the empennage, the total drag coefficient is $C_D = 0.0314$.

The comparison is made against Configuration 12 as shown in Fig. 31 at $R_v = 1.43 \times 10^6$: $CHP = 0.0180$.

The equivalent drag ratio is thusly: $0.0180/0.0314 = 0.573$.

It can be concluded, without fear of reprobation, that the present test model yields approximately 50% less equivalent drag than conventional streamlined bodies with empennage, in both the free-transition and the tripped-transition cases, at the same volume Reynolds number.

IV - YAWING MOMENTS ANALYSIS

The empennage design was previously reported by Goldschmied (22). In the test program, the yawing moments of Configuration 11 and of Configuration 12 were measured at $\alpha = 0^\circ, 3^\circ, 6^\circ$ and 8° . The test data were plotted against the slot suction, as shown in Figs. 33, 34 and 35 where the yawing moment coefficient C_Y is plotted against the suction flow coefficient C_Q . The coefficient C_Y and C_Q are defined as follows:

$$C_Y = M_Y/qV$$

$$C_Q = Q/U_0 V^{0.66}$$

where M_Y = Experimental Yawing Moment
 q = Free-stream Dynamic Pressure
 U_0 = Free-stream Velocity
 Q = Suction Flow
 V = Hull Volume

Also shown in each figure for reference is the theoretical value of the yawing moment coefficient. It can be seen that the yawing moment of Configuration 11 is practically independent of the slot suction flow coefficient at all angles ($0^\circ, 3^\circ, 6^\circ$ and 8°) while the yawing moment of Configuration 12 is very sensitive to slot suction. In each figure there appears to be a minimum suction coefficient C_Q value for full empennage effectiveness of Configuration 12; $C_Q = 0.0155$ is an acceptable minimum value for all angles of yaw.

Figure 36 presents the correlation of the yawing moment coefficient C_Y against angle of yaw α for Configuration 11 and for Configuration 12; the theoretical line is also shown for convenient reference. All the points were taken at $C_Q = 0.0155$. It can be seen

that the Configuration 11 points are in good agreement with theory and that the Configuration 12 empennage provides neutral static stability over the entire test range up to $\alpha = 8^\circ$. Thus the empennage design has been verified exactly. The fan air power contribution of the empennage/tailboom assembly can be gauged in Fig. 29 as the difference between Configuration 02 and Configuration 01, in Fig. 30 as the difference between Configuration 52 and Configuration 51, and finally in Fig. 31 as the difference between Configuration 12 and Configuration 11. At a fixed volume Reynolds number of 1.9×10^6 , the difference between the faired plots is as follows:

Free-transition (Fig. 29) $\Delta CHP = 0.0017$

Transition at 50% (Fig. 30) $\Delta CHP = 0.0007$

Transition at 10% (Fig. 31) $\Delta CHP = 0.0015$

If the actual test points are used, instead of the faired plots, the results are only slightly different, as shown below in Table IV.

TABLE IV - AIR POWER CONTRIBUTION OF EMPENNAGE AT $\alpha = 0^\circ$

Configuration	Volume Reynolds Number - R_v	Fan Air Power Differential	Average
12-11	1.26×10^6	0.0020	
12-11	1.46	0.0031	0.00175
12-11	1.63	0.0019	
12-11	Mean Line	0.0000	
52-51	1.27×10^6	0.0030	
52-51	1.45	0.0008	0.0021
52-51	1.63	0.0032	
52-51	Mean Line	0.0014	
02-01	1.28×10^6	0.0020	
02-01	1.69	0.0022	0.00185
02-01	1.97	0.0012	
02-01	Mean Line	0.0020	

It can be seen that the overall average for the fan air power contribution of the Configuration 12 empennage/tailboom assembly is $\Delta C_{HP} = 0.0019$, while the average from the faired plots was 0.0013. This can be compared with the conventional empennage drag of $\Delta C_D = 0.003$, yielding a power increment of 0.00353 if the propulsive efficiency is 85%.

The power ratio is $0.0019/0.0035 = 0.538$.

In conclusion, the Goldschmied empennage offers a saving of 46% power as against the conventional streamlined submarine. Also it can be noted that many conventional vehicles are not designed for neutral static stability but only for dynamic stability which requires smaller empennage planform.

The ratio of total empennage planform area over volume equivalent was as follows:

$$\frac{AF}{V^{0.66}} = 0.404$$

and the tailboom length ratio over maximum hull diameter was as follows:

$$\frac{\bar{D}}{D} = 0.50.$$

V - CORRELATION OF FAN COEFFICIENTS AND SELECTION OF FAN DESIGN PARAMETERS

The fan (or pump) provides both the suction for the slot boundary-layer control and the pressure for the stern jet propulsion, i.e. it is an essential part of the integrated hull, boundary-layer control and propulsion system. A poor fan installation can negate much of the power gain achievable by the integrated system.

The operational vehicle design requires also the design of the fan unit; it cannot be considered complete without it.

First the power coefficient CHP_{25} , the flow coefficient CQ_5 and the pressure coefficient CH_{25} will be correlated, as shown in Figs. 37 and 38. Figure 37 plots the slot suction flow coefficient CQ_5 against the fan air power coefficient CHP_{25} , which is obtained from Figs. 29 through 32 for the several configurations. Figure 38 plots the fan pressure-rise coefficient CH_{25} against the suction flow coefficient CQ_5 , which is obtained from the above Fig. 37. Thus the fan air power, flow and pressure are fully determined for the several configurations in the test range of volume Reynolds numbers.

The next problem is the development of a procedure for the design of the best possible fan for the job. From the flow coefficient CQ , the flow may be expressed thusly: $Q_5 = CQ_5 \times U_0 \times V^{0.66}$.

From the pressure coefficient CH_{25} , the pressure-rise may be expressed thusly: $P_{25} = CH_{25} \times \frac{1}{2} \rho U_0^2$.

The diameter of the axial fan is assumed to be equal to the stern jet diameter; for the test model the ratio of jet diameter is: $D_5/V^{0.33} = 3.25/22.15 = 0.146$.

Thus the fan diameter D_0 is expressed thusly: $D_0 = 0.146 V^{0.33}$.

The fan design parameters are taken to be the flow parameter ϕ and the pressure parameter ψ , defined as follows:

$$\phi = \frac{Q}{\frac{\pi D_0^2 u}{4}} = \frac{4Q}{\pi^2 D_0^3 n} = 0.405 \frac{Q}{D_0^3 n}$$

$$\psi = \frac{P}{\frac{1}{2} \rho u^2} = \frac{2P}{\pi^2 \rho D_0^2 n^2} = 0.203 \frac{P}{\rho D_0^2 n^2}$$

where $Q = Q_5$ = Fan Flow
 $P = P_{25}$ = Fan Pressure Rise
 U_0 = Free-stream Velocity
 V = Hull Volume
 D_5 = Ster. Jet Diameter
 D_0 = Fan Diameter
 u = Fan Tip Speed
 n = Fan Speed, RPS
 ρ = Fluid Mass Density

Substituting:

$$\phi = \frac{CQ_5 \times U_0 \times V^{0.66}}{V \times n} \times \frac{0.405}{0.146^3} = CQ_5 \left(\frac{U_0}{nV^{0.33}} \right) 130.13$$

$$\psi = \frac{CH_{25} \times \rho U_0^2}{\frac{1}{2} \rho n V^{0.66}} \times \frac{0.203}{0.146^2} = CH_{25} \left(\frac{U_0}{nV^{0.33}} \right)^2 4.76$$

The parameter $\sigma = \frac{U_0}{nV^{0.66}}$ may be termed the fan speed parameter, since the fan speed n is the only variable for a given free-stream velocity U_0 and vehicle volume V . The fan selection procedure is described as follows:

- a) Plot ϕ and ψ against the fan speed parameter σ , with the values of CQ_5 , CH_{25} , U_0 and V for the specific vehicle configuration, Reynolds

number, free-stream velocity and vehicle volume. This is shown in Fig. 39 for a specific case.

- b) Select a known tested fan design to be checked out for this vehicle application. Plot the experimental ψ and efficiency against the flow parameter ϕ , as shown in Fig. 40 for a specific case.
- c) Transfer the experimental ϕ - ψ points from b) onto the chart of a); join the experimental ψ points with a faired curve and find its intersection with the vehicle ψ plot. Read off the corresponding value of the speed parameter σ to compute the operating fan speed n . Read off the corresponding ϕ value to locate the efficiency value in the chart of b).

This fan design procedure will be illustrated by a specific example; the fan design will be that which is best suited to the test model in its operational configuration (Configuration 12) at full wind-tunnel velocity ($q = 60$ PSF).

Fan Design Specifications

Configuration 12 (Transition at 10%)

Volume Reynolds number	$R_v = 2.4 \times 10^6$
Wind-tunnel Dynamic Pressure	$q = 60$ PSF
Wind-tunnel Velocity	$U_0 = 230$ FPS
Model Volume Equivalent Length	$y^{0.33} = 1.846$ ft
Pressure Coefficient	$CH_{25} = 1.200$
Suction Flow Coefficient	$CQ_5 = 0.0128$
Fan Speed Parameter	$\sigma = 124.5/n$

The fan design parameter ϕ will be computed as follows:

$$\phi = 0.0128 \times \sigma \times 130.13 = 1.665\sigma = \frac{207.29}{n}$$

The fan design parameter ψ will be computed as follows:

$$\psi = 1.200 \times \sigma^2 \times 4.76 = 4.712\sigma^2 = \left(\frac{297.55}{n} \right)^2 .$$

The values of σ , ϕ , ψ and n are tabulated below in Table V; Figure 39 presents the plot of ϕ and ψ against σ for this specific application.

An axial compressor stage developed in 1953-54 at the NACA Lewis Flight Propulsion Laboratory was selected to be checked out for this application.

TABLE V - FAN DESIGN PARAMETERS

σ	ϕ	ψ	n(RPS)	RPM
0.150	0.249	0.128	831	49,879
0.175	0.291	0.174	711	42,680
0.200	0.333	0.228	621	37,297
0.225	0.374	0.289	553	33,208
0.250	0.416	0.357	497	29,855
0.275	0.457	0.432	452	27,177
0.300	0.500	0.514	414	24,840
0.325	0.541	0.603	382	22,957
0.350	0.582	0.700	355	21,340
0.375	0.624	0.803	331	19,903
0.400	0.666	0.913	310	18,648

The axial stage is fully described in Refs. 17 and 18; the rotor diameter was 14.00" and it was running at 9824 RPM with a tip speed $u = 600$ FPS. The inlet hub/tip ratio was 0.40 and the outlet hub/tip ratio was 0.52. Twenty rotor blades were used, with constant 2.00" chord; the thickness ratio was 0.05 at the tip and 0.08 at the hub.

The stator vanes had constant 2.00" chord with constant 0.06 thickness ratio. The experimental performance of the rotor/stator stage is given in the following Table VI and is presented in Fig. 40; the photo of the rotor is shown in Fig. 41.

TABLE VI - EXPERIMENTAL FAN PERFORMANCE

$W\sqrt{\zeta}/\mu A$	P_3/P_1	η	P_3-P_1 , in WG	ϕ	ψ	Symbol
19.25	1.125	91.0%	50.87	0.419	0.575	◎
21.25	1.120	92.0	48.84	0.463	0.552	□
23.90	1.110	94.0	44.77	0.520	0.506	◇
25.75	1.095	89.5	38.66	0.561	0.437	▽
27.80	1.075	74.5	30.52	0.605	0.345	○

where W = Weight Air Flow, 16/sec

ζ = Ratio of inlet total temperature to standard NACA atm

μ = Ratio of inlet pressure to standard NACA atm

A = Fan frontal area, ft^2

P_1 = Pressure upstream of rotor

P_3 = Pressure downstream of stator

η = Adiabatic efficiency of fan stage

It is to be noted that P_1 would be seen at Station 2 of the test model and P_3 would be seen at Station 5; thus P_3-P_1 corresponds to CH_{25} .

The experimental points of Table VI are transferred from Fig. 40 onto Fig. 39, thusly:

- In Fig. 39 locate the experimental ψ points on the ψ -curve; the points are marked by open symbols.
- In Fig. 39, for each experimental ϕ -point, locate the corresponding ψ -point along the vertical constant- σ line; these points are marked by solid symbols.
- In Fig. 39 join all the experimental ψ -points (solid symbols) with a faired curve.
- In Fig. 39 locate the intersection of the c) curve with the ψ curve; this would be the operating point of the selected fan design for the specific vehicle application at $\psi_o = 0.5225$ and at $\sigma_o = 0.303$.

- e) In Fig. 39 locate the corresponding ϕ -point at the intersection of the ϕ curve with the vertical line at $\sigma_0 = 0.303$: $\phi_0 = 0.505$.
- f) In Fig. 40 spot this operating point at $\phi_0 = 0.505$ and read off the corresponding adiabatic efficiency $\eta = 93.5\%$.

In conclusion, the operating fan parameters would be as follows:

$$D_0 = 3.250"$$

$$\phi_0 = 0.505$$

$$\psi_0 = 0.5225$$

$$\eta = 93.5\%$$

$$\sigma_0 = 0.303$$

$$\text{RPM} = 24,653$$

It must be noted that reduction of the rotor diameter from the tested 14.00" to 3.25" (for this wind-tunnel model) will have an effect on the performance, particularly the adiabatic efficiency. It would be much more advisable to increase the model size by a factor of 4.30 and to use the NASA Langley 30 ft \times 60 ft wind-tunnel, if the overall power coefficient is to be guaranteed.

VI - ANALYSIS OF BOUNDARY-LAYER CONTROL PARAMETERS

The inviscid pressure distribution of the test model has a step pressure-rise $\Delta CP \approx 1.00$ at 86% length, i.e. all the aftbody pressure recovery is taken at once. In the absence of effective boundary layer control at this step, however, the real viscous flow will separate and little, if any, pressure recovery will be achieved, i.e. $\Delta CP \approx 0$. Thus the experimental pressure step ΔCP across the suction slot is a meaningful measure of the boundary-layer control effectiveness achieved by the slot suction flow CQ_5 . The static pressure on the hull is measured by a series of flush pressure taps; the measurement of the slot pressure differential ΔCP is provided by the two taps nearest to the slot, one upstream and the other downstream.

Figure 42 presents the plot of the experimental pressure step ΔCP against the slot suction flow coefficient CQ_5 for Configuration 00 and Configuration 01; a similar plot is given in Fig. 43 for Configurations 01 and 11 and another plot in Fig. 44 for Configurations 02 and 12.

Three CQ segments can be observed in all three figures:

- a) The first segment, starting from zero flow, shows small or zero pressure step values; this is the area of complete aftbody flow separation.
- b) The second segment shows a very steep rise of the pressure step; the slope change is dramatic at the boundary between the first and second segment. This is the area of incipient aftbody flow attachment, where the flow is not yet steady.
- c) The third segment shows a pressure step rise with much lower slope; the slope change is very apparent at the boundary between second and third segments. This is the area of full aftbody flow attachment.

The inviscid flow pressure step of $\Delta CP = 1.00$ is indicated in all three figures; the maximum ΔCP achieved experimentally varies from 0.985 for Configuration 00 to 0.805 for Configuration 10. A summary of the performance of all the configurations is given below in Table VII; it can be seen that for free transition the most efficient (least C_Q value) aftbody attachment is achieved by Configuration 01, while for transition tripped at 10% length, this is achieved by Configuration 12. Thus it is demonstrated that the tailboom, while serving as the structural support of the empennage, also serves an important aerodynamic function for the stabilization of the flow field in the rear of the body and for the consequent minimization of the required boundary-layer control suction power. The absence of the tailboom (Configurations 00 and 01) causes a suction flow increase from 20% to 30% for full aftbody attachment.

It is interesting to note that the aerodynamic role of the tailboom was suggested by repeated observations that sting-mounted models in wind-tunnels always had higher aftbody pressure recoveries than comparable strut-mounted models.

TABLE VII - SUMMARY OF SLOT PRESSURE STEPS

Configuration	End of Complete Aftbody Separation		Start of Full Aftbody Attachment		Maximum Slot Pressure Step
	C_Q_5	ΔCP	C_Q_5	ΔCP	
00	0.0060	0.05	0.0130	0.865	0.985
10	0.0156	-0.02	0.0178	0.685	0.805
01	0.0038	0.085	0.0098	0.780	0.940
11	0.0114	-0.045	0.0171	0.693	0.855
02	0.0058	0.125	0.0103	0.790	0.950
12	0.0108	-0.090	0.0150	0.650	0.840

With free-transition, the maximum pressure step achieved ranges from 0.940 to 0.985; this compares quite well with the inviscid value of 1.00. With transition tripped at 10%, the maximum pressure step achieved

ranges from 0.805 to 0.855; to explain this difference it would be necessary to carry out the inviscid computation on the body geometry augmented by the turbulent boundary-layer displacement thickness.

It is to be noted that Figs. 42, 43 and 44 contain all the test points within the experimental Reynolds number range; it is of great interest to spot in Figs. 42, 43 and 44 the CQ points corresponding to the equilibrium fan air power (zero axial force). Using the mean line power coefficients of Table I, the following results are obtained, as presented below in Table VIII.

In Fig. 42 it can be seen that for Configuration 00 the zero-force CQ point is below the full aftbody attachment boundary by only a small amount, while for Configuration 10 the zero-force CQ point is only down at the incipient attachment boundary.

TABLE VIII — SUMMARY OF ZERO AXIAL FORCE SUCTION

FLOW COEFFICIENTS

Configuration	Mean Volume Reynolds Number R_v	Mean Line Fan Air Power Coefficient CHP_{25}	Suction Flow Coefficient CQ_5
00	1.615×10^6	0.0135	0.0120
10	1.470	0.0208	0.0144
01	1.600	0.0124	0.0117
11	1.585	0.0170	0.0133
02	1.625	0.0144	0.0124
12	1.455	0.0170	0.0133

In Fig. 43 it can be seen that for Configuration 01 the zero-force CQ point is well above the full aftbody attachment boundary, while for Configuration 11 the zero-force CQ point is less than halfway to full attachment.

In Fig. 44 it can be seen that for Configuration 02 the zero-force CQ point is well above the full aftbody attachment boundary while for Configuration 12 the zero-force CQ point is over halfway to full attachment.

Thus for Configurations 01 and 02 the boundary-layer control is well matched to the propulsion; for Configuration 11 and for Configuration 12 more suction flow should be used at the zero-force point (25% and 12% more flow, respectively), with corresponding decrease of the stern jet velocity and increase of the jet diameter so as to maintain the same thrust.

At this point it is useful to note explicitly that the boundary-layer control function comprises three elements in order to be efficient and stable:

- a) Ringloeb cusp
- b) Slot suction
- c) Tailboom

All three elements must be present in the vehicle design; suction alone cannot be depended on because it can be very unstable against the pressure step.

Finally, it is of great significance to develop the correlation between the boundary-layer Reynolds number upstream of the slot, the minimum suction flow coefficient C_{Q_5} for full attachment and the inlet pressure loss ratio.

Figure 45 shows the plot of a new suction flow coefficient $CS = Q/U_1\delta_1 V^{0.33}$ against the Reynolds number $R_\delta = U_1\delta_1/v$.

The values of Q represent in all cases the best estimates of minimum suction for full aftbody attachment. It can be seen in Fig. 45 that a workable correlation does exist, with a minimum $CS \sim 0.40$ and a maximum $CS \sim 2.40$ within the experimental R_δ range.

Furthermore, the slot inlet pressure loss must be known in order to proceed from the total pressure at Station 1 (predictable by hull boundary-layer computations) upstream of the slot to the total

pressure at Station 2 inside the slot at the fan plenum entrance. The total-pressure at Station 1 is the mass-averaged mean pressure of that portion of the boundary-layer which is taken into the suction slot, as measured by the rake of Station 1; the total-pressure at Station 2 is the mass-averaged mean pressure as measured across the entire height of the annular passage by the rake of Station 2.

Figure 46 presents the correlation of the slot inlet pressure loss ratio CH_{12}/CH_{25} with the boundary-layer Reynolds number R_δ . The pressure loss ratios correspond to the suction flows used in Fig. 45. It can be seen that a workable correlation does occur, with minimum loss ratios of 0.20 and maximum loss ratios of 0.55 within the experimental R_δ range.

VII - ANALYSIS OF PROPULSION JET

While there have been two previous wind-tunnel tests in 1957 (3) and in 1969 (5) demonstrating the hull interaction with boundary-layer control, this is the first test of the complete hull/boundary-layer control/propulsion interaction, with and without tailboom.

The static pressure at the jet discharge (as measured here by one wall static tap and by two static probes) was generally assumed to be substantially near free-stream's, i.e. to have static-pressure coefficients of the order of 0.1-0.2, as in the case of conventional streamlined bodies. This was found to be far from the experimental truth: Figures 47, 48 and 49 present the plot of the jet static-pressure coefficient C_{Q_5} against the slot pressure step ΔC_P for Configurations 00, 10, 01, 11, 02 and 12. The slot pressure step ΔC_P was chosen as the best representation of the degree of aftbody flow attachment, as seen in Figs. 42, 43 and 44. In all three figures the characteristics are similar up to the full aftbody attachment boundary: from free-stream static for the complete separation case, the jet static-pressure coefficient has an abrupt or step rise for incipient attachment to 0.3-0.5 levels; then there occurs a linear growth phase up to the full aftbody attachment boundary.

In Figs. 42, 43 and 44 it was shown that the tailboom of Configurations 02 and 12 has a substantial effect on reducing the full aftbody attachment C_{Q_5} by 20% to 30%. Here in Figs. 47, 48 and 49 it can be seen that the tailboom has a dramatic effect on the jet static-pressure after full aftbody attachment has been achieved. While in Fig. 47 Configurations 00 and 10 continue their linear trends after full aftbody attachment, in Figs. 48 and 49 Configurations 01, 11, 02 and 12 show an abrupt rise of jet static-pressure after full aftbody attachment, reaching full stagnation values.

Configuration 02 presents an unique case of a step rise of jet static-pressure to full stagnation: this can only mean that, once the aftbody flow is fully attached, the flowfield snaps on the tailboom to achieve complete and stable closure. This effect has never been observed before in any wind-tunnel experiment with axisymmetric bodies.

Clearly, jet static-pressure increases mean fan pressure rise increases and thusly fan air power coefficient increases: the suction flow must be kept low enough to avoid triggering jet static-pressure steps. On the other hand, the suction flow must be kept high enough to insure full aftbody attachment, so as to prevent high wake drag and flow instabilities. These constraints must be included in the new optimization model; they were not considered in the original aerodynamic integration.

A summary of the jet discharge static pressures is given below in Table IX. The allowable range of suction flow coefficients CQ_5 may be estimated from Figs. 43, 44, 48 and 49 as shown below in Table X. Figure 50 presents the plot of the jet velocity ratio over free-stream velocity against jet total-pressure ratio over free-stream dynamic pressure. It can be seen that a velocity ratio of 0.69 corresponds to a total-pressure ratio of 1.0 and that a velocity ratio of 1.0 corresponds to a total-pressure ratio of 1.81.

TABLE IX - SUMMARY OF JET STATIC-PRESSURE COEFFICIENTS

Configuration	Incipient Aftbody Attachment		Full Aftbody Attachment		Maximum Static Pressure	
	CP_5	ΔCP	CP_5	ΔCP	CP_5	ΔCP
00	0.430	0.0050	0.600	0.850	0.655	0.985
10	0.360	0.015	0.515	0.690	0.560	0.805
01	0.295	0.065	0.505	0.780	1.100	0.950
11	0.490	0.000	0.715	0.690	1.070	0.860
02	0.310	0.015	0.550	0.800	1.095	0.925
12	0.450	0.020	0.660	0.640	1.065	0.850

TABLE X - ALLOWABLE RANGE OF FLOW COEFFICIENTS

Configuration	Minimum Flow for Aftbody Attachment CQ_5	Maximum Flow before Jet Static- Pressure Rise CQ_5
01	0.0098	0.0130
11	0.0171	0.0182
02	0.0103	0.0150
12	0.0150	0.0166

The jet velocity ratio and the jet total-pressure ratio are tabulated below in Table XI for Configurations 00, 10, 01, 11, 02 and 12 at the equilibrium (zero axial force) point.

TABLE XI - JET VELOCITY RATIO AND TOTAL-PRESSURE RATIO

Configuration	Fan Air Power Coefficient CHP_{25}	Suction Flow Coefficient CQ_5	Velocity Ratio U_5/U_0	Total Pressure Ratio H_5/q
00	0.0135	0.0120	0.692	1.005
10	0.0208	0.0144	0.830	1.400
01	0.0124	0.0117	0.675	0.980
11	0.0170	0.0133	0.767	1.160
02	0.0144	0.0124	0.715	1.05
12	0.0170	0.0133	0.767	1.160

It can be seen that all velocity ratios are well below unity, i.e. the discharge jet velocity is well below free-stream velocity. It can also be seen that two cases (Configurations 00 and 01) have jet total-pressure ratio of essentially unity, i.e. there is no excess total-pressure in achieving steady-state flight.

Since jet propulsion has always been associated with jet velocities and jet total-pressures above free-stream's, the above achievement of having steady-state flight with jet total-pressure equal to free-stream's is worthy of careful recognition.

VIII - PRELIMINARY ANALYSIS OF ALTERNATE CONFIGURATIONS

Many applications of operational vehicles have diameter constraints, i.e. the diameter is limited by the type of installation which is dictated by the vehicle's mission. The fineness ratio of 2.70 was originally selected by Goldschmied (1)(2)(4) on the basis of the Lighthill two-dimensional airfoil; a fineness ratio of 3.0 is generally accepted as yielding minimum drag for theoretical non-separating spheroids (Ref. 10). From wind-tunnel and towing-tank testing, the best fineness ratio is known to be between 5.0 and 6.0.

A preliminary analysis will be carried out, considering application of the single-slot boundary-layer control suction concept to three turbulent bodies with fineness ratios of 9.39, 7.47 and 4.06, which are presented by Smith, Stokes and Lee (19) as bodies CD8, R8 and R4. In all three cases there is a pressure discontinuity at locations well aft (85%, 94% and 86% length, respectively) which is tailored for a Stratford zero skin-friction pressure recovery on the aftbody. Only a slight aftbody geometry change would be required to achieve the slot pressure step for the suction boundary-layer control from the Stratford pressure plot.

Table XII presents the tabulation of coordinates for the body CD8 with 9.39 fineness ratio from Ref. 19; this body has a semi-spherical nose, a constant-diameter forebody up to 85% length and then a short aftbody. The pressure distribution has a spike at the forebody-aftbody boundary.

Table XIII presents the tabulation of coordinates for the body R8 with 7.47 fineness ratio from Ref. 19; this body has a Reichardt forebody with constant pressure up to 94% length and then a short aftbody.

Table XIV presents the tabulation of coordinates for the body R4 with 4.06 fineness ratio from Ref. 19; this body also has a Reichardt

TABLE XII - HULL COORDINATES OF BODY CD8 (Case 1, Ref. 19)

I	X/R	r/R	I	X/R	r/R
1	0.0000	0.0000	27	14.1583	.9955
2	.0093	.1566	28	14.8068	.9795
3	.0426	.3100	29	15.3319	.9656
4	.0999	.4561	30	15.7250	.9462
5	.1797	.5912	31	15.9814	.9336
6	.2798	.7120	32	16.1325	.8925
7	.3977	.8156	33	16.2782	.8266
8	.5303	.8994	34	16.4333	.7784
9	.6746	.9613	35	16.5871	.7207
10	.8266	.9999	36	16.7439	.6679
11	.9829	1.0138	37	16.9007	.6127
12	1.2397	1.0167	38	17.0585	.5596
13	1.6332	1.0202	39	17.2163	.5066
14	2.1585	1.0244	40	17.3743	.4550
15	2.8072	1.0289	41	17.5322	.4045
16	3.5679	1.0335	42	17.6899	.3556
17	4.4266	1.0376	43	17.8474	.3081
18	5.3657	1.0410	44	18.0047	.2623
19	6.3696	1.0433	45	18.1618	.2182
20	7.4154	1.0440	46	18.3188	.1760
21	8.4828	1.0433	47	18.4756	.1358
22	9.5503	1.0401	48	18.6323	.0978
23	10.5961	1.0355	49	18.7890	.0624
24	11.5990	1.0280	50	18.9459	.0298
25	12.5391	1.0194	51	19.1032	.0022
26	13.3977	1.0074			

TABLE XIII - HULL COORDINATES OF BODY R8 (Case 4, Ref. 19)

I	X/R	r/R	I	X/R	r/R
1	0.0000	0.0000	27	8.4958	.9998
2	.0139	.0139	28	8.9961	.9906
3	.0601	.0601	29	9.4924	.9780
4	.1381	.1381	30	9.9827	.9608
5	.2472	.2472	31	10.4650	.9403
6	.3870	.3870	32	10.9375	.9144
7	.5569	.5569	33	11.3982	.8854
8	.7561	.7561	34	11.8451	.8496
9	.9840	.9840	35	12.2767	.8111
10	1.2396	1.2396	36	12.6906	.7631
11	1.5219	1.5219	37	13.0857	.7127
12	1.8298	1.8298	38	13.4584	.6470
13	2.1620	2.1620	39	13.8089	.5774
14	2.5173	2.5173	40	14.1273	.4744
15	2.8942	2.8942	41	14.2185	.4277
16	3.2912	3.2912	42	14.2994	.3647
17	3.7068	3.7068	43	14.3895	.3159
18	4.1394	4.1394	44	14.4789	.2658
19	3.2912	4.5872	45	14.5706	.2200
20	5.0484	5.0484	46	14.6632	.1760
21	5.5213	5.5213	47	14.7571	.1350
22	6.0039	6.0039	48	14.8521	.0966
23	6.4944	6.4944	49	14.9484	.0614
24	6.9909	6.9900	50	15.0457	.0292
25	7.4912	7.4912	51	15.1447	.0026
26	7.9935	7.9935			

TABLE XIV - HULL COORDINATES OF BODY R^o (Case 8, Ref. 19)

I	X/R	r/R	I	X/R	r/R
1	0.0000	0.0000	27	4.2397	1.0096
2	.0051	.1222	28	4.4898	1.0030
3	.0267	.2070	29	4.7379	.9929
4	.0647	.2814	30	4.9829	.9791
5	.1186	.3494	31	5.2240	.9618
6	.1880	.4125	32	5.4601	.9406
7	.2725	.4717	33	5.6901	.9157
8	.3718	.5273	34	5.9133	.8866
9	.4854	.5798	35	6.1285	.8535
10	.6129	.6292	36	6.3347	.8154
11	.7538	.6756	37	6.5311	.7728
12	.9075	.7191	38	6.7162	.7235
13	1.0734	.7598	39	6.8887	.6674
14	1.2509	.7975	40	7.0150	.6137
15	1.4392	.8324	41	7.1225	.5285
16	1.6376	.8643	42	7.2442	.4652
17	1.8453	.8932	43	7.3639	.3980
18	2.0616	.9191	44	7.4867	.3368
19	2.2854	.9420	45	7.6103	.2773
20	2.5160	.9617	46	7.7357	.2215
21	2.7524	.9783	47	7.8623	.1688
22	2.9937	.9918	48	7.9904	.1197
23	3.2389	1.0020	49	8.1200	.0744
24	3.4872	1.0089	50	8.2510	.0339
25	3.7373	1.0125	51	8.3842	.0009
26	3.9885	1.0128			

forebody with constant pressure up to 86% length and then a short aftbody.

This preliminary analysis will attempt to estimate relative (if not absolute) values of the slot suction flow coefficient C_Q for these three bodies and for the original Goldschmied design (4).

The suction flow coefficient C_Q is expressed as follows:

$$C_Q = 2\pi C_\theta \left(\frac{U_1}{U_0} \right) \left(\frac{\theta_1}{\sqrt{0.33}} \right) \left(\frac{r_1}{\sqrt{0.33}} \right) = \frac{Q}{U_0 V 0.66}$$

where $C_\theta = \frac{Q}{U_1 \theta_1 2\pi r_1}$ Boundary-layer Control Parameter

Q = Total Suction Flow

U_0 = Free-stream Velocity

U_1 = Velocity Upstream of Suction Slot

U_6 = Velocity Downstream of Suction Slot

r_1 = Body Radius at Suction Slot

R = Maximum Body Radius

θ_1 = Momentum Thickness Upstream of Suction Slot

V = Body Volume.

The parameters $\left(\frac{U_1}{U_0} \right)$, $\left(\frac{\theta_1}{\sqrt{0.33}} \right)$ and $\left(\frac{r_1}{\sqrt{0.33}} \right)$ will be estimated for the four cases; the boundary-layer control parameter C_θ will be taken as a function of the slot velocity ratio $\frac{U_6}{U_1}$ from the simple two-dimensional Taylor theory, as plotted in Fig. 51. The downstream velocity U_6 is assumed to be 0.70 in all cases; the length Reynolds number is taken to be 10^7 in all cases for this first relative evaluation.

The $\frac{U_1}{U_0}$ are given in Ref. 19 for turbulent bodies CD8 and R8 for $R_L = 10^7$, as well as $\frac{r_1}{R}$ and $\frac{U_1}{U_0}$ values. For the R4 body, only laminar results are given for $R_L = 10^7$; the $\frac{U_1}{U_0}$ value is estimated as follows for the turbulent $R_L = 10^7$ case:

- a) Compute θ_1 ratio for the R8 turbulent body and the R8 laminar body: $0.0358/0.00583 = 6.140$ at $R_L = 10^7$.
- b) Assume that the ratio holds also for the R4 laminar body:

$$\left(\frac{\theta_1}{R}\right)_{\text{turbulent}} = 6.140 \left(\frac{\theta_1}{R}\right)_{\text{laminar}} = 0.0395 \text{ at } R_L = 10^6.$$
- c) Compute θ_1 ratio for turbulent R8 body and estimated turbulent R4 body at $R_L = 10^6$: $0.0395/0.0518 = 0.762$.
- d) Correcting this ratio for $R_L = 10^7$, the estimated θ_1 for the turbulent R4 body is: $\frac{\theta_1}{R} = 0.0232$ at $R_L = 10^7$.

All the results are presented below in Table XV.

TABLE XVI – SUMMARY OF SUCTION FLOW PARAMETERS

Configuration	CD8	R8	R4	Goldschmied
$y^{0.33}/R$	3.781	3.217	2.596	2.215
r_1/R	0.892	0.474	0.528	0.576
$r_1/y^{0.33}$	0.236	0.147	0.203	0.259
CP_{\min}	-0.492	-0.06	-0.190	-0.400
U_1/U_0	1.220	1.0295	1.090	1.183
U_6/U_0	0.700	0.700	0.700	0.700
U_6/U_1	0.573	0.680	0.641	0.590
C_θ	1.55	0.75	1.00	1.40
$\theta_1/R @ R_L = 10^7$	0.0170	0.0358	0.0232	0.00912
$\theta_1/y^{0.33} @ R_L = 10^7$	0.00454	0.0111	0.0090	0.00409
Prismatic Coeff. KV	0.896	0.706	0.687	0.642
$L/D @ r/R = 0.062$	9.39	7.47	4.06	2.70
$L/D @ r_1$	8.065	7.06	3.505	2.435
L_1/L	0.858	0.945	0.863	0.900
C_Q	0.0127	0.00791	0.0124	0.0110
Flow Rating Index	1.154	0.719	1.127	1.000

Finally, the last line represents the relative suction flow rating of the four bodies, with the Goldschmied body being assigned the rating of unity. The results are unexpected: the R8 body appears to require 28% less flow than the 2.70 body while the R4 body needs 12% more flow. The CD8 torpedo-like body requires only 15% more flow.

Another useful approach would be to consider only the class of Reichardt forebodies and to plot all the parameters against fineness ratio for the R8, R4 and the Goldschmied body. The latter can be classified as a partial Reichardt design, since the pressure distribution is flat from 40% to 85% length.

Figure 52 presents the plots of the radius ratio ($r_1/V^{0.33}$) of the momentum thickness ratio ($\theta_1/V^{0.33}$) and of the velocity ratio (U_1/U_0) against (L/D) ; it can be seen that the radius and the velocity decrease with fineness ratio while the momentum thickness increase with fineness ratio. Figure 53 presents the plot of the boundary-layer control parameter C_θ and of the suction slot flow coefficient C_Q against fineness ratio. The results are that maximum C_Q values appear at $\frac{L}{D} \approx 4$ and minimum values appear at $\frac{L}{D} \approx 7.5$.

If a fineness ratio of 4.70 is required for some specific application, the parameters may be read off the plots of Figs. 52 and 53:

$$\begin{aligned} r_1 &= V^{0.33} \times 0.192 \\ \theta_1 &= V^{0.33} \times 0.00975 \\ U_1 &= U_0 \times 1.071 \\ C_\theta &= 0.92 \\ C_Q &= 0.0120 \end{aligned}$$

Suction Flow Rating = 1.091.

The correct body shape may be approximated by stretching the R4 geometry by the factor $4.7/4.06 = 1.157$.

However, before firm design conclusions are drawn for a specific Reynolds number, a detailed parametric numerical investigation

needs to be carried out over a fineness range from 2 to 10 and at each fineness ratio with several forebodies from Reichardt constant-pressure shapes to pointed shapes with constant-pressure gradients.

IX - CONCLUSIONS AND RECOMMENDATIONS

The present test program has been very productive. The most significant conclusions from the analysis are listed below:

- 1) The equivalent drag coefficient of the complete test model with empennage is ~50% lower than that of conventional streamlined bodies with fins both for the free-transition case and for the case of transition tripped at 10% length, at exactly the same volume Reynolds number.
- 2) The potential seems to exist for increasing the power gain from 50% to 70% by achieving the following:
 - (a) Decrease in half the total-pressure loss which occurs at the slot inlet between Sta. 1 and Sta. 2; a power gain of 10% would result from this improvement.
 - (b) Redesign the hull by increasing the fineness ratio from 2.70 to 7.47 and by using a constant-pressure Reichardt forebody; a preliminary analysis has indicated that a power gain over 28% can be achieved, relative to the present test model.
- 3) The test empennage has provided exactly neutral static stability with a fan air power coefficient increment of 0.0019 and with a ratio of total fin planform area over volume equivalent of 0.404.
- 4) With the fixed jet diameter used in the test program, it was found that the boundary-layer control flow was very well matched to the jet velocity for the free-transition case but not for the tripped-transition case. In the latter case, at the correct jet velocity the suction flow was below that needed for full aftbody attachment, i.e.

more suction flow was needed, with consequent lower jet velocity and larger jet diameter to maintain the same thrust.

5) For both efficient and stable boundary-layer control it was found that three elements must be combined in the body design:

- (a) Ringloeb cusp
- (b) Suction slot flow
- (c) Tailboom

6) The free-transition body without empennage has been observed to fly in steady-state with a jet velocity ratio over free-stream's of 0.675 and with a jet total-pressure ratio over free-stream dynamic pressure of approximately 1.0; this is of basic significance because it verifies the energy recovery assumptions of the integrated aerodynamic concept.

7) A procedure has been developed for the selection of the best fan design parameters from the vehicle coefficients. A new fan speed parameter has been defined, relating fan RPM to free-stream velocity and body volume. As a specific example, a fan design with 93.5% adiabatic efficiency was selected from a tested NACA axial rotor/stator stage.

It is recommended that a theoretical and wind-tunnel investigation be carried out to optimize the predicted fineness ratio effect.

REFERENCES

1. F. R. Goldschmied, "Proposal for the study of application of boundary-layer control to lighter-than-air craft," Goodyear Aircraft Report GER-5796 (1954).
2. F. R. Goldschmied, "A theoretical aerodynamic analysis of a boundary-layer controlled airship hull," Goodyear Aircraft Report GER-6251 (1954).
3. P. A. Cerreta, "Wind-tunnel investigation of the drag of a proposed boundary-layer controlled airship," David Taylor Model Basin Aero Report 914 (March 1957).
4. F. R. Goldschmied, "Integrated hull design, boundary-layer control and propulsion of submerged bodies," AIAA Journal of Hydraulics, Vol. 1, No. 1, pp. 1-11 (July 1967).
5. F. R. Goldschmied, "Aerodynamic analysis of the 1969 wind-tunnel tests of the Goldschmied body. Vol. I - Slot geometries and body pressure distributions; Vol. II - Boundary-layer suction, transition and wake drag," Westinghouse Electric Corp., R&D Center, Research Report 77-1E9-BLCON (March 1977).
6. J. S. Parsons, R. E. Goodson and F. R. Goldschmied, "Shaping of axisymmetric bodies for minimum drag in incompressible flow," AIAA Journal of Hydraulics, Vol. 8, No. 3, pp. 100-107 (July 1974).
7. F. R. Goldschmied, "Axisymmetric vehicle system design for total propulsion power optimization," Proceedings of Low-speed Boundary-layer Transition Workshop: II, Santa Monica, CA, September 1976, Rand Corp. Report P-6119 (January 1978).
8. F. R. Goldschmied, "LTA propulsion power optimization: an overview," AIAA Paper 77-1178, LTA Technology Conference, Melbourne, FL (August 1977).

9. F. R. Goldschmied, "Aerodynamic design for 'HASPA' LTA optimization," AIAA Journal of Aircraft, Vol. 15, No. 9, pp. 634-638 (September 1978).
10. J. L. Hess, "On the problem of shaping an axisymmetric body to obtain low drag at large Reynolds numbers," SNAME Journal of Ship Research, Vol. 20, No. 1, pp. 51-60 (March 1976).
11. F. R. Goldschmied, J. S. Parsons and R. E. Goodson, "Comments on Hess," SNAME Journal of Ship Research, Vol. 20, No. 4, pp. 233-234 (December 1976).
12. B. H. Carmichael, "Underwater vehicle drag reduction through choice of shape," AIAA Paper 66-657, Second Joint Propulsion Conference (June 1966).
13. R. T. Leitner, Jr., and E. F. McCabe, Jr., "Preliminary assessment of the feasibility of a low-drag spherical submersible (U)," DTNSRDC/ASED-81/20 (December 1982), CONFIDENTIAL.
14. H. J. Howe and B. J. Neumann, "An experimental validation of a low propulsion power, discrete suction concept applied to an axisymmetric vehicle," DTNSRDC/TM-16-82/02 (January 1982).
15. E. M. Dempsey, "Static stability characteristics of a systematic series of stern control surfaces on a body of revolution," DTNSRDC Report 77-0085 (August 1977).
16. H. C. McLemore, "Wind-tunnel tests of a $\frac{1}{20}$ scale airship model with stern propellers," NASA TN D-1026 (1962).
17. G. K. Serovy, W. H. Robbins and F. W. Glaser, "Experimental investigation of a 0.4 Hub/Tip diameter ratio axial-flow compressor inlet stage. I - Rotor design and overall performance at tip speeds from 60% to 100% of design," NACA RM E53I11 (December 1953).
18. J. C. Montgomery and F. W. Glaser, "Experimental investigation of a 0.4 Hub/Tip diameter ratio axial flow compressor inlet stage. II - Stage and blade element performance," NACA RM E54I29 (January 1955).

19. A.M.O. Smith, T. R. Stokes, Jr. and R. S. Lee, "Optimum tail shapes for bodies of revolution," AIAA Journal of Hydronautics, Vol. 15, Nos. 1-4, pp. 67-80 (December 1981).
20. F. R. Goldschmied, "An approach to turbulent incompressible separation under adverse pressure gradients," AIAA Journal of Aircraft, Vol. 2, pp. 108-115 (March/April 1965).
21. I. H. Abbott, "The drag of two streamlined bodies as affected by protuberances and appendages," NACA Report 451 (1932).
22. F. R. Goldschmied, "Analysis and redesign of the 1957 Goldschmied model," Contract N00167-80-M-4800, May 25, 1981.

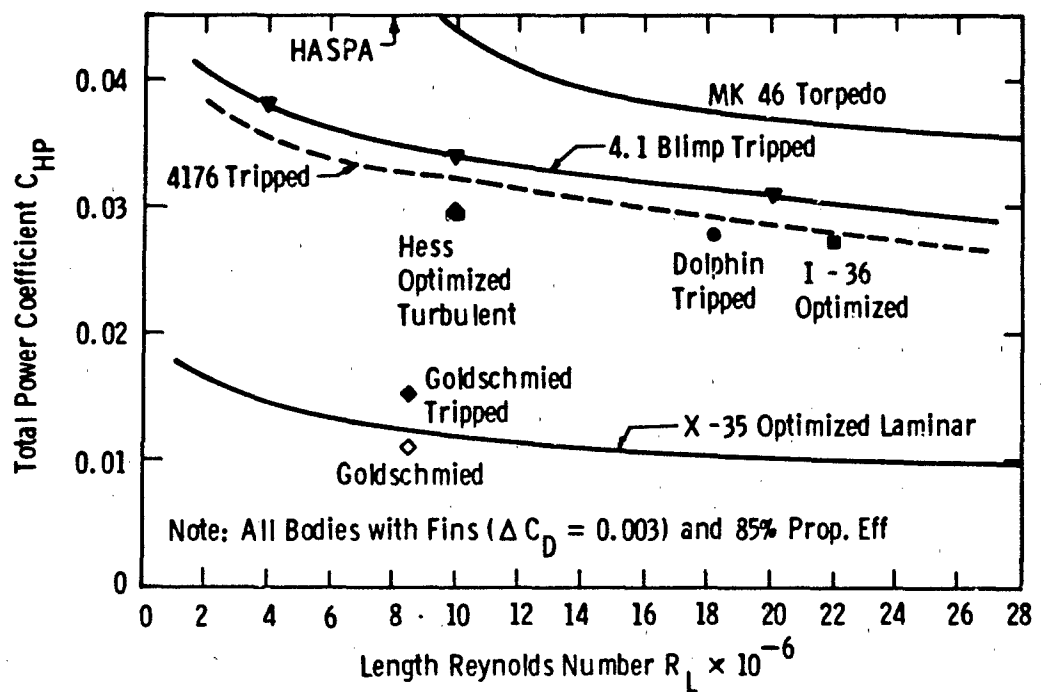


FIG.1 - SURVEY OF VEHICLE TOTAL POWER COEFFICIENTS

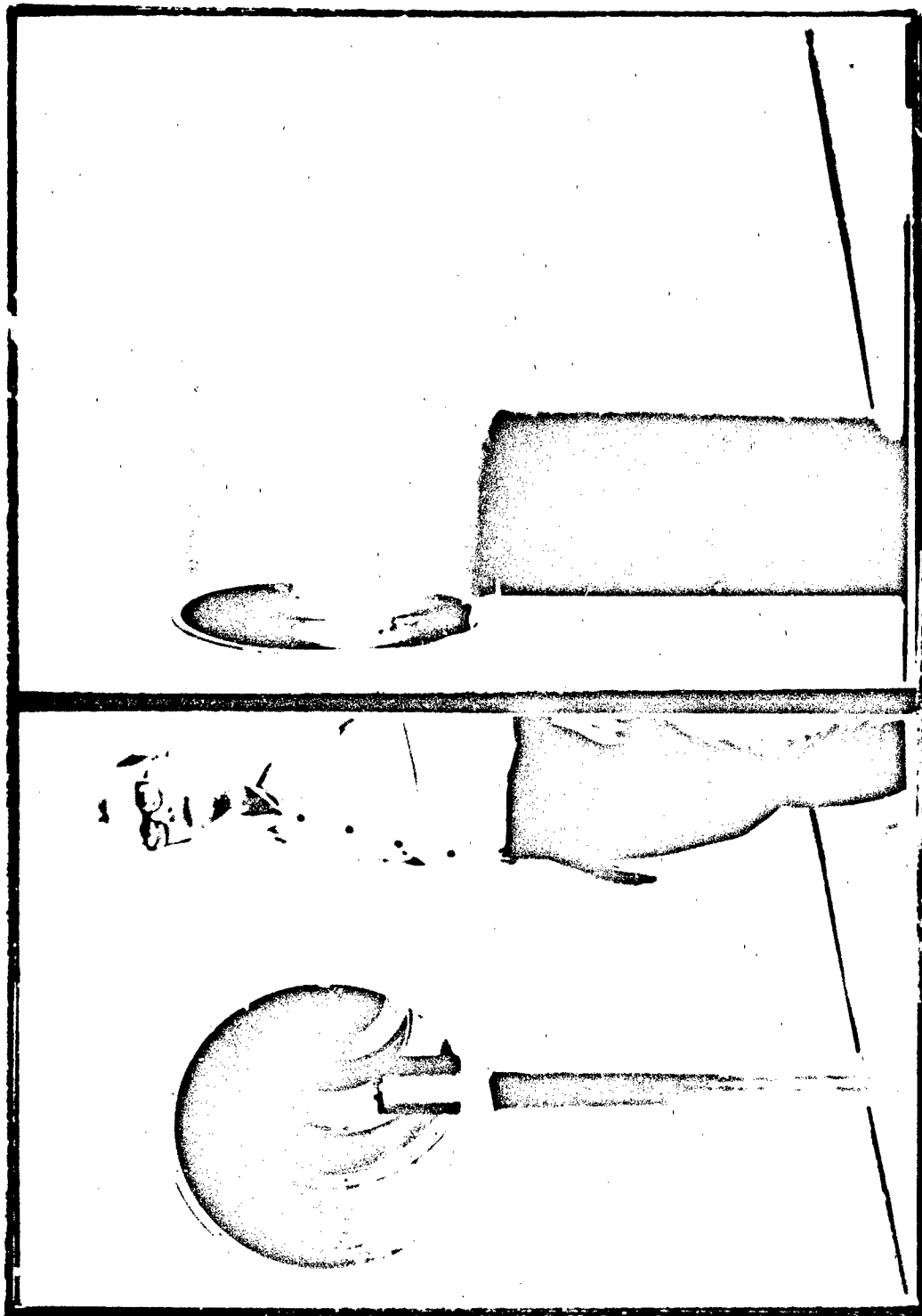


FIG. 2 - PHOTOS OF 1957 FOREBODY ON VERTICAL STRUT

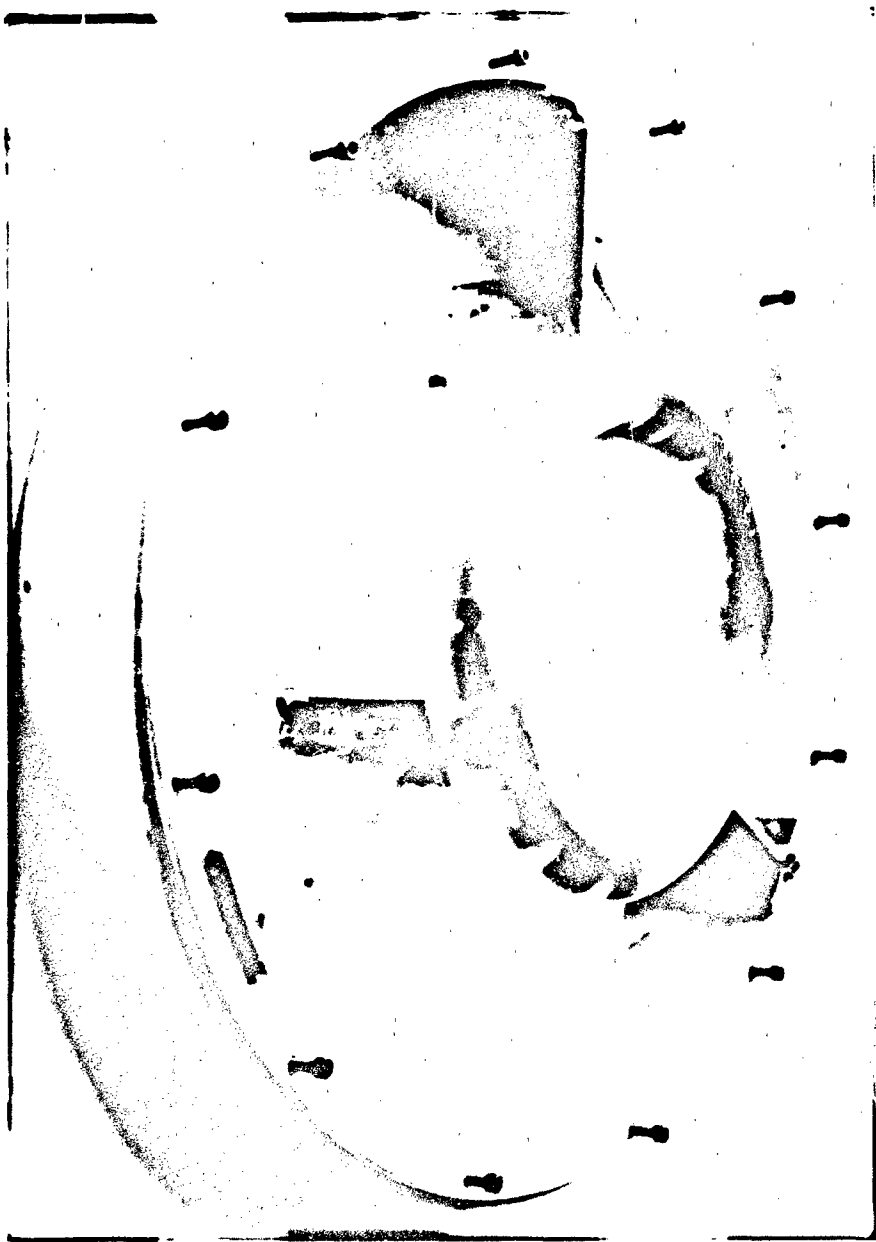


FIG.3 - PHOTO OF INTERMEDIATE HULL SECTION WITH CENTRAL RING ASSEMBLY AND FAN INLET FLARE

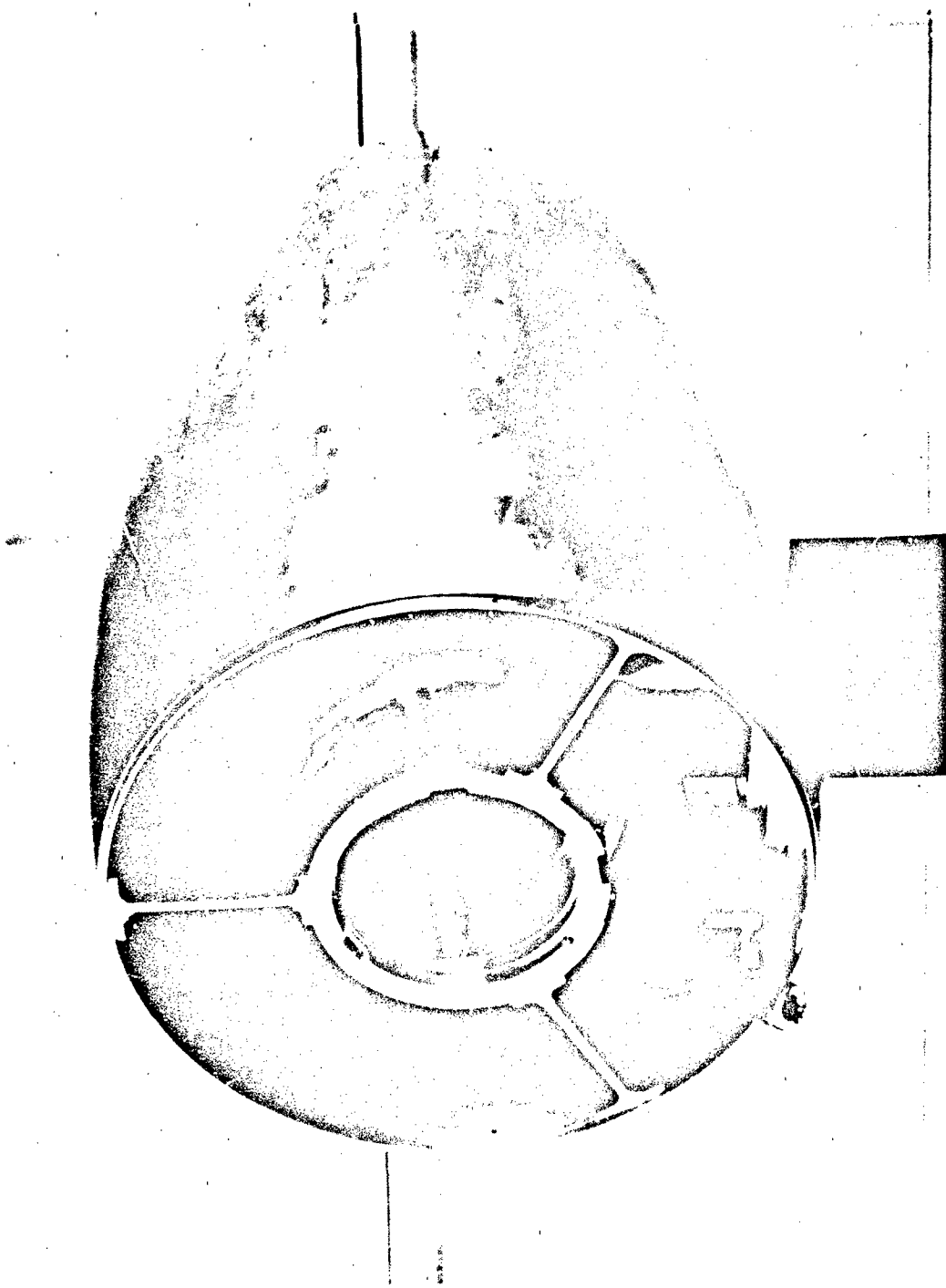


FIG.4 - PHOTO OF INTERMEDIATE HULL SECTION ATTACHED TO FOREBODY

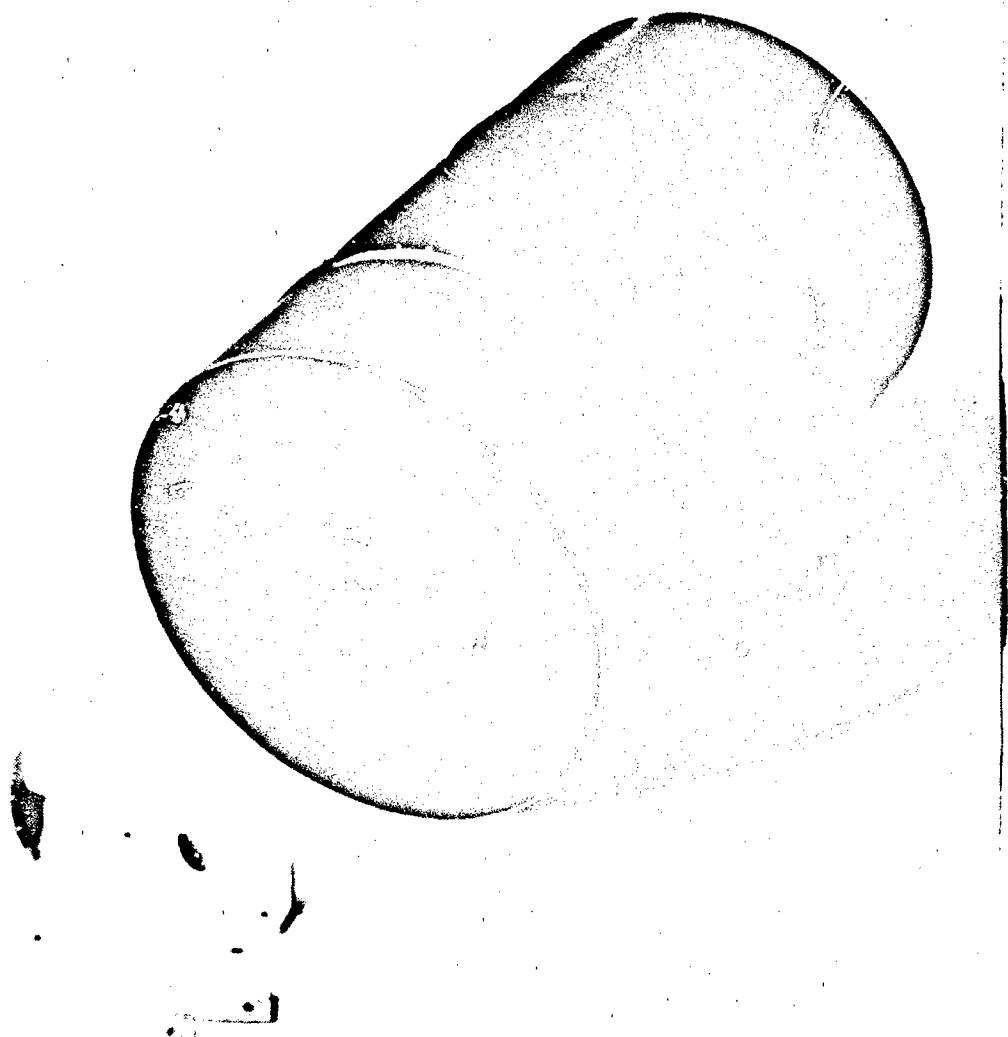


FIG.5 - PHOTO OF DYNAMIC AIR ENGINEERING, INC. SUCTION AND PROPULSION FAN

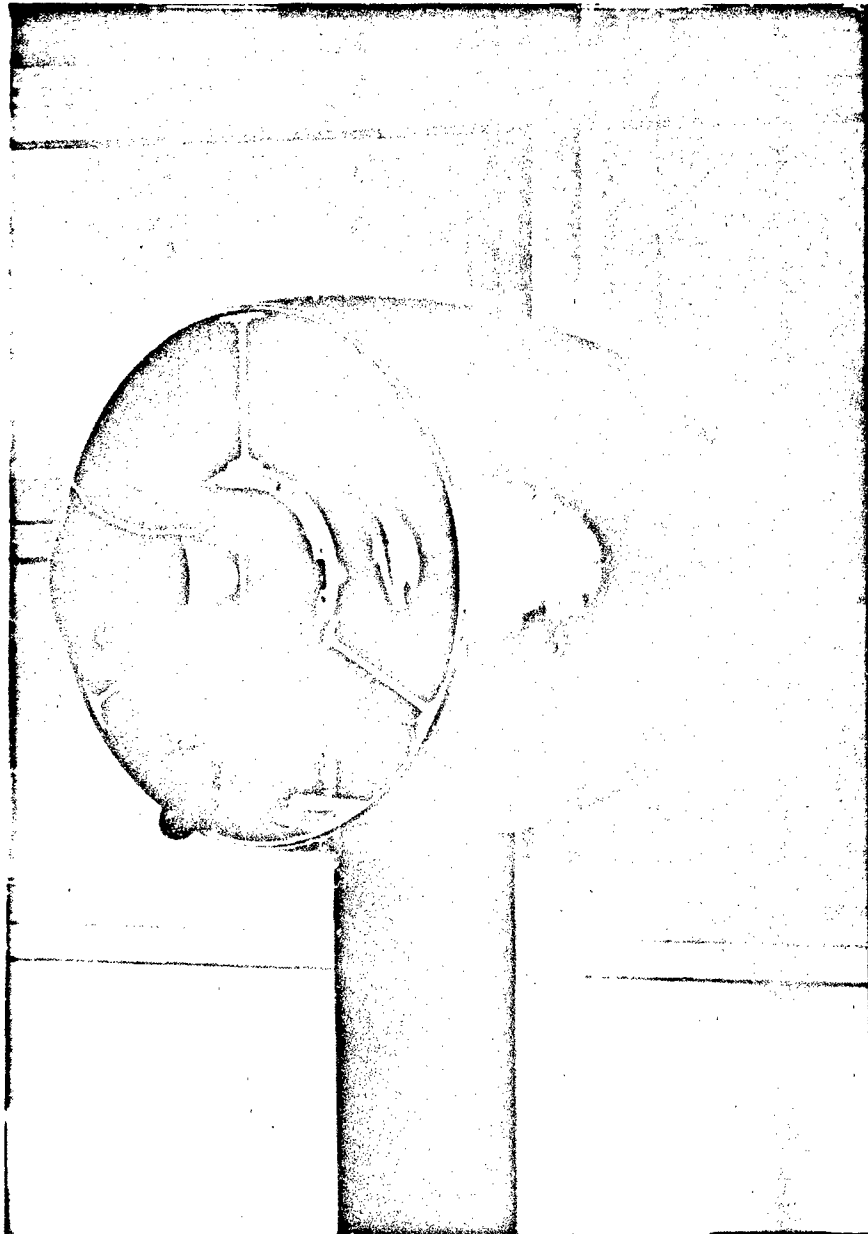


FIG.6 - PHOTO OF FAN INSTALLED IN CENTRAL RING, WITH INTERMEDIATE HULL SECTION ATTACHED TO FOREBODY

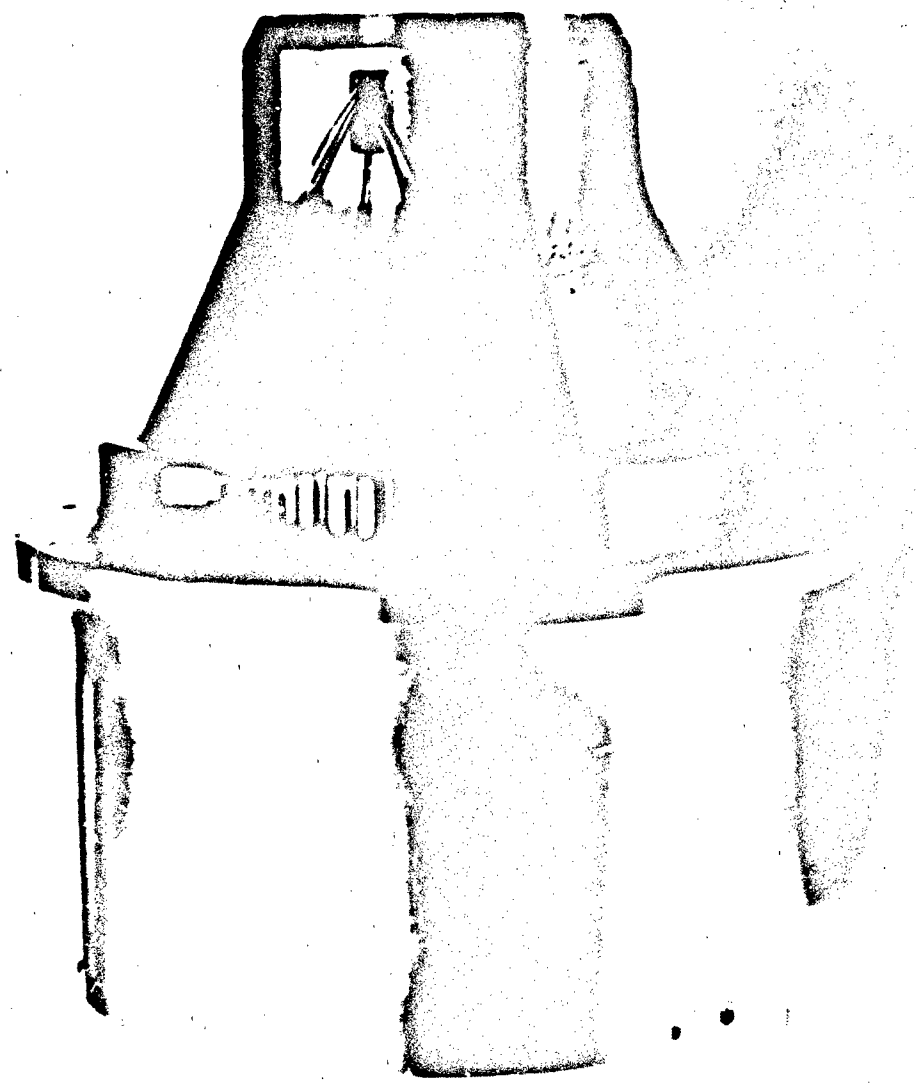


FIG.7 - PHOTO OF JET DISCHARGE NOZZLE ASSEMBLY

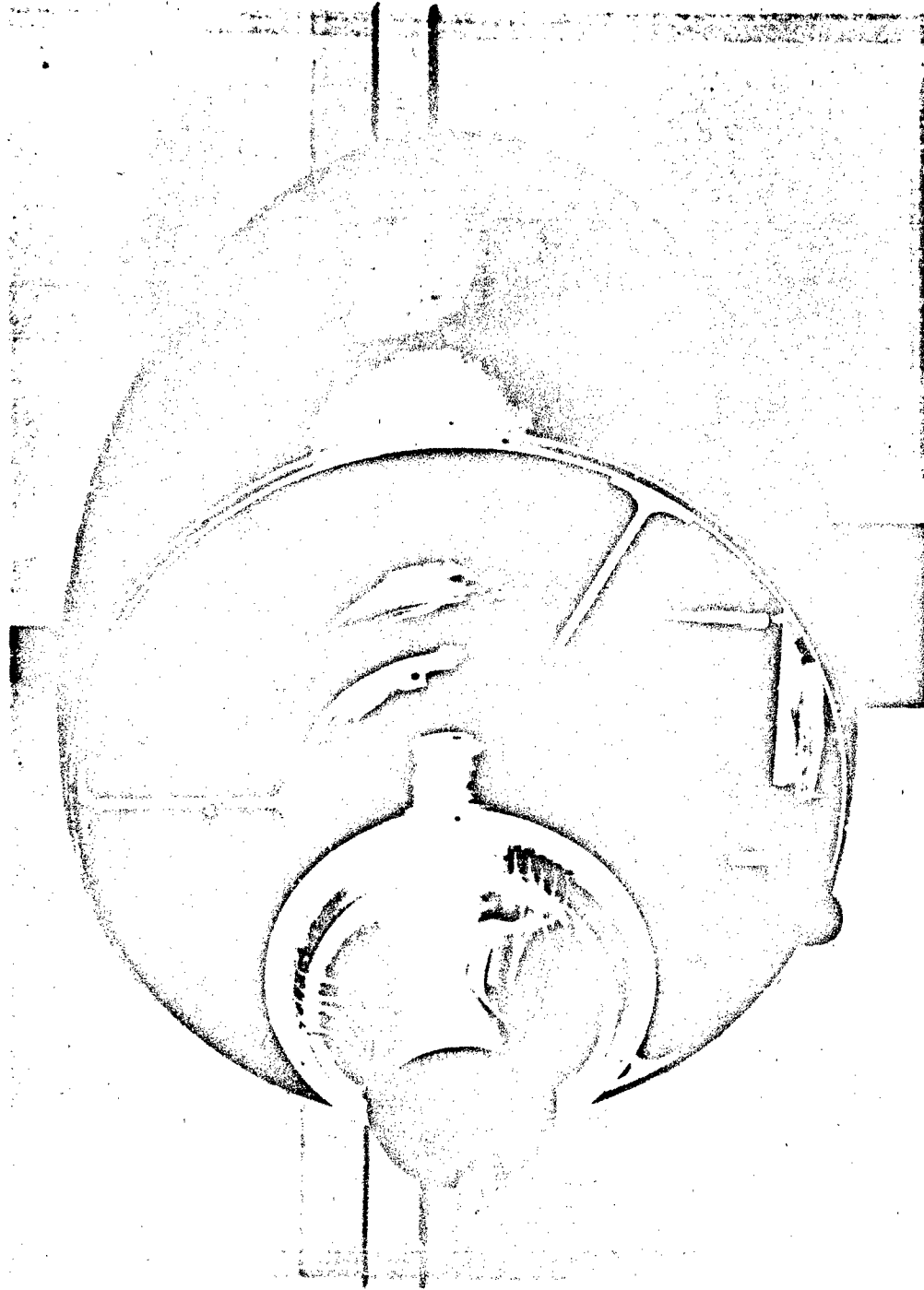


FIG. 8 - PHOTO OF JET DISCHARGE NOZZLE MOUNTED ON FAN: FAN INSTALLED IN CENTRAL RING, WITH INTERMEDIATE HULL SECTION ATTACHED TO FOREBODY

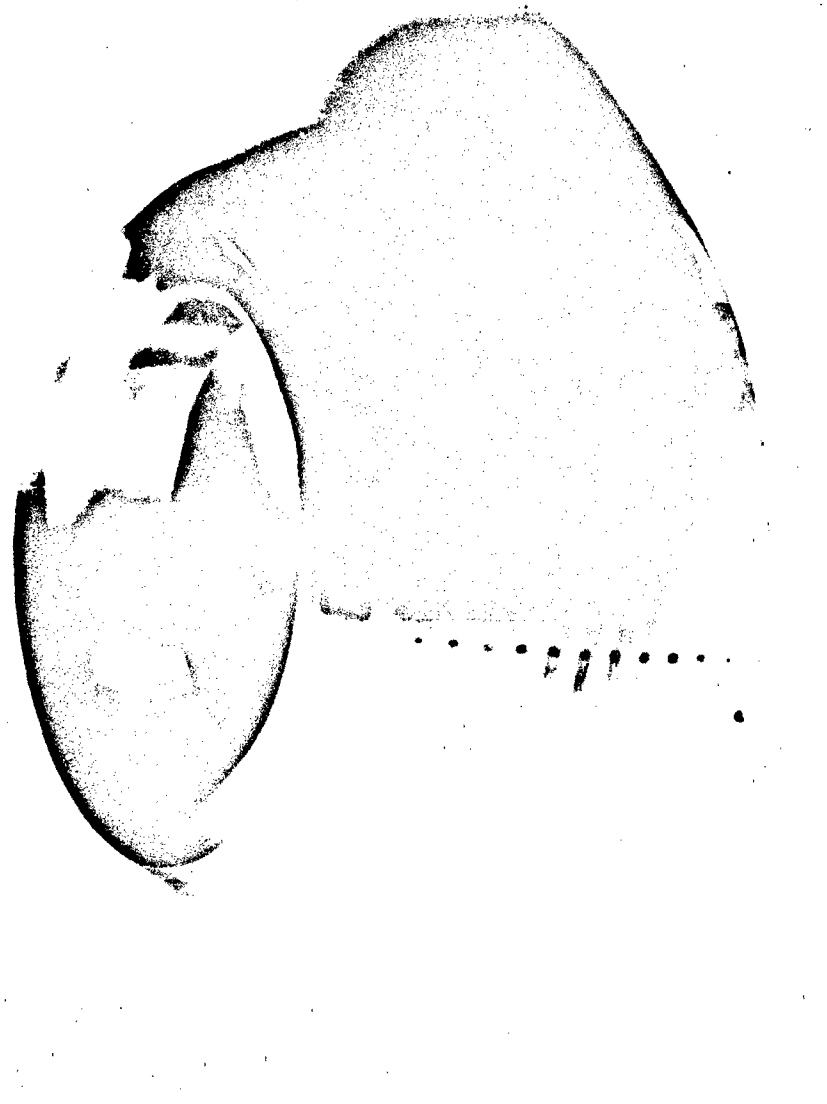
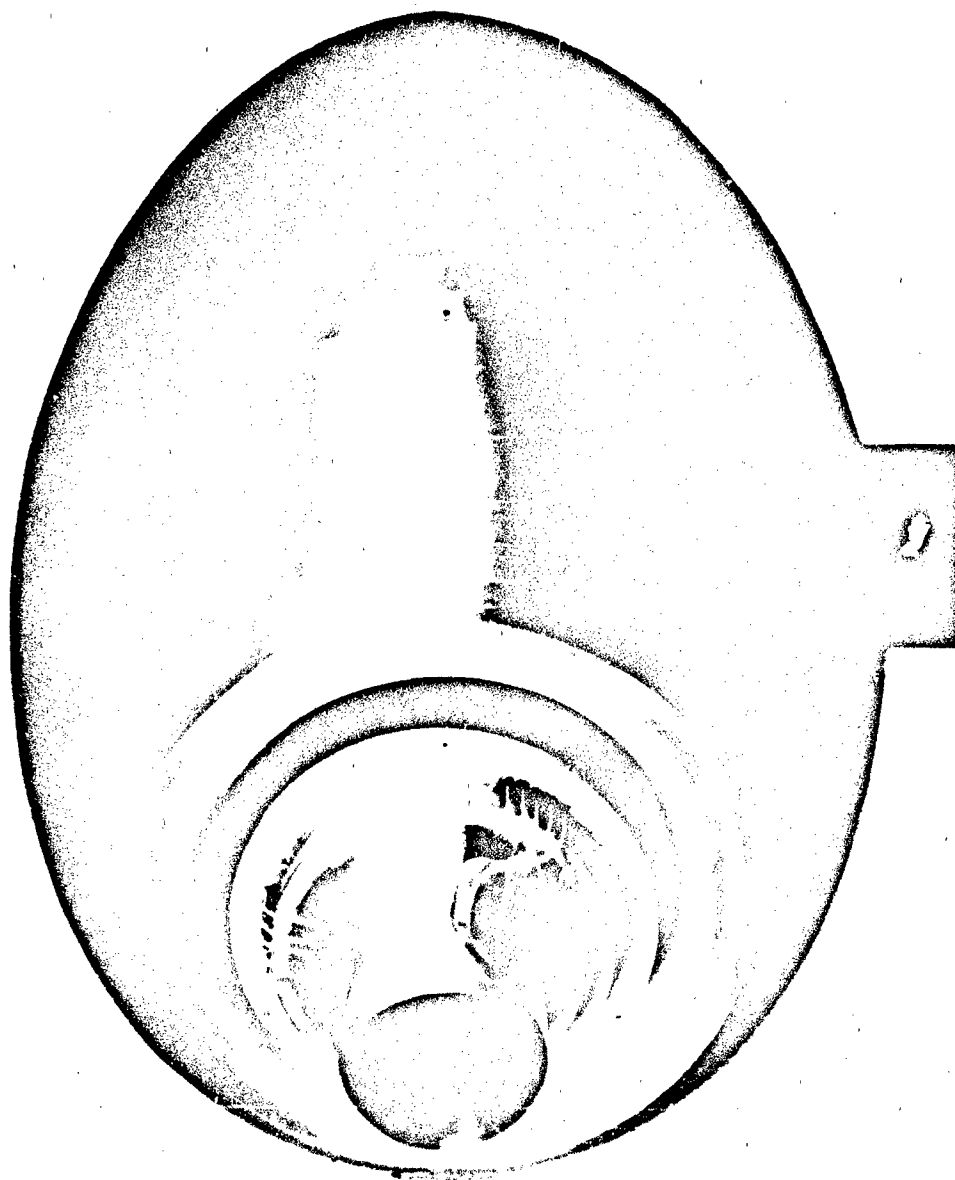


FIG.9 - PHOTO OF END SECTION OF HULL, SHOWING SHARP EDGE OF
RINGLOEB CUSP

FIG.10 - PHOTO OF INSTALLATION OF END SECTION OF HULL



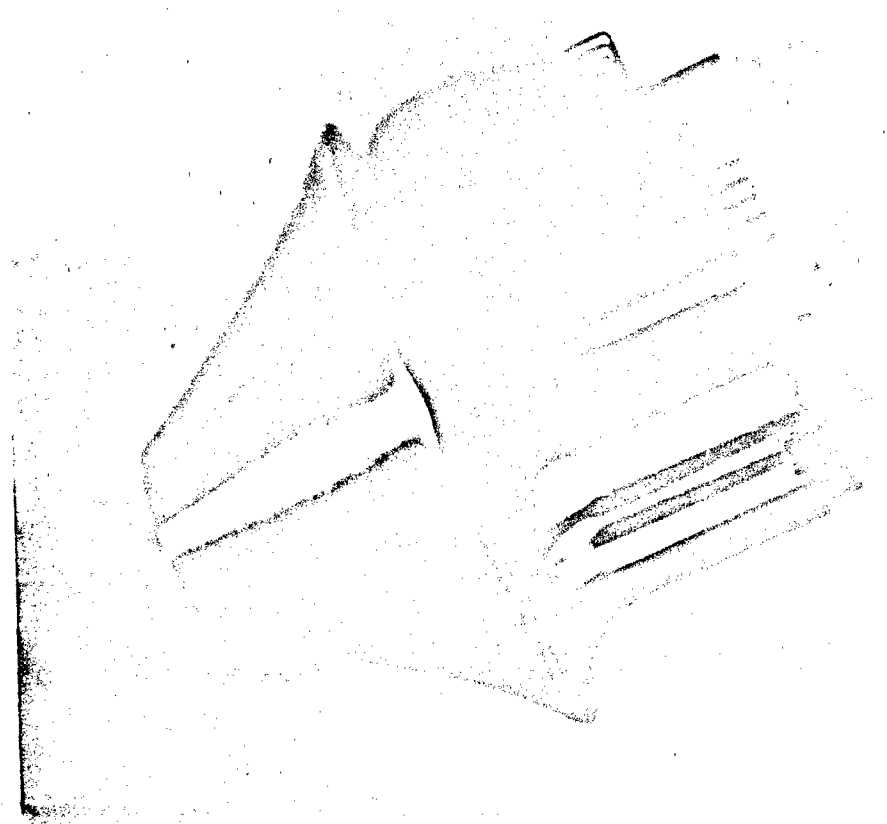


FIG.11 - PHOTO OF OPEN - JET AFTBODY

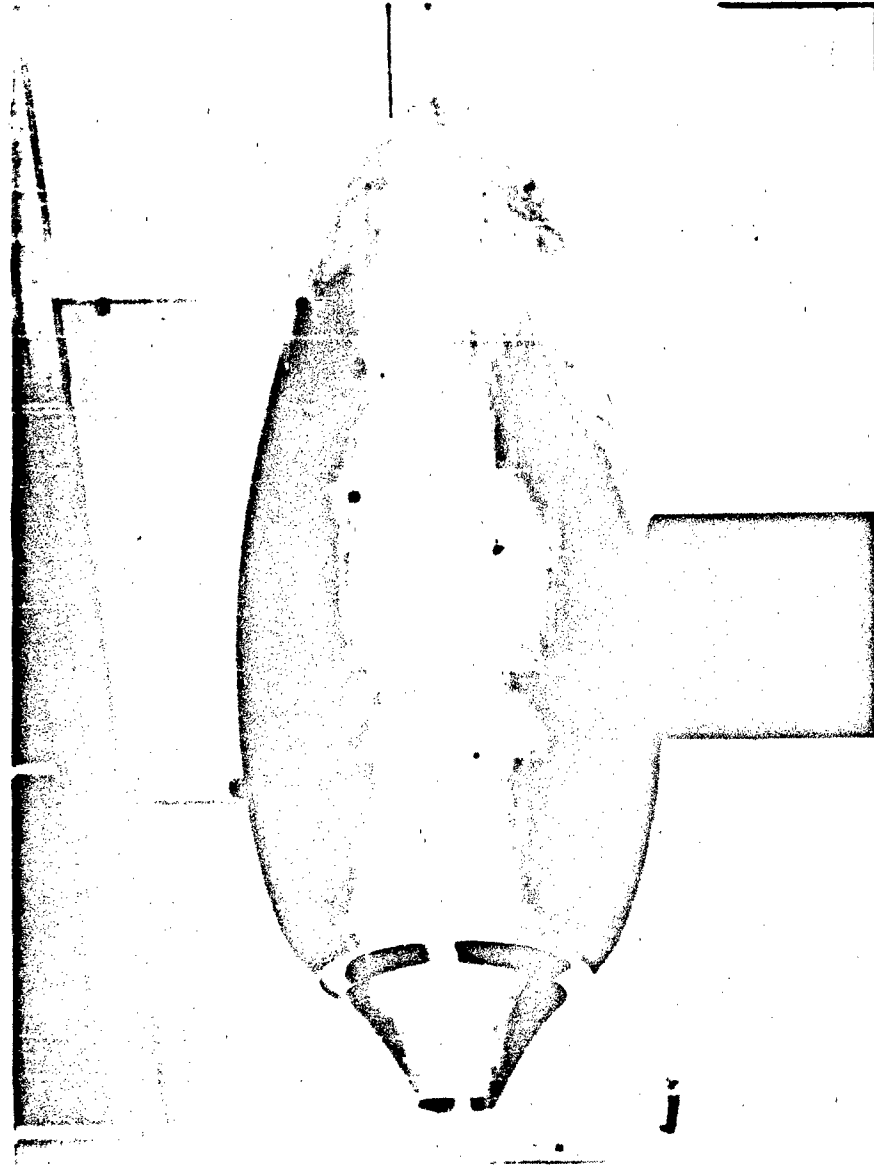


FIG. 12 - STARBOARD PHOTO VIEW OF COMPLETE TEST MODEL WITH OPEN - JET AFTBODY
(CONFIGURATION 0)

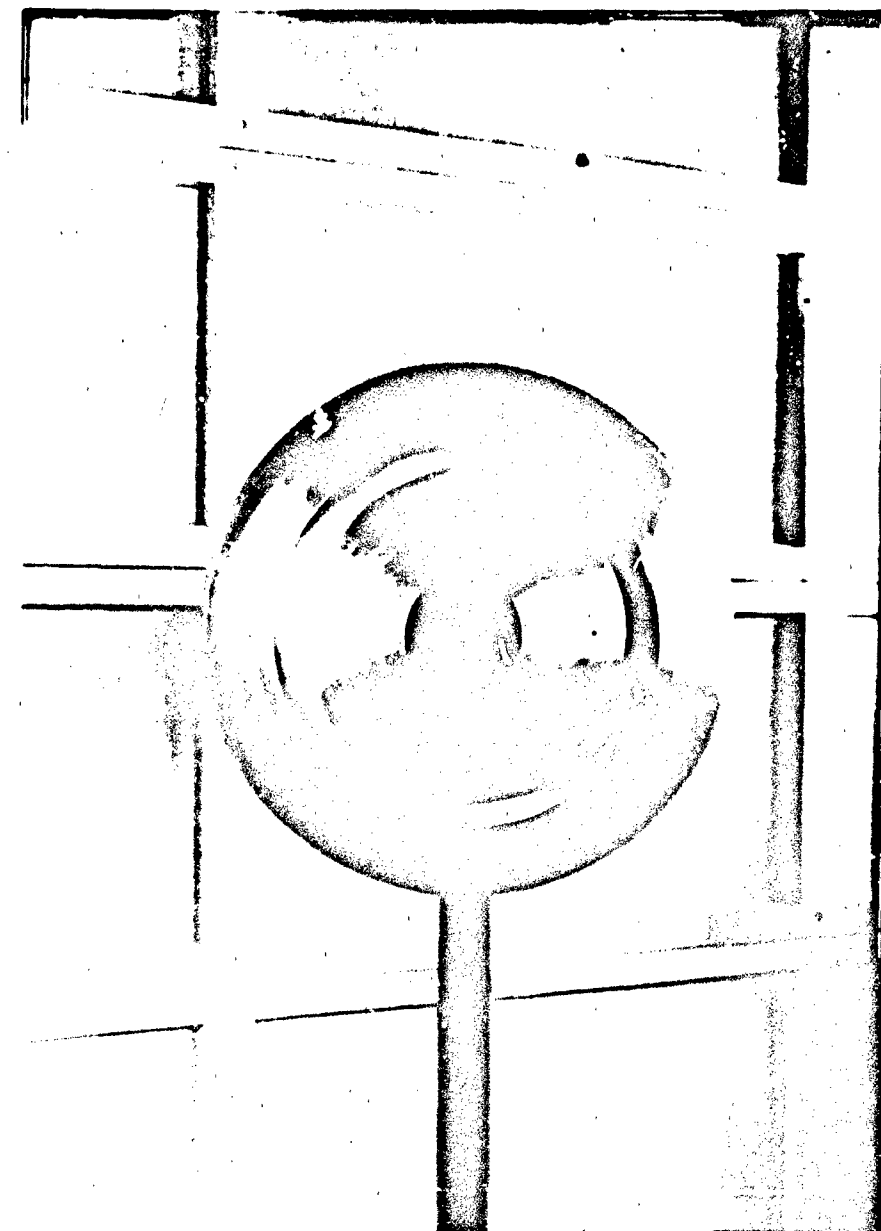


FIG.13 - STERN PHOTO VIEW OF COMPLETE TEST MODEL WITH OPEN -
JET AFTBODY (CONFIGURATION '0')

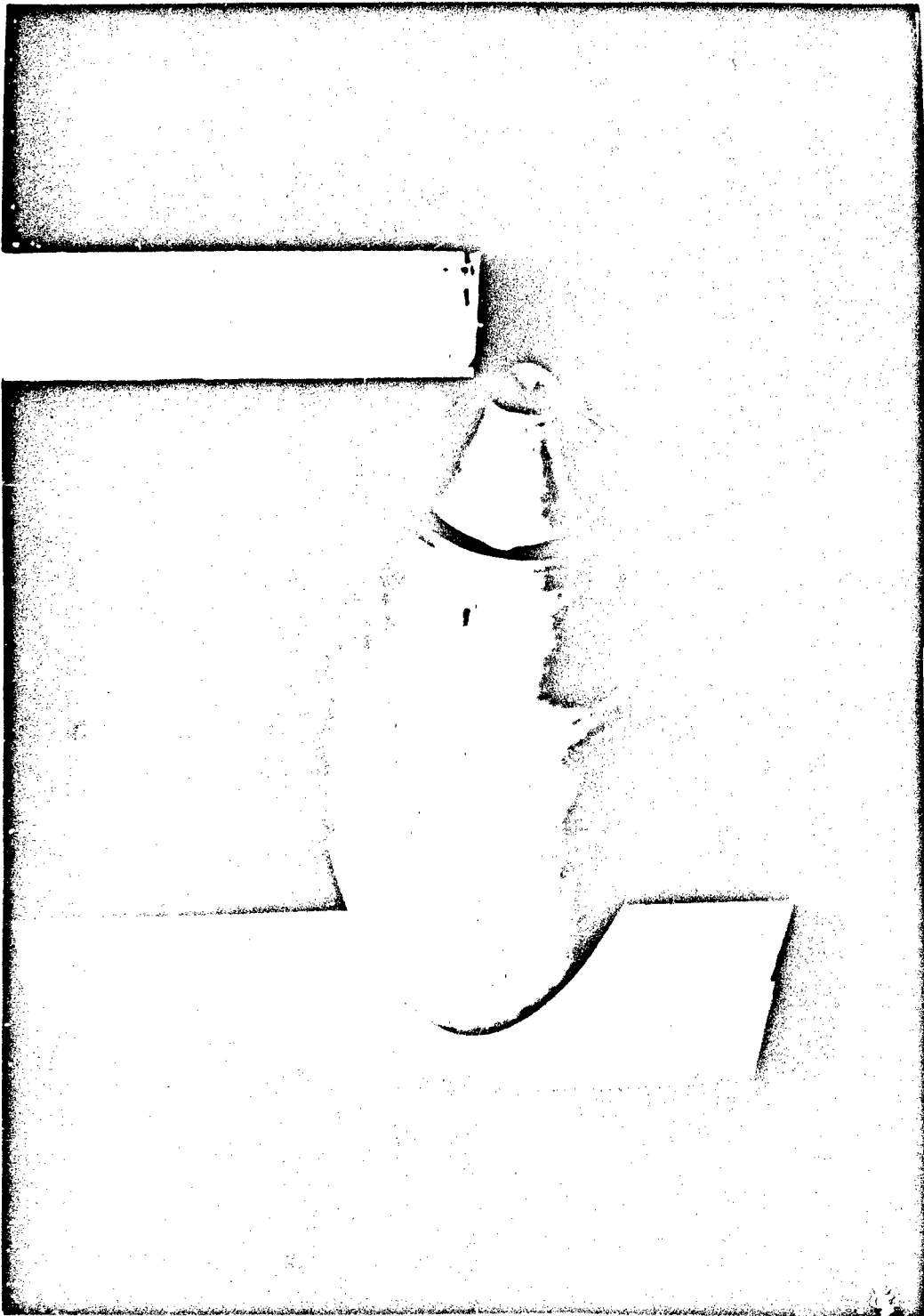


FIG. 14 - PHOTO OF WIND TUNNEL INSTALLATION OF TEST MODEL WITH OPEN - JET AFTBODY
(CONFIGURATION 0)



FIG. 15 - PHOTO OF WIND TUNNEL INSTALLATION OF TEST MODEL WITH TAILBOOM AFTBODY
(CONFIGURATION 1)

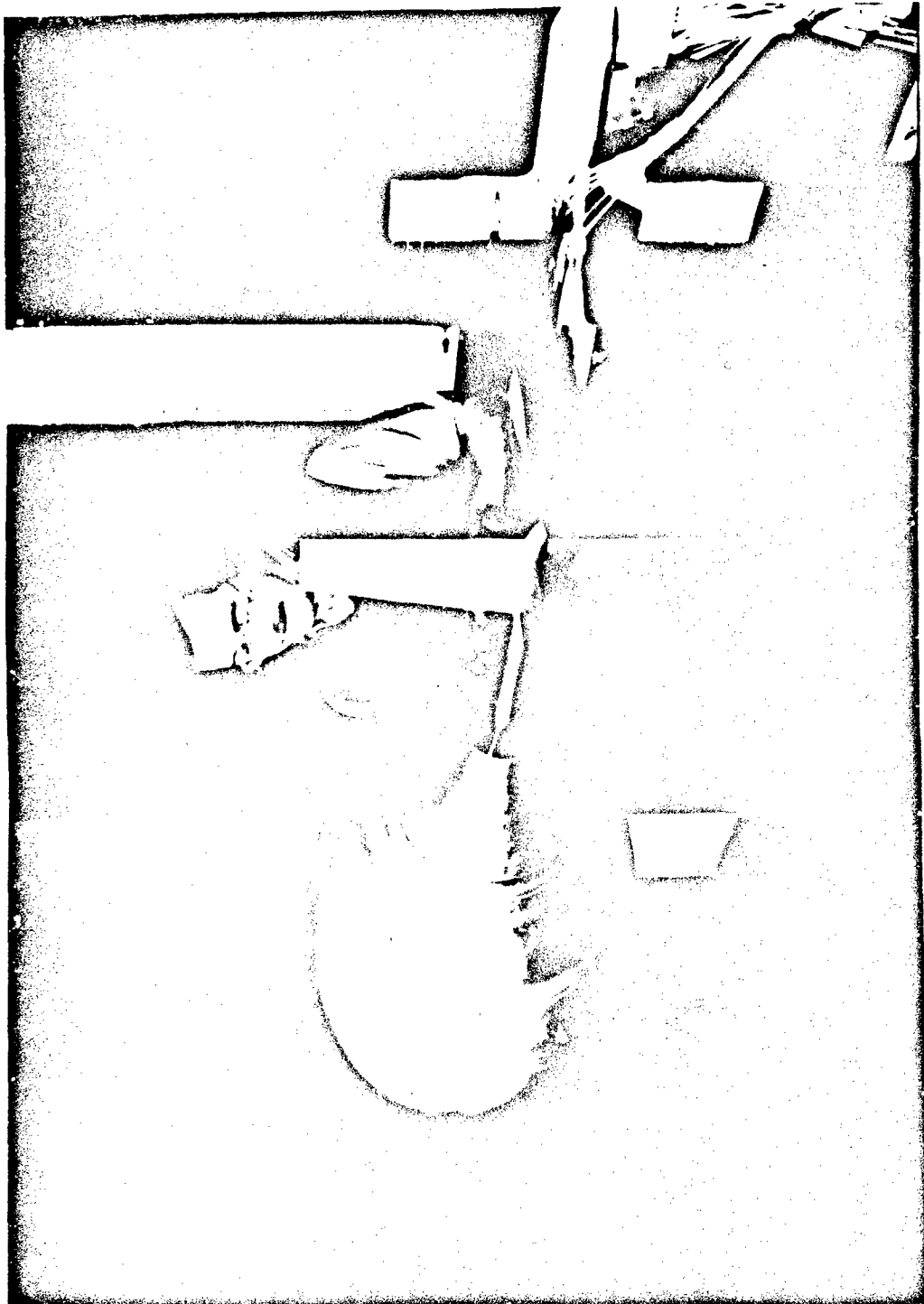


FIG. 16 - PHOTO OF WIND TUNNEL INSTALLATION OF TEST MODEL WITH TAILBOOM AFTBODY AND EMPENNAGE (CONFIGURATION 2), SHOWING ALSO THE WAKE RAKE ASSEMBLY

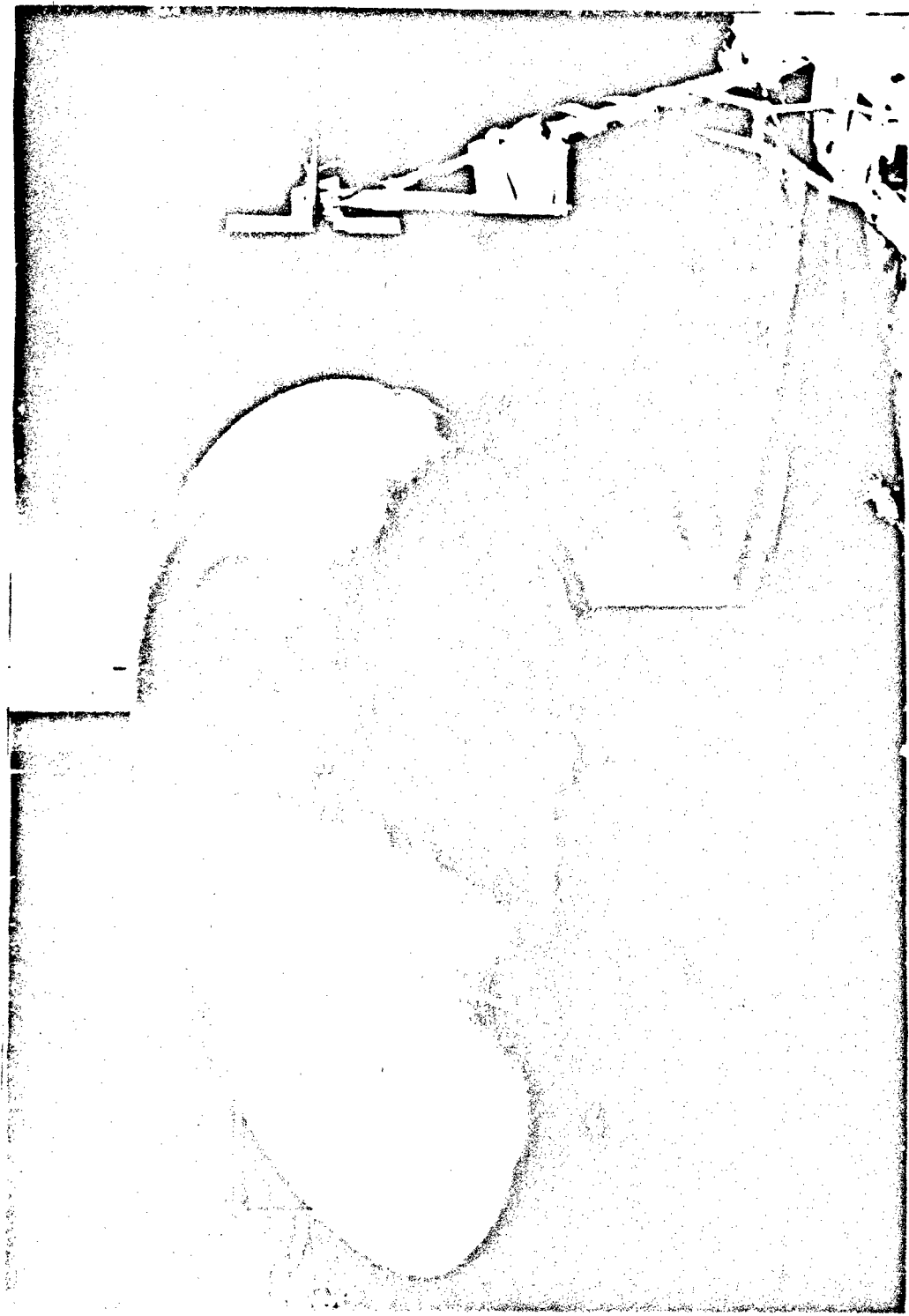


FIG. 17 - BOW PHOTO VIEW OF WIND TUNNEL INSTALLATION OF TEST MODEL WITH TRANSITION
TRIP AT 10% LENGTH, SHOWING ALSO THE WAKE RAKE ASSEMBLY

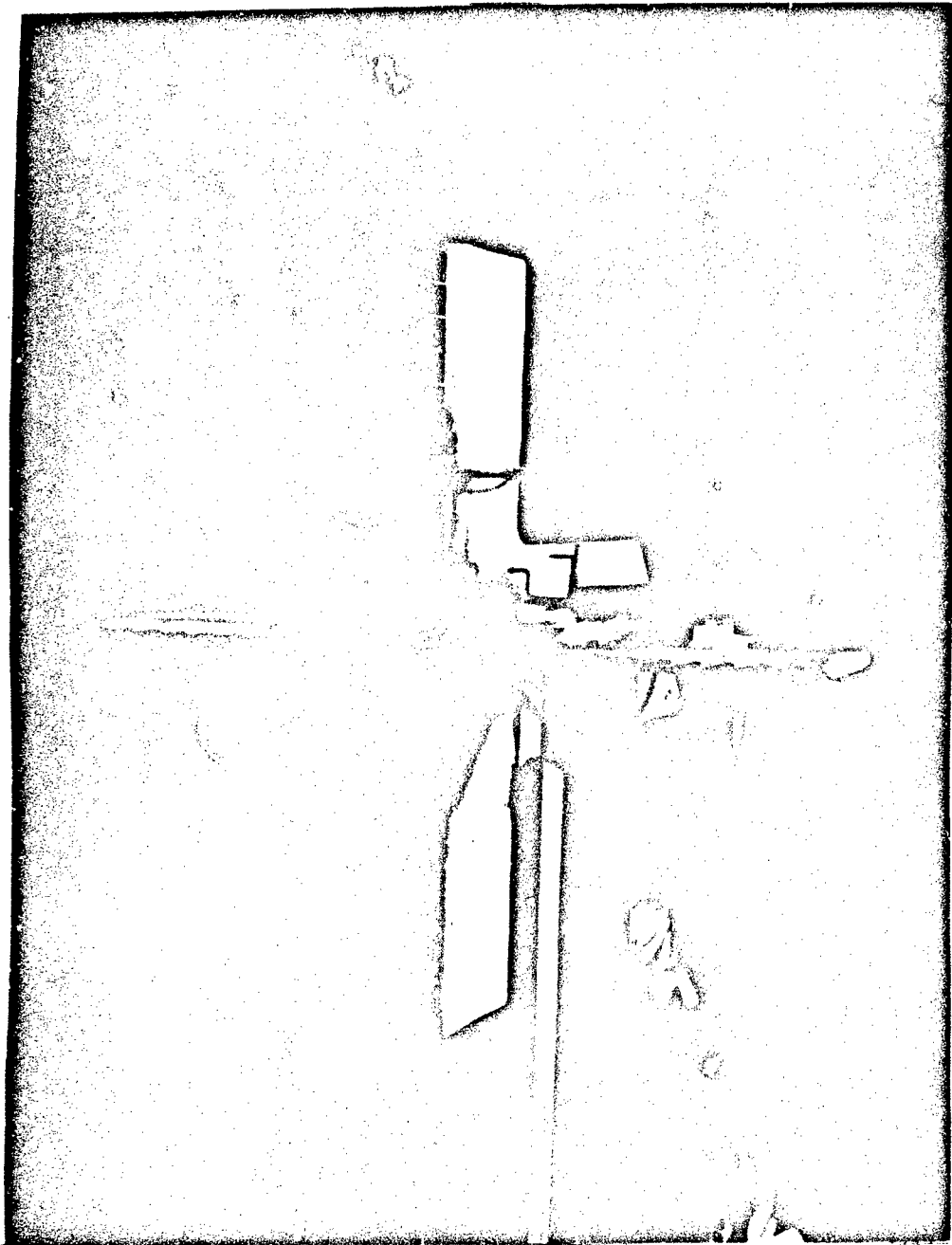


FIG.18 - PHOTO OF WAKE RAKE ASSEMBLY

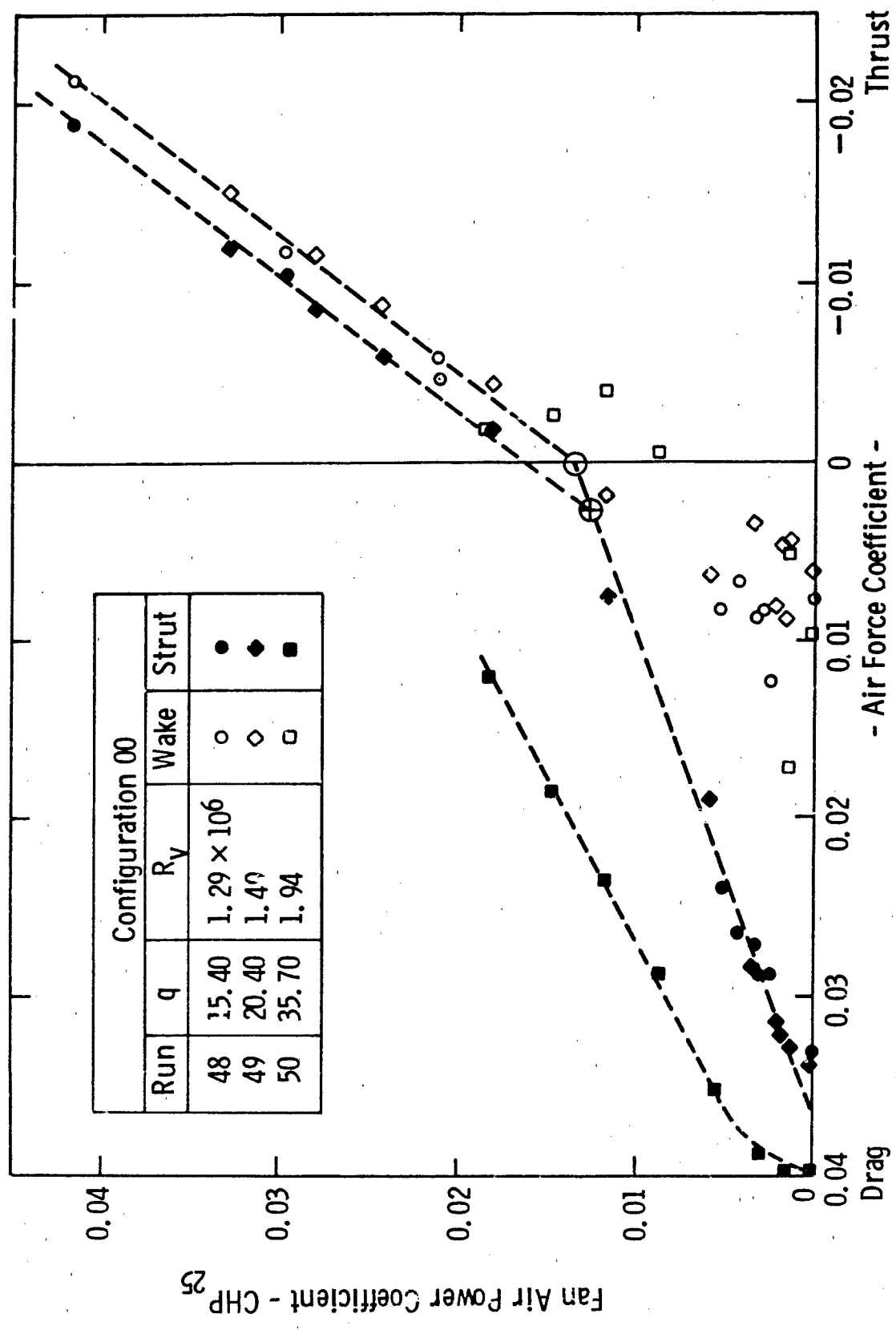


Fig. 19—Fan air power coefficient vs axial force coefficient-configuration 00

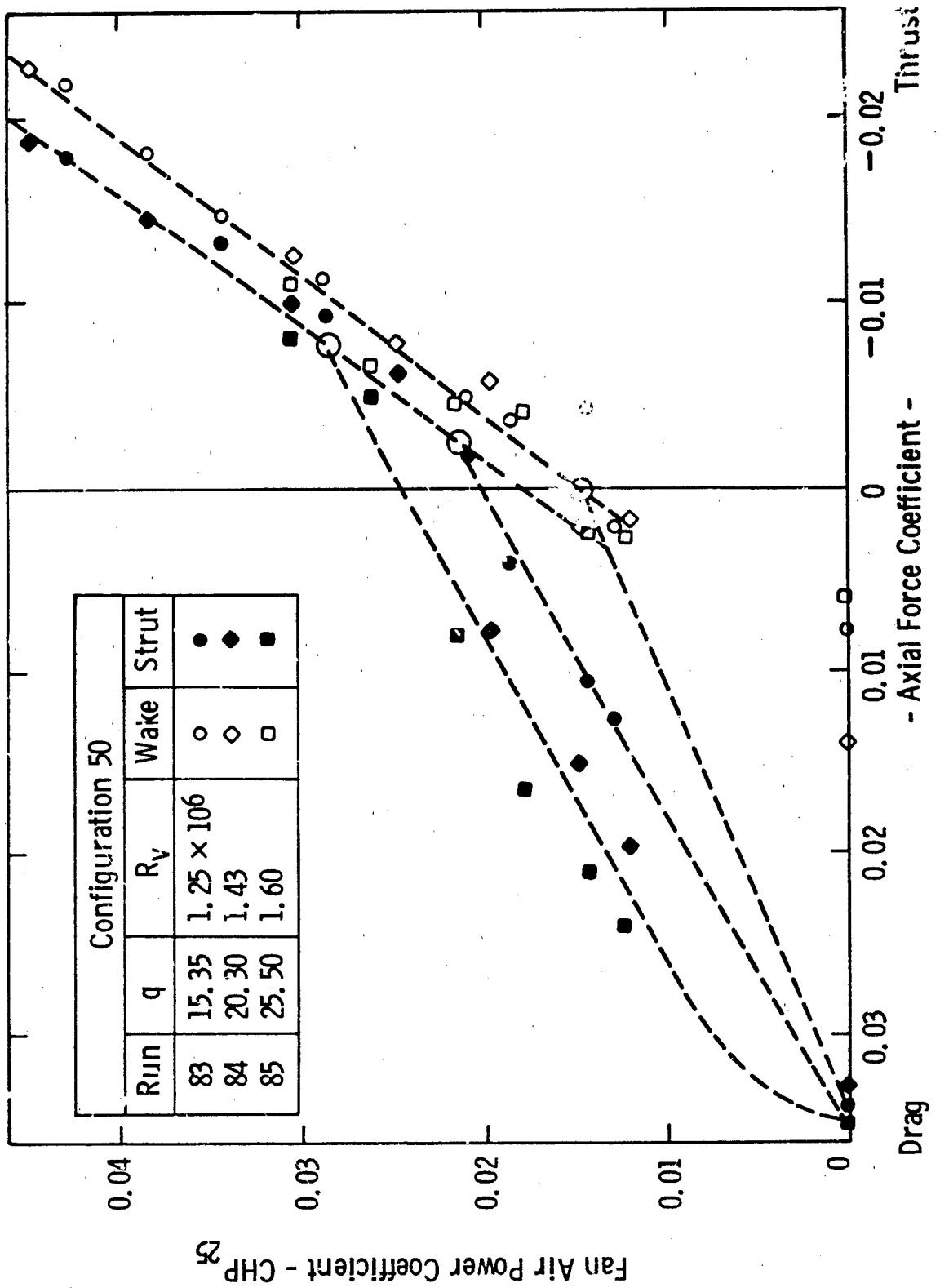


Fig. 20—Fan air power coefficient vs axial force coefficient-configuration 50

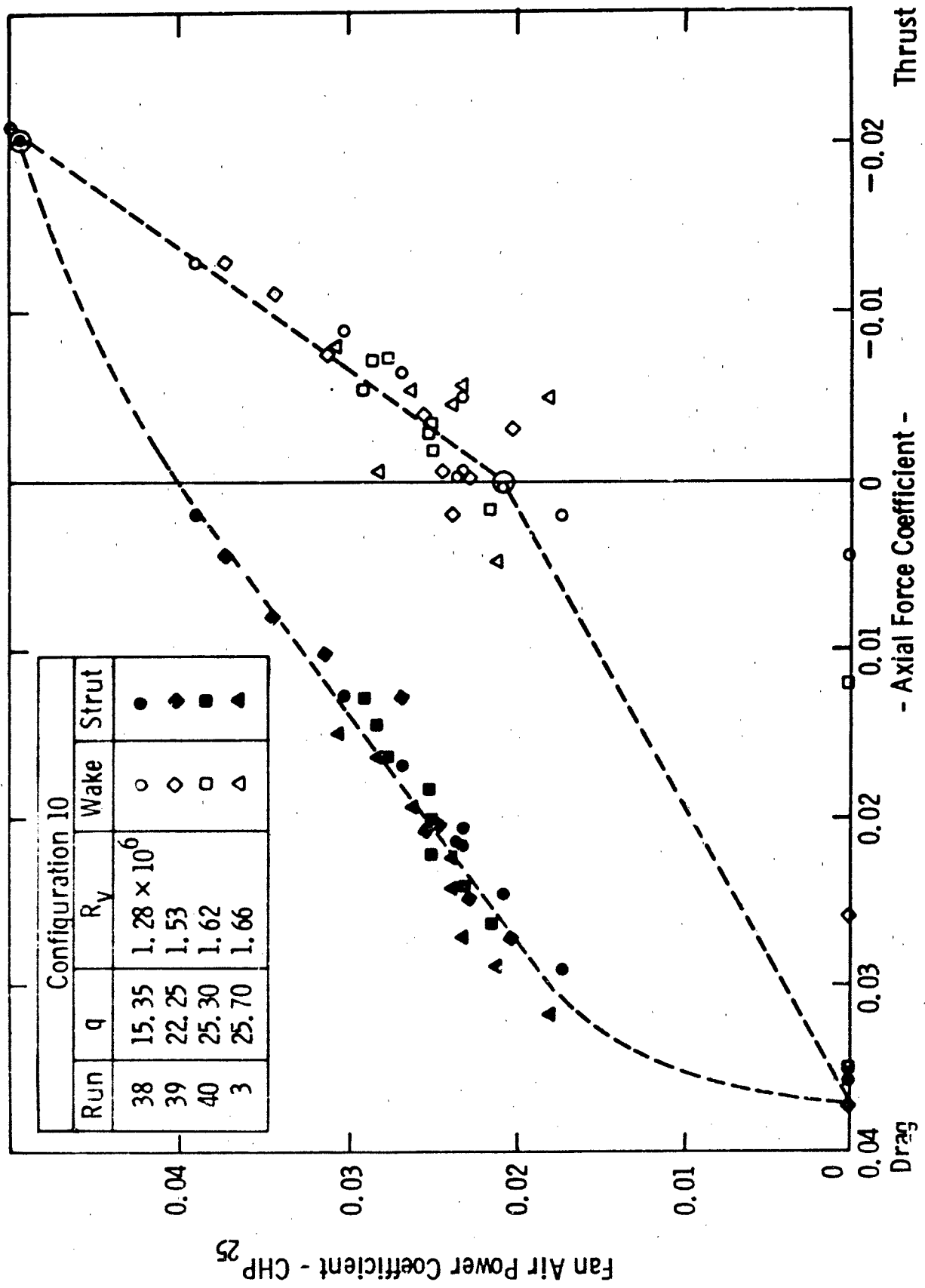


Fig. 21—Fan air power coefficient vs axial force coefficient—configuration 10

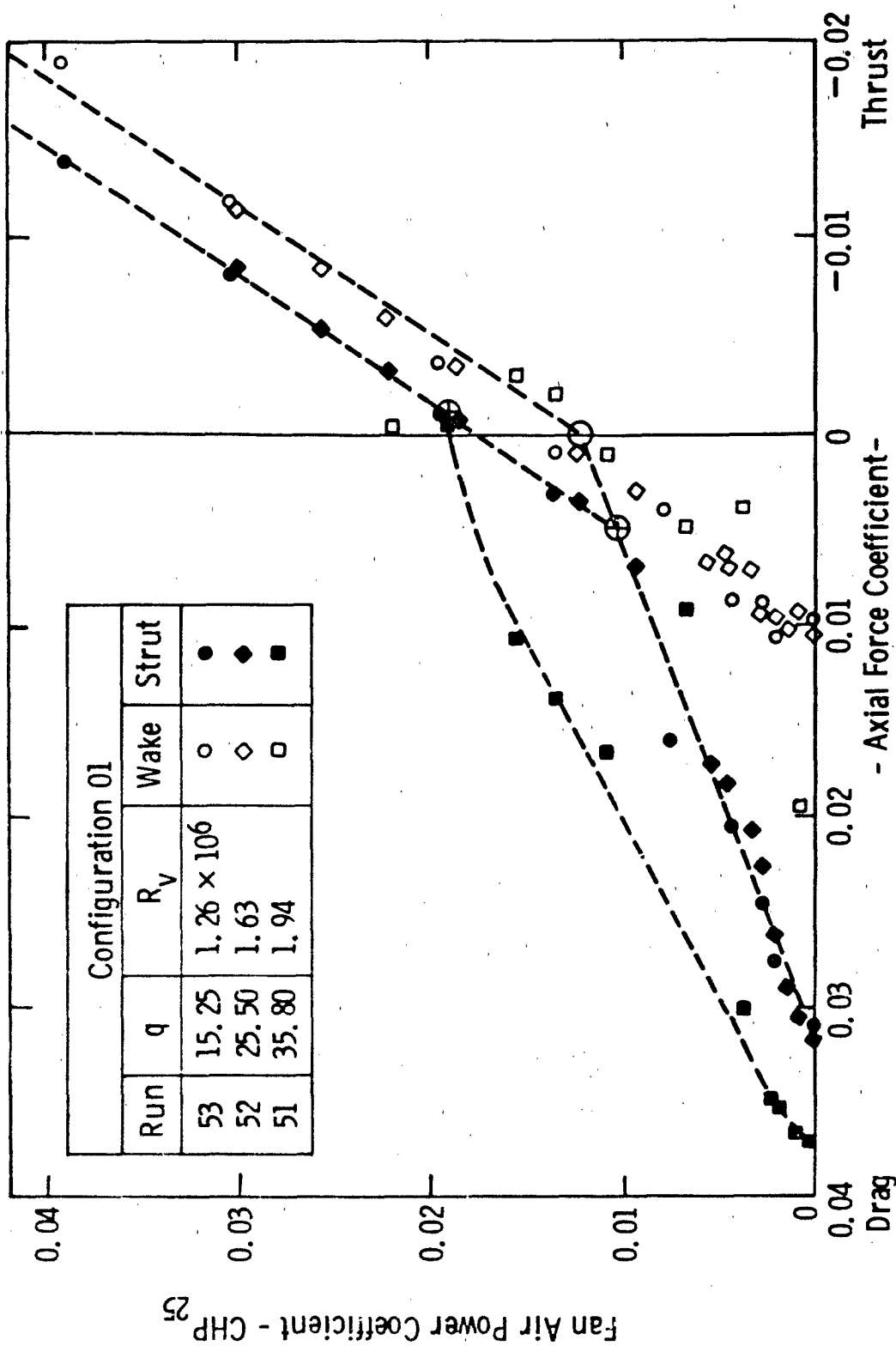


Fig. 22—Fan air power coefficient vs axial force coefficient-configuration 01

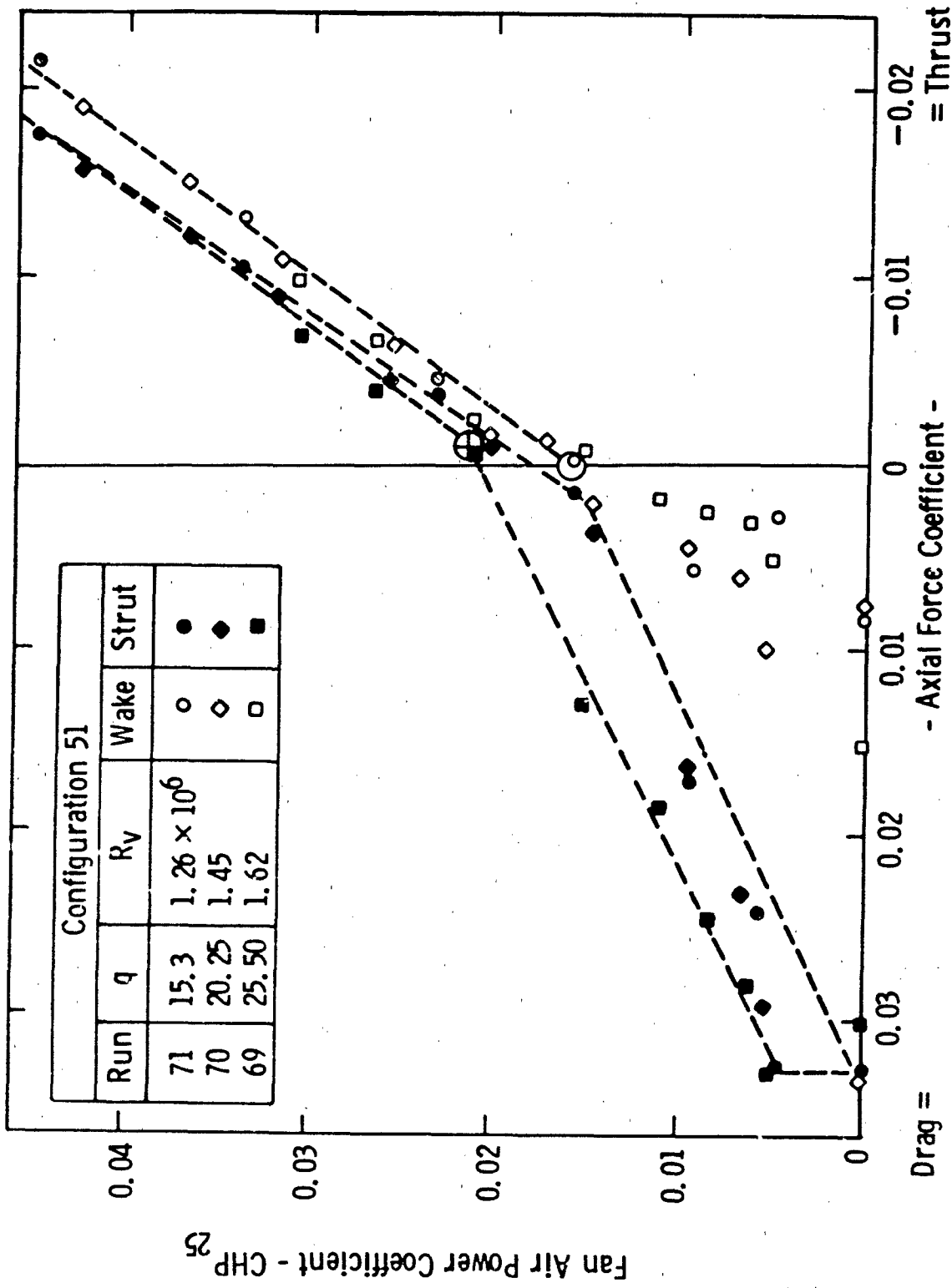


Fig. 23--Fan air power coefficient vs axial force coefficient-configuration 51

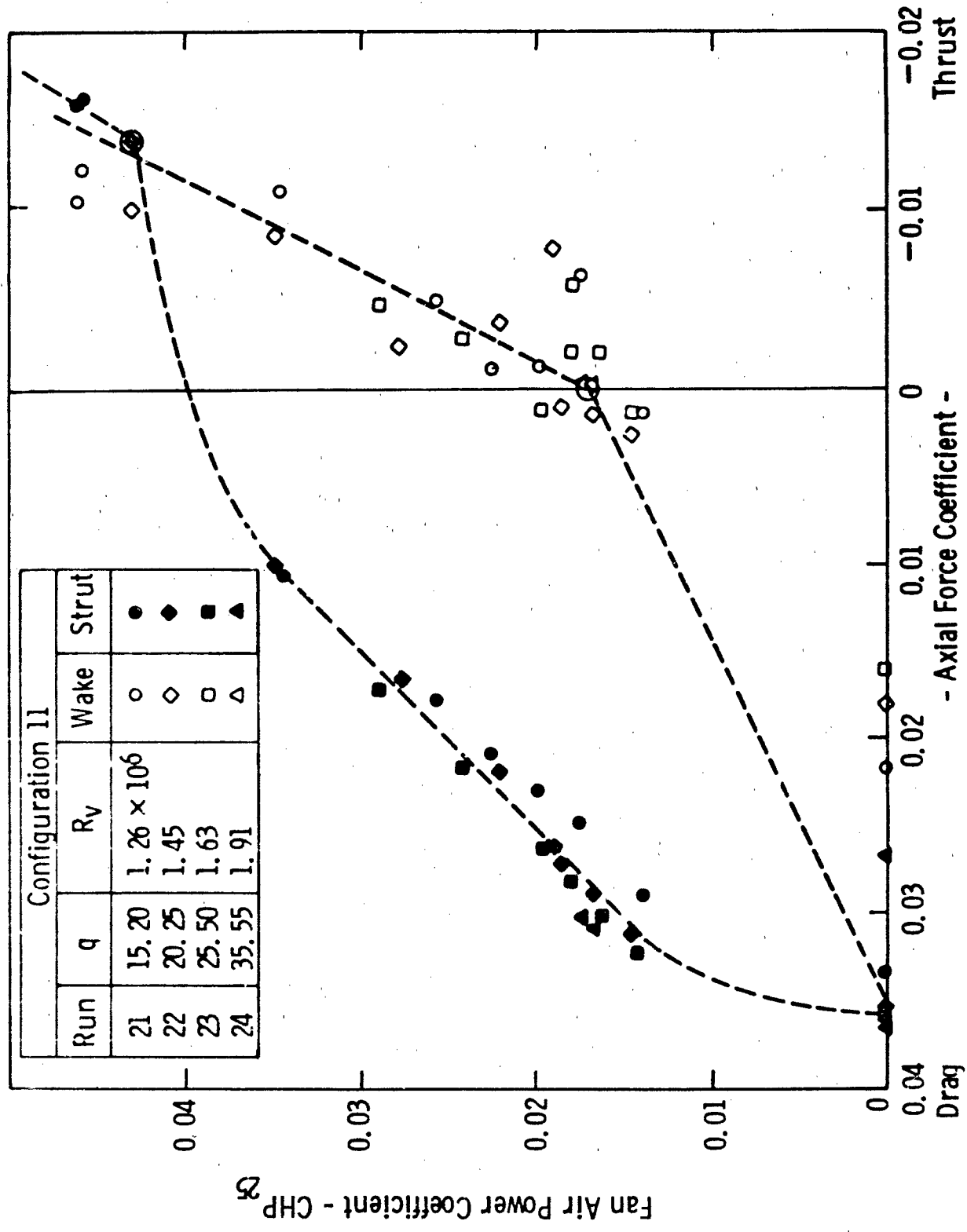


Fig. 24—Fan air power coefficient vs axial force coefficient-configuration 11

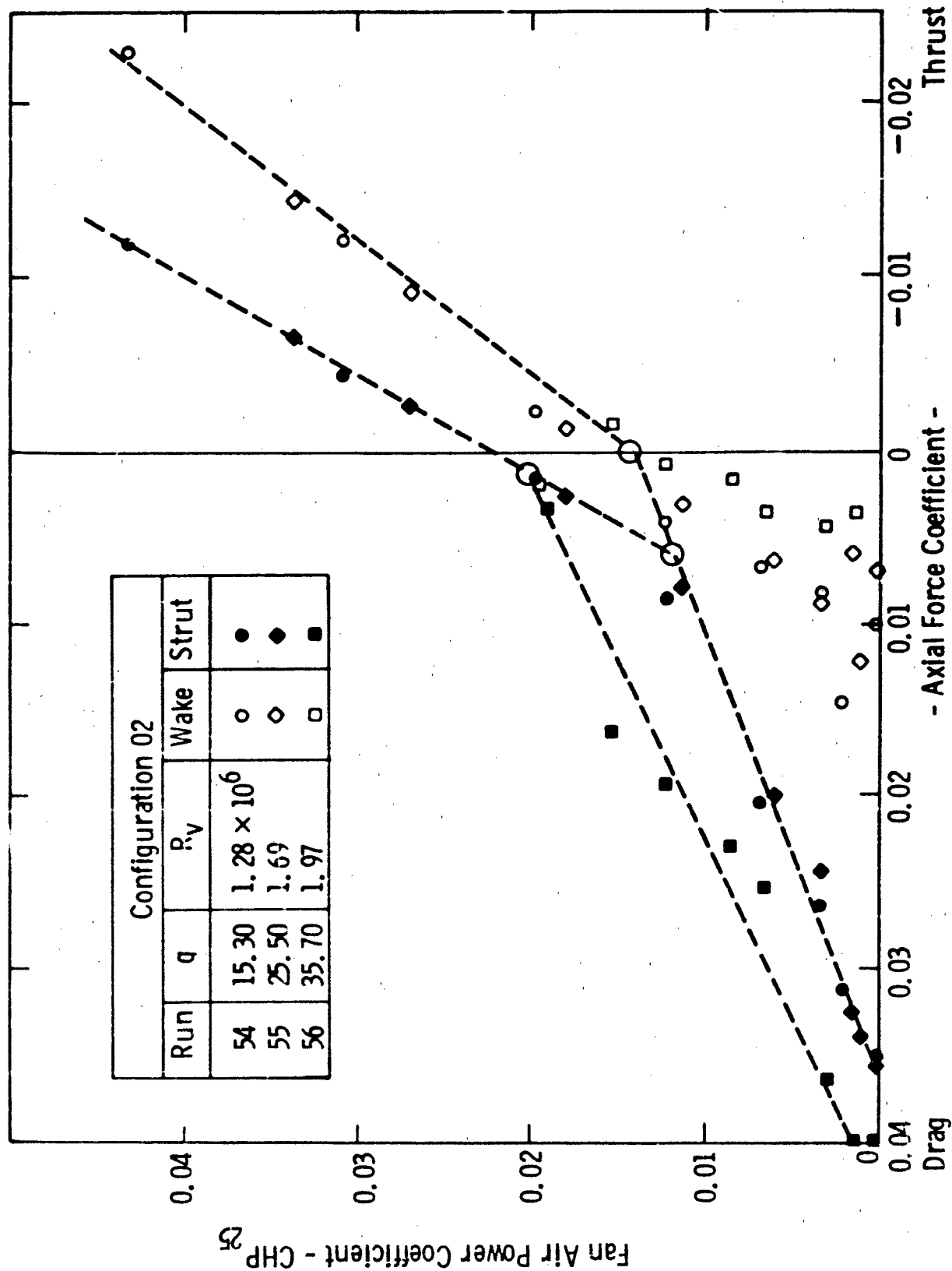


Fig. 25—Fan air power coefficient vs axial force coefficient configuration 02

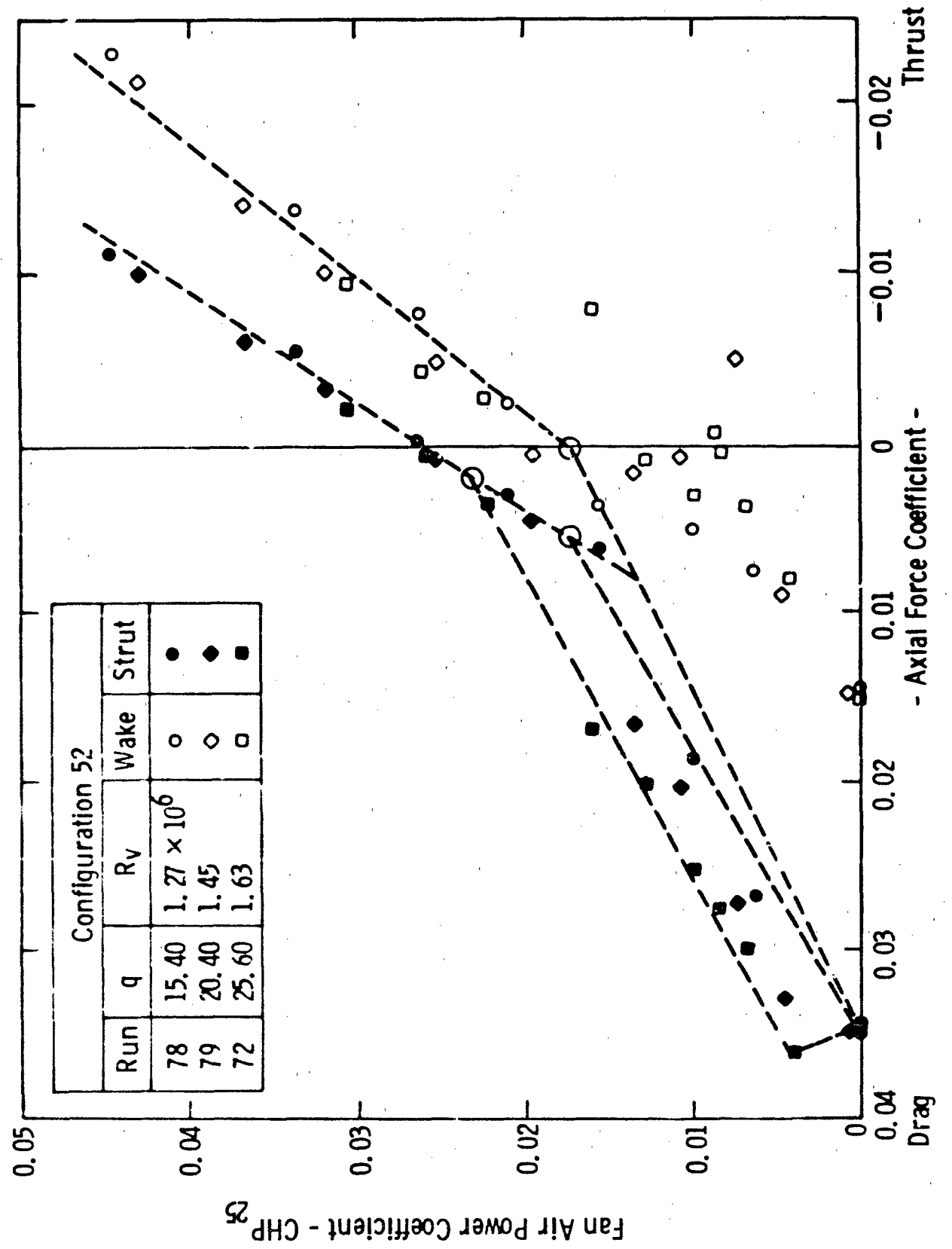


Fig. 26—Fan air power coefficient vs axial force coefficient-configuration 52

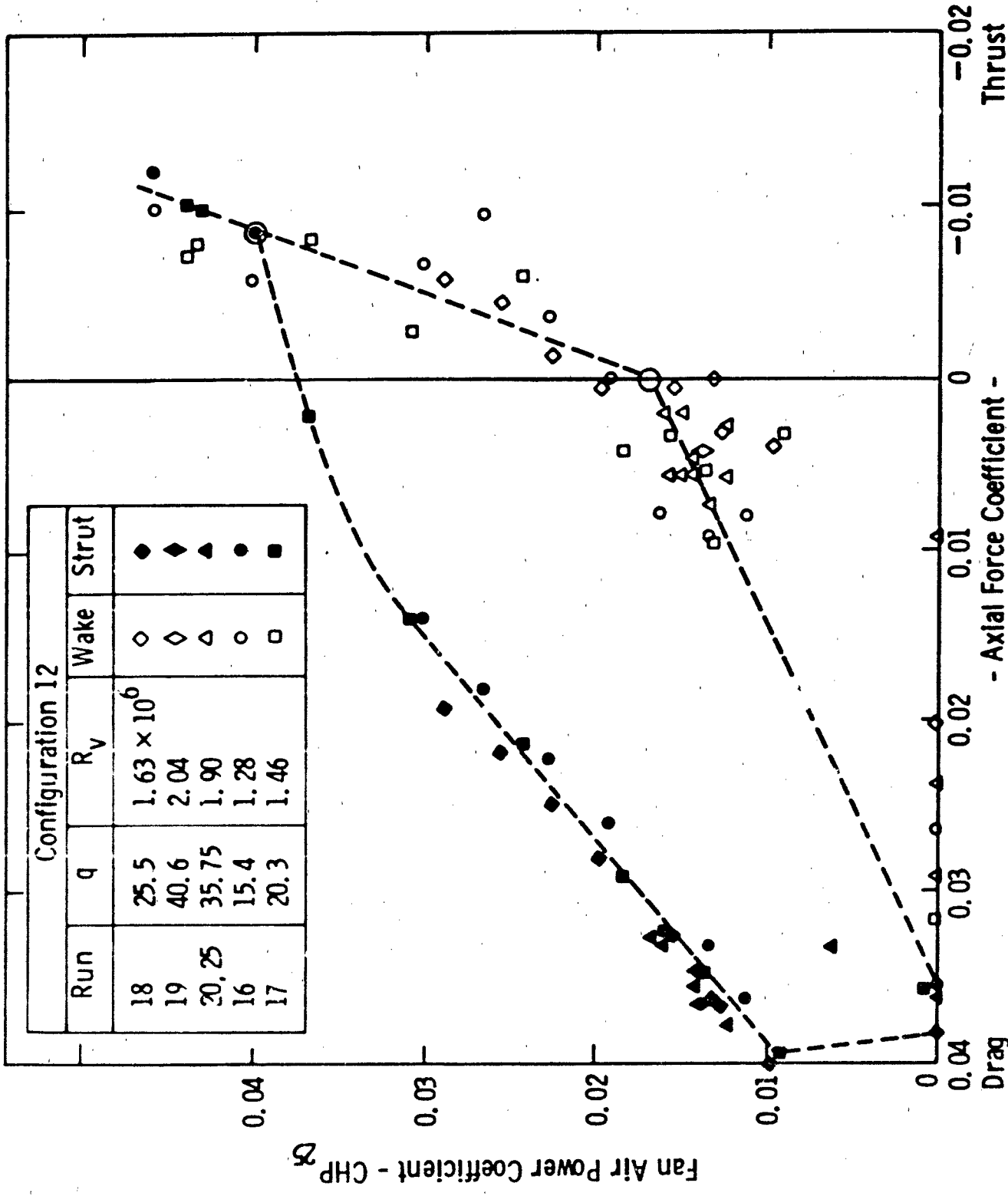


Fig. 27—Fan air power coefficients and force coefficients for Configuration 12 at $\alpha = 25^\circ$ and 27° .

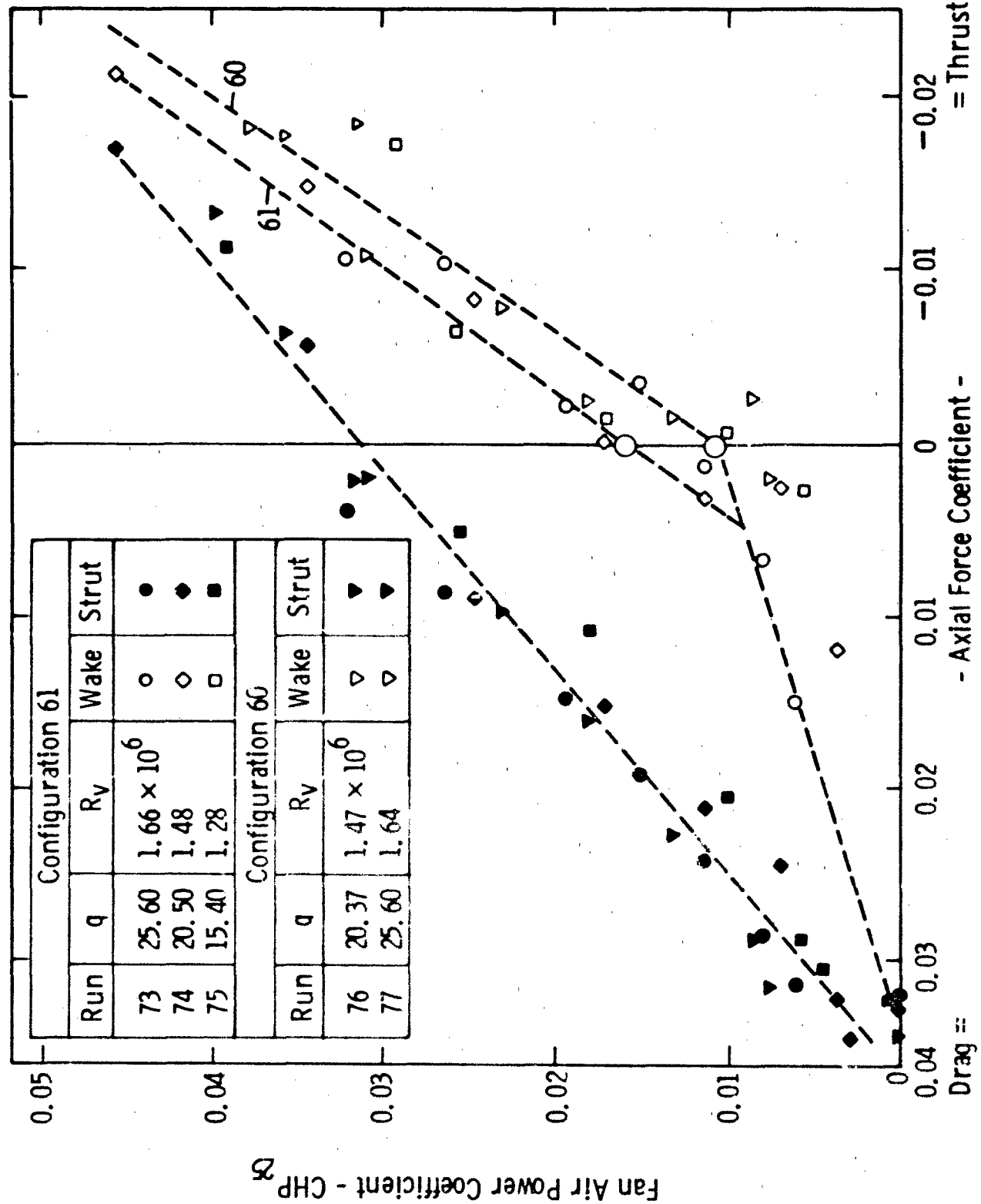


Fig. 28—Fan air power coefficient vs axial force coefficient-configuration 60 and 61

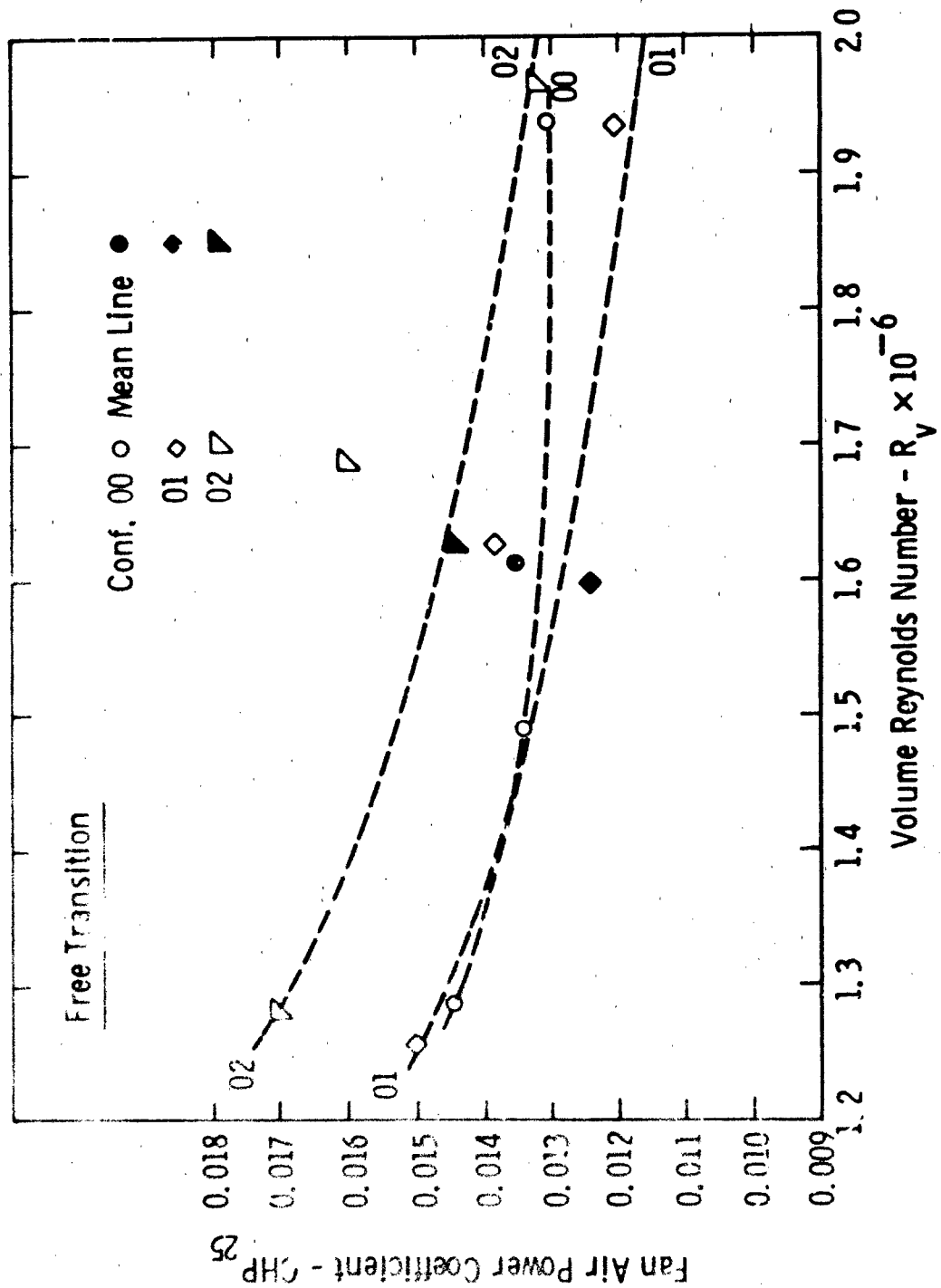


Fig. 29—Fan air power coefficient vs volume Reynolds number - configurations 00, 01 and 02 (free transition)

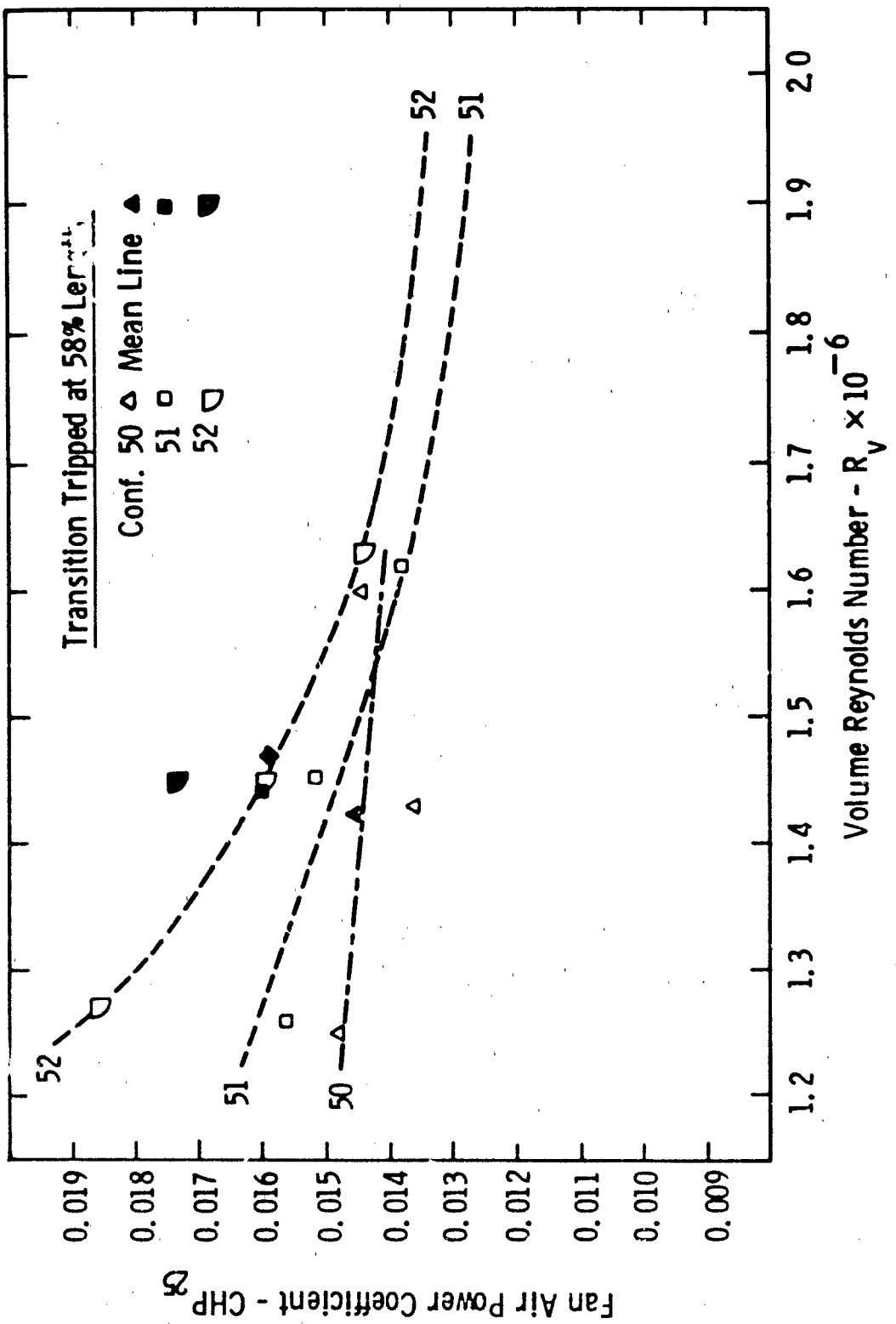


Fig. 30—Fan air coefficient vs volume Reynolds number - configurations 50, 51 and 52
(transition at 58% length)

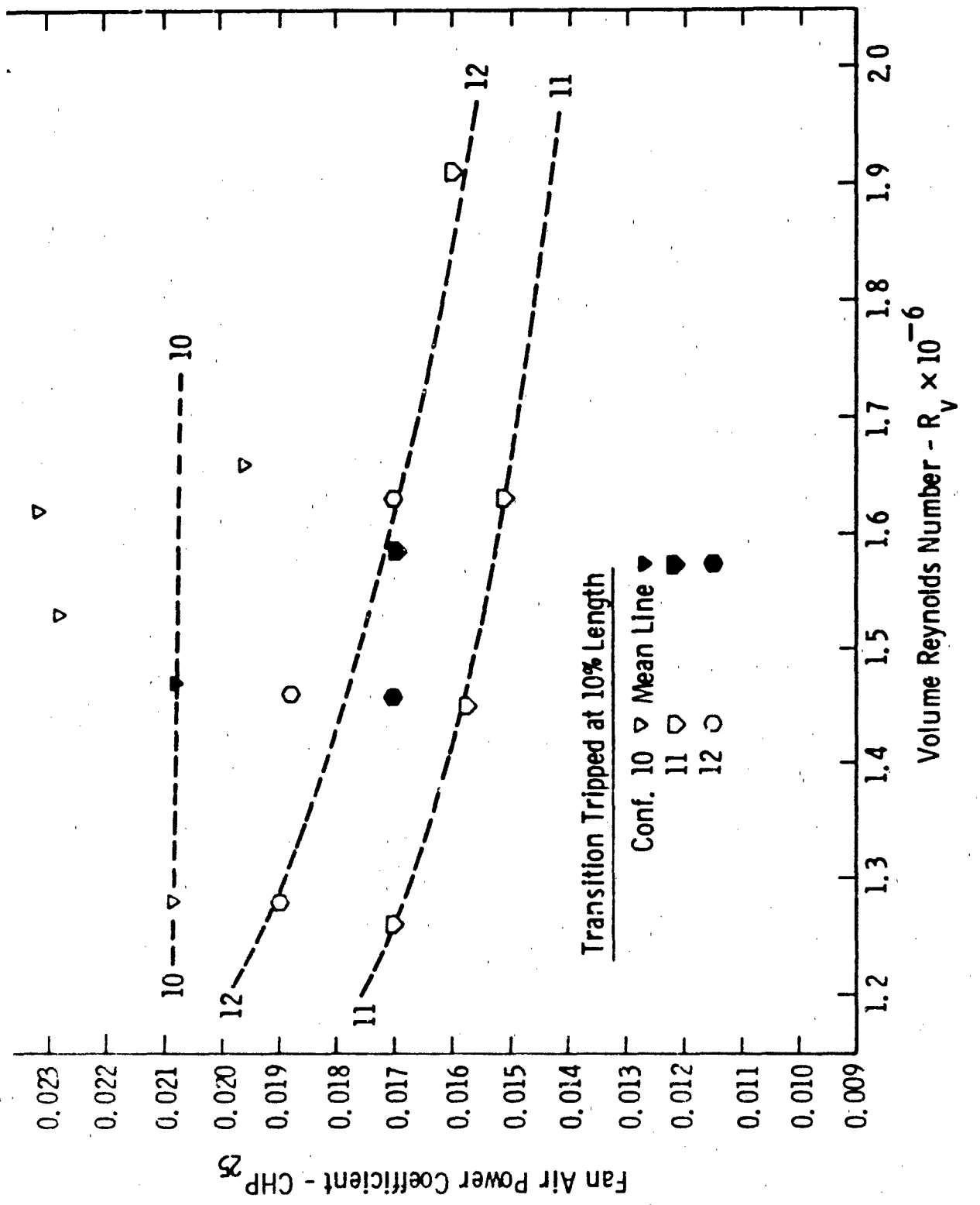


Fig. 31—Fan air power coefficient vs volume Reynolds number - configurations 10, 11, and 12 (transition at 10% length)

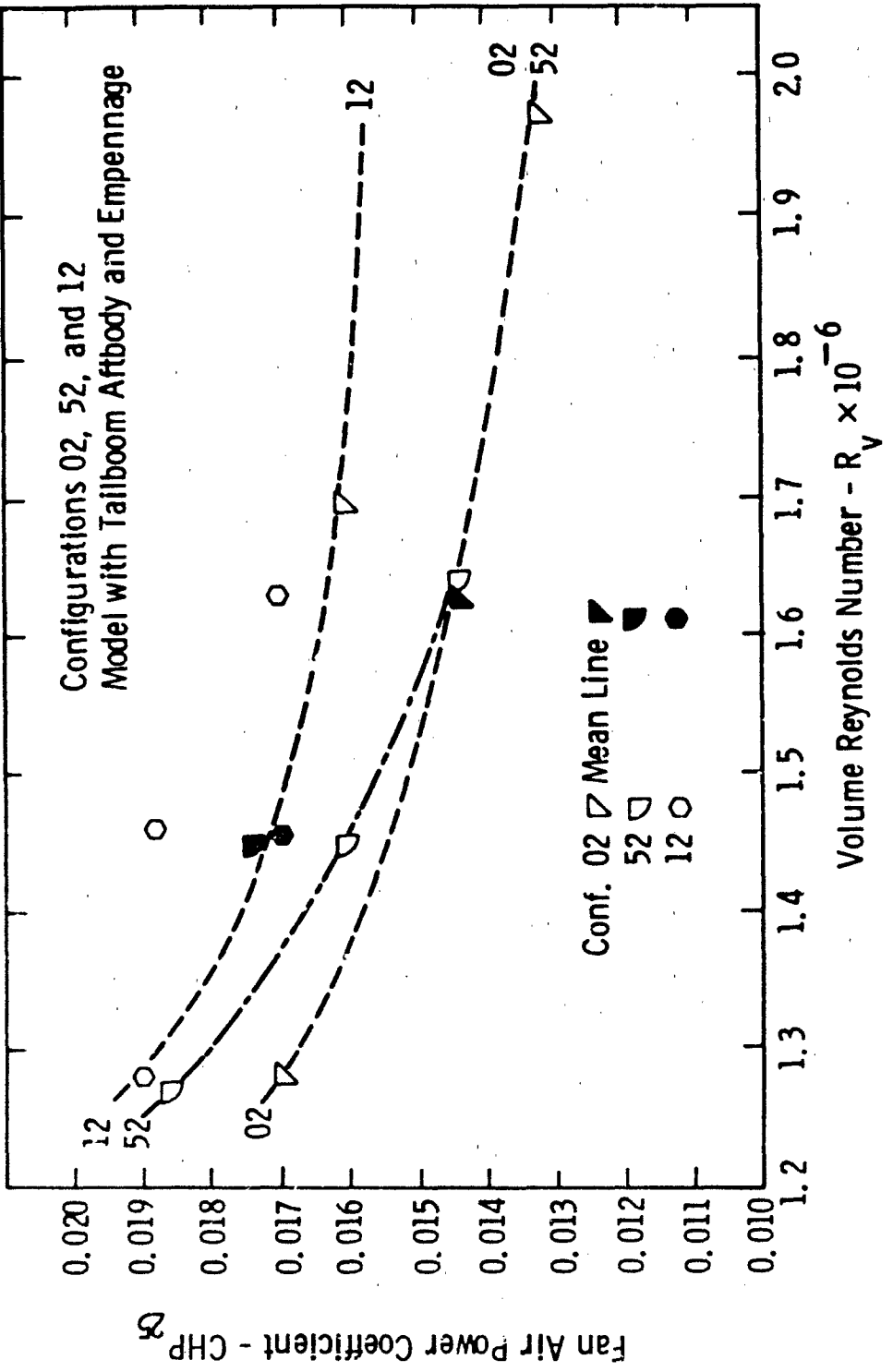


Fig. 32—Fan air power coefficient vs volume Reynolds number - configurations 02, 52 and 12 (model with empennage)

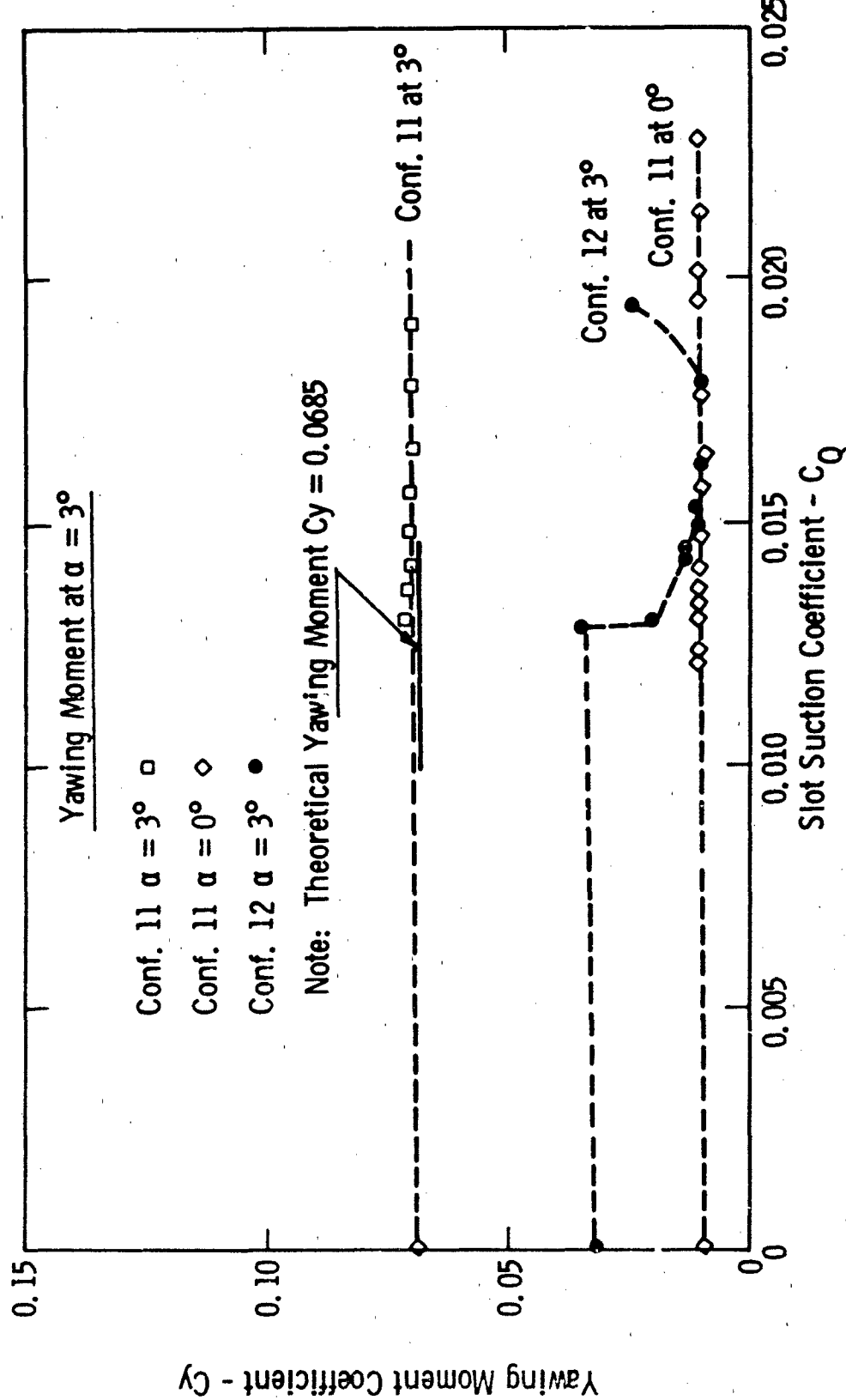


Fig. 33—Correlation of yawing moment coefficient at $\alpha = 3^\circ$ with slot suction coefficient — configurations 11 and 12

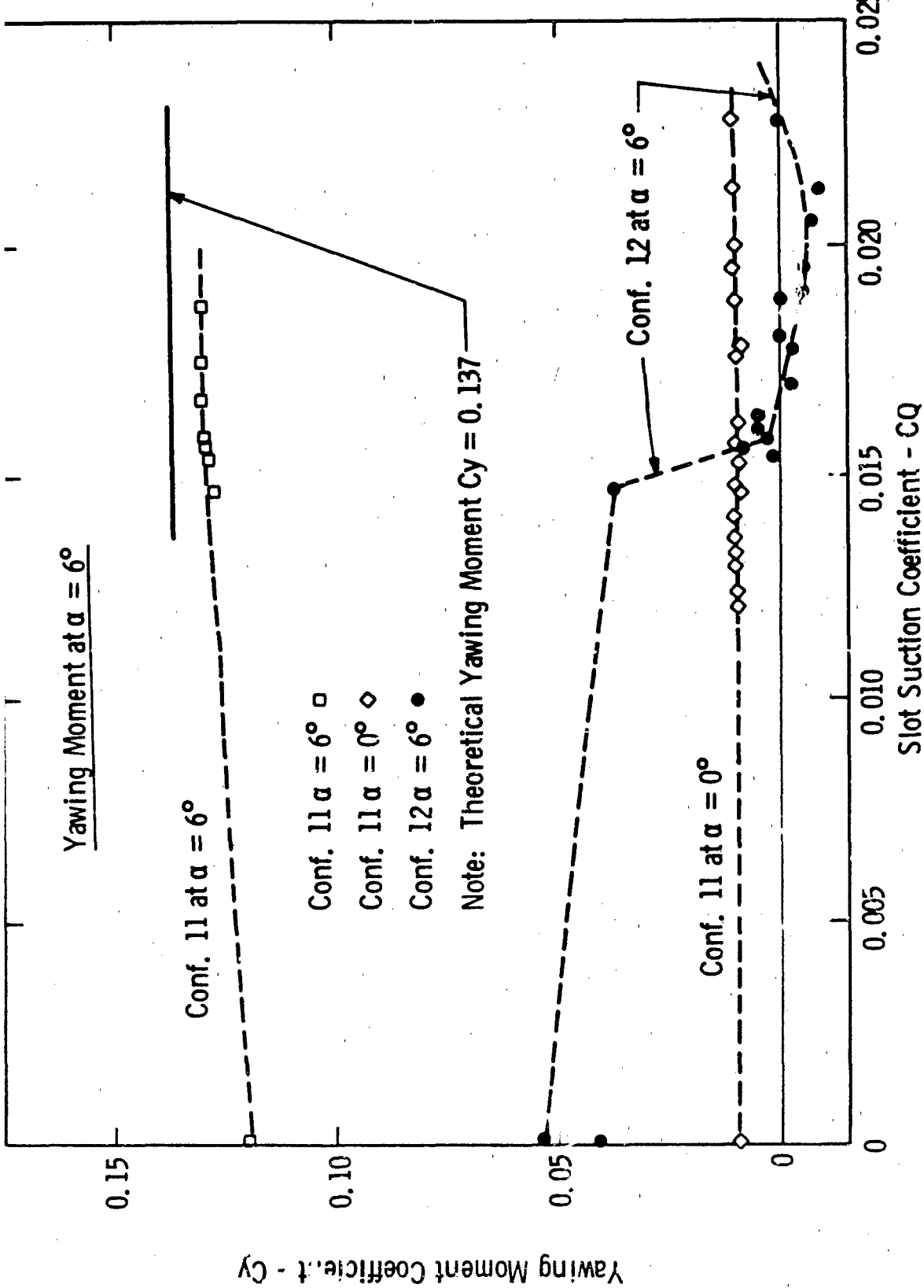


Fig. 34—Correlation of yawing moment coefficient at $\alpha = 6^\circ$ with slot suction coefficient - configurations 11 and 12

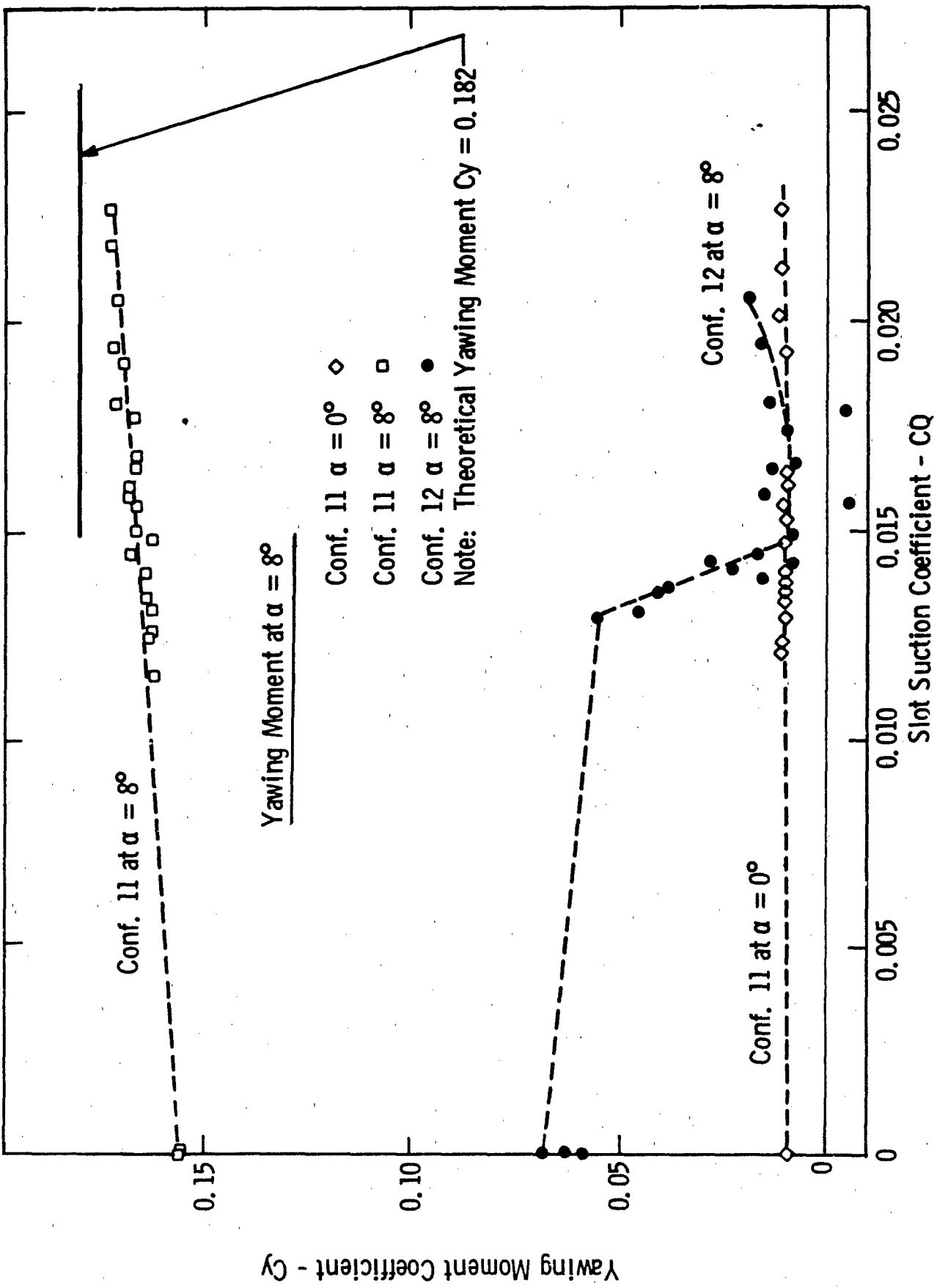


Fig. 35—Correlation of yawing moment coefficient at $\alpha = 8^\circ$ with slot suction coefficient - configurations 11 and 12.

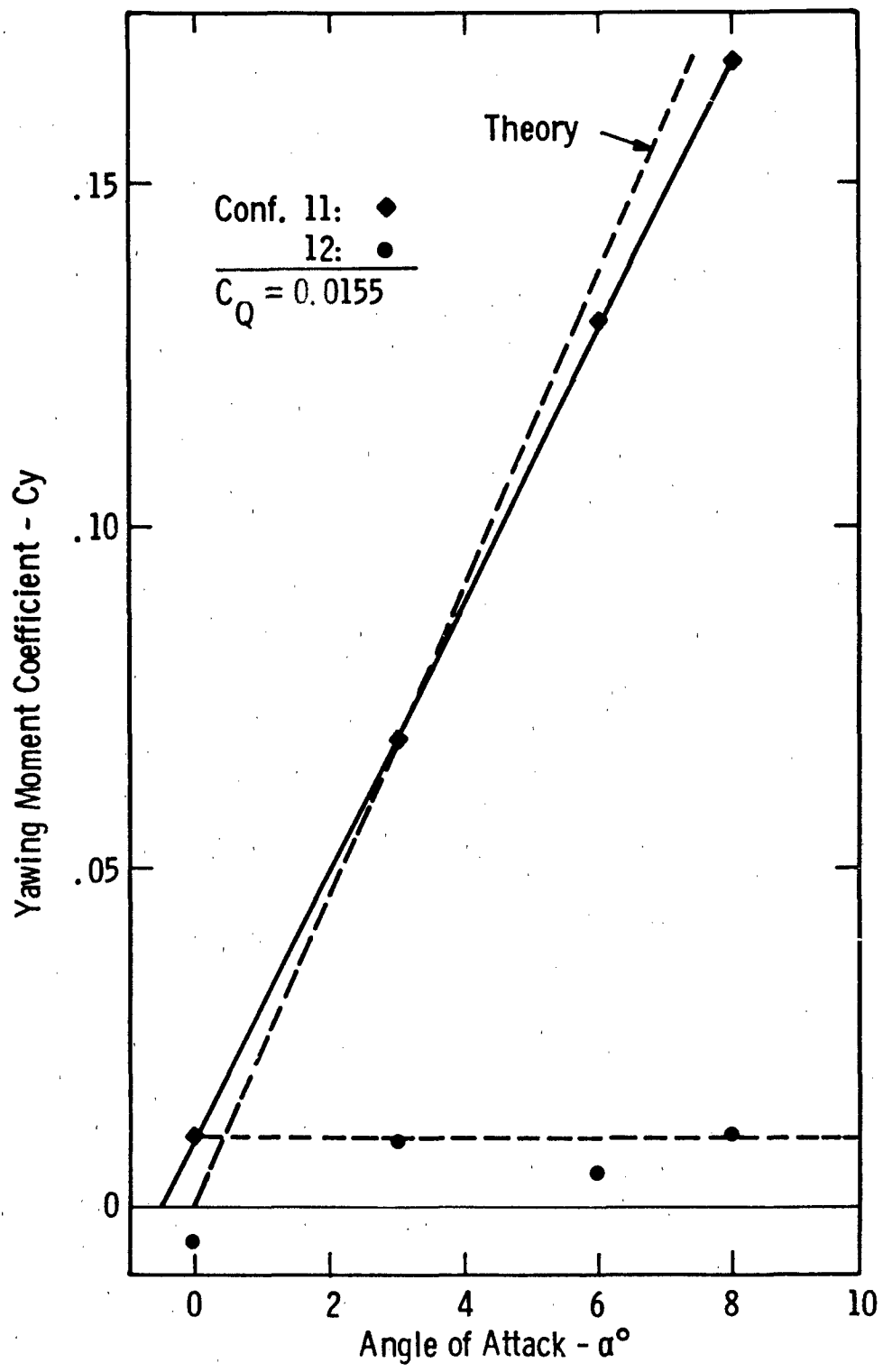


Fig. 36—Correlation of yawing moment coefficient with angle of attack - confs. 11 and 12

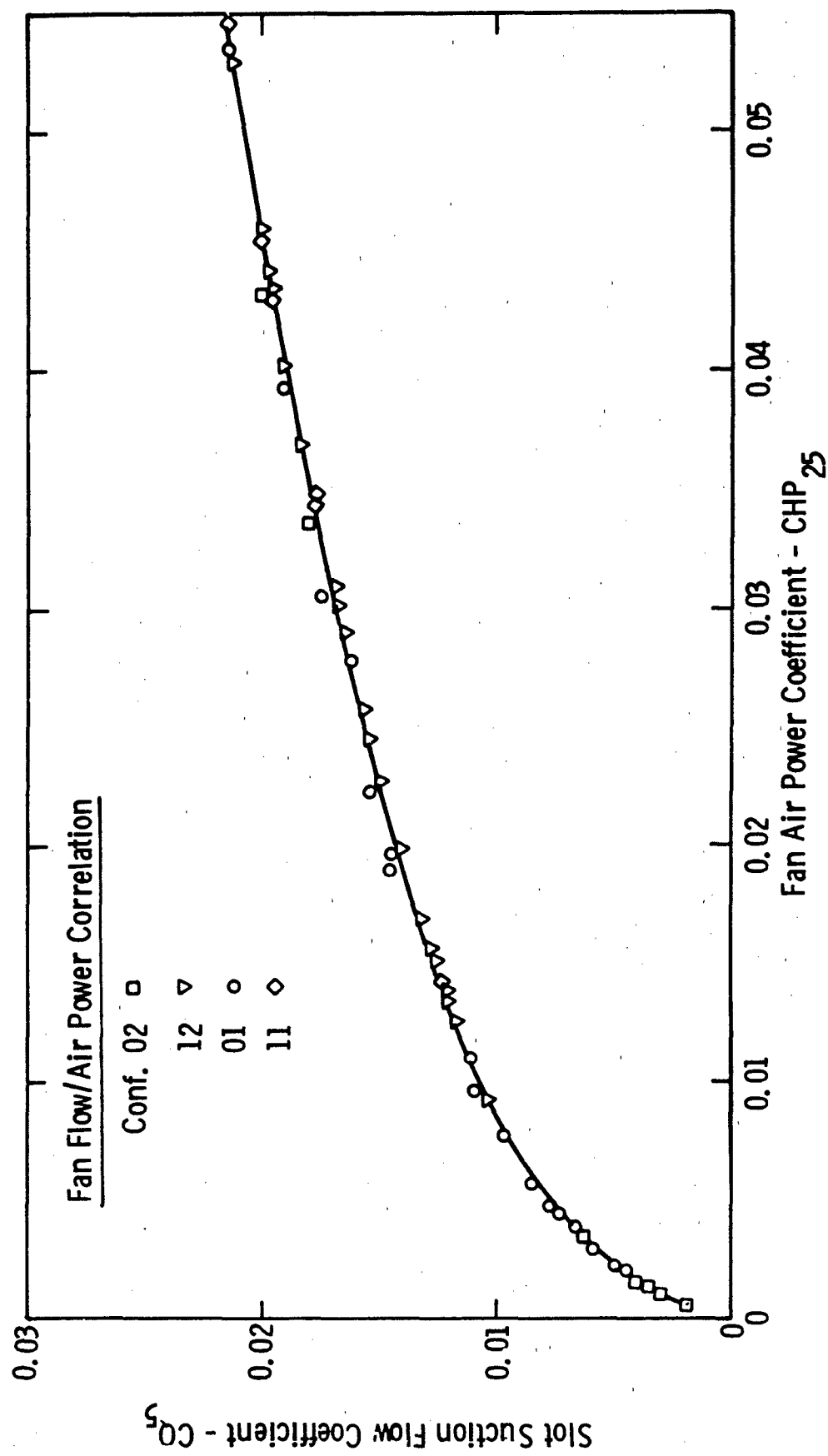


Fig. 37—Correlation of slot suction flow with fan air power

Pressure/Flow Fan System Plot

Conf. 02 □
12 ▽
01 ○
11 ◇

Fan Pressure Rise Coefficient - C_H^{Δ}

- 85 -

0.3

0.025
0.02
0.015
0.01
0.005
0 0

Fig. 38—Correlation of slot suction flow with fan pressure rise

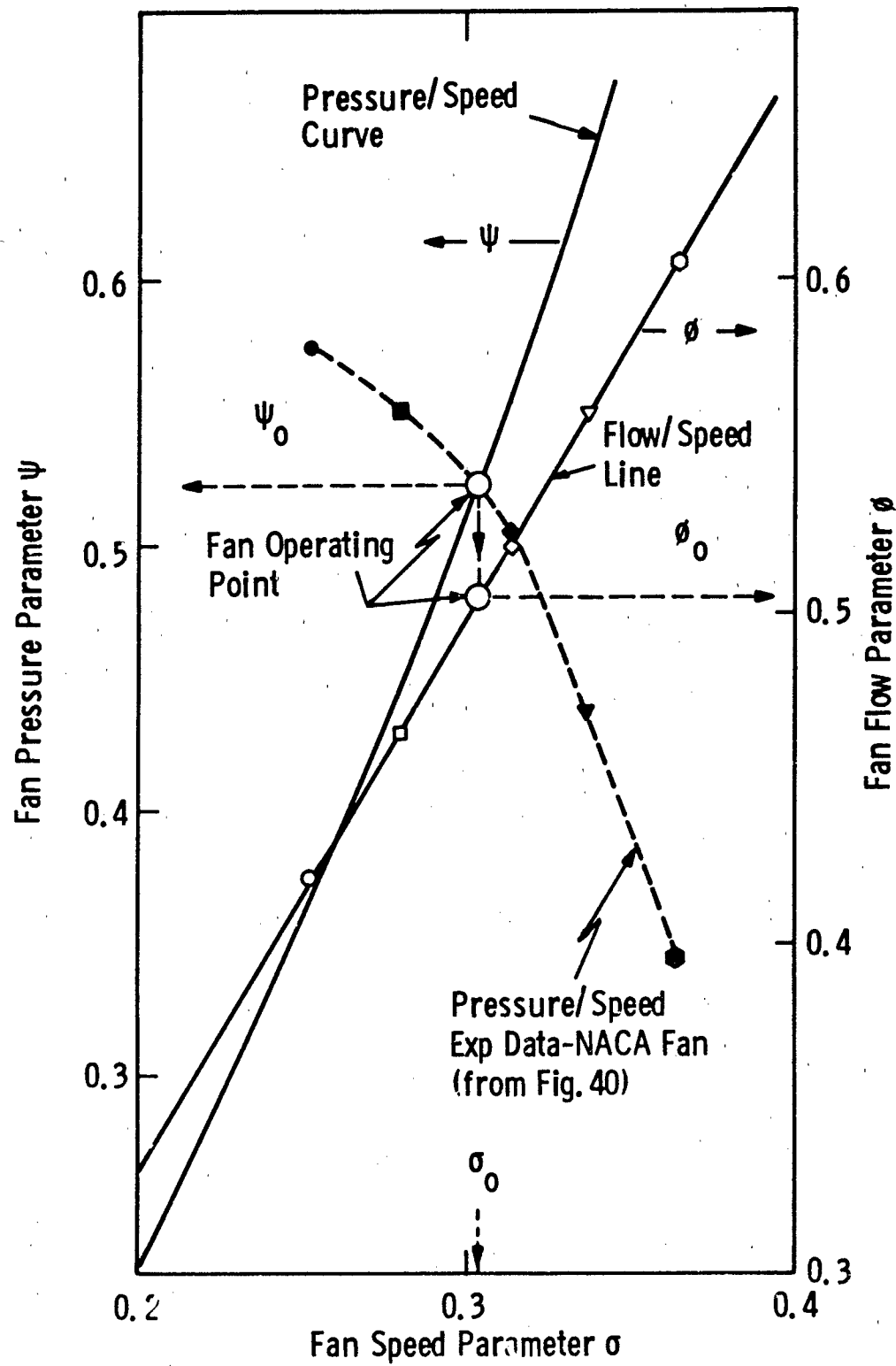


Fig. 39—Chart of fan design parameters - selection of operating point

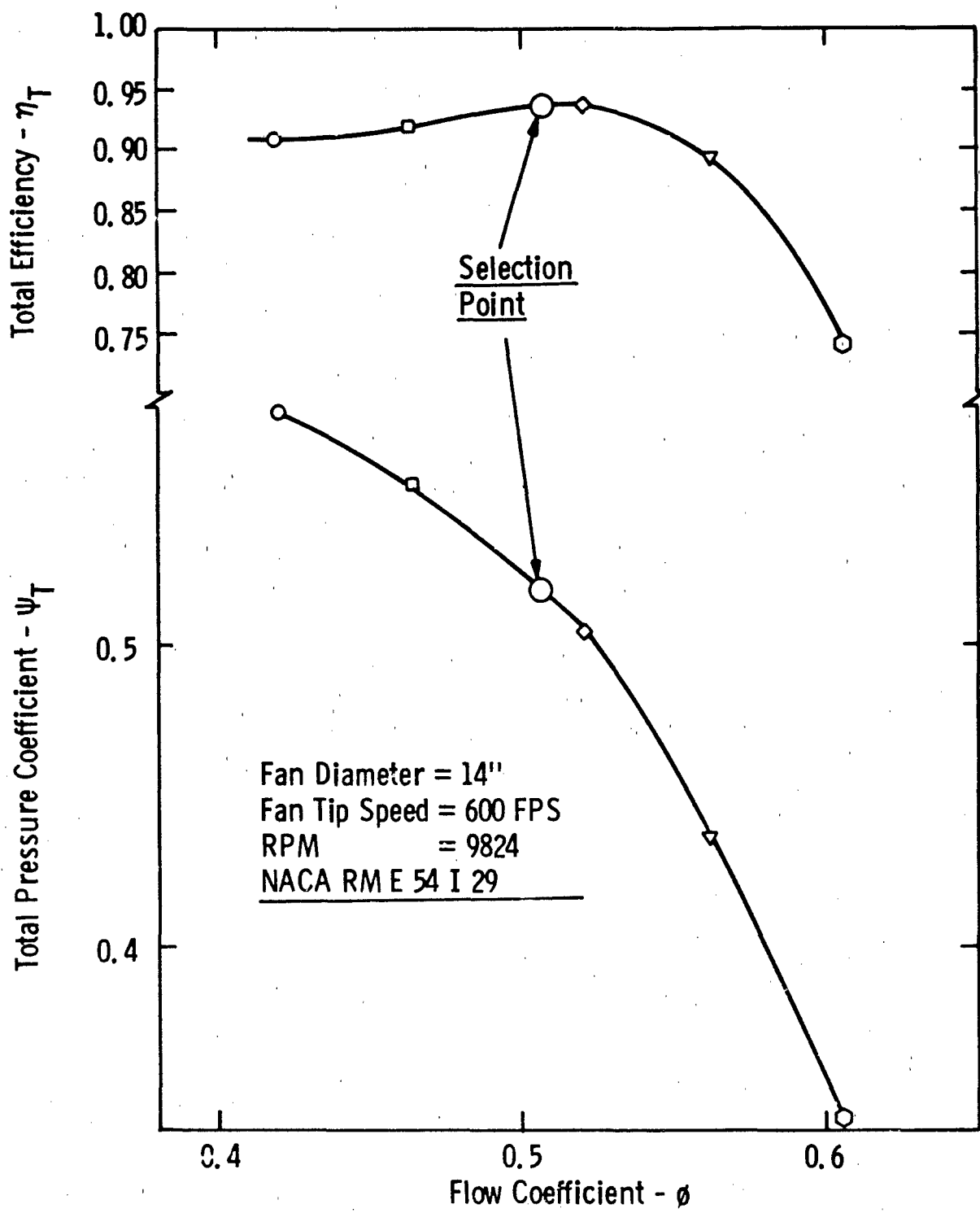


Fig. 40—Experimental performance of NACA axial stage

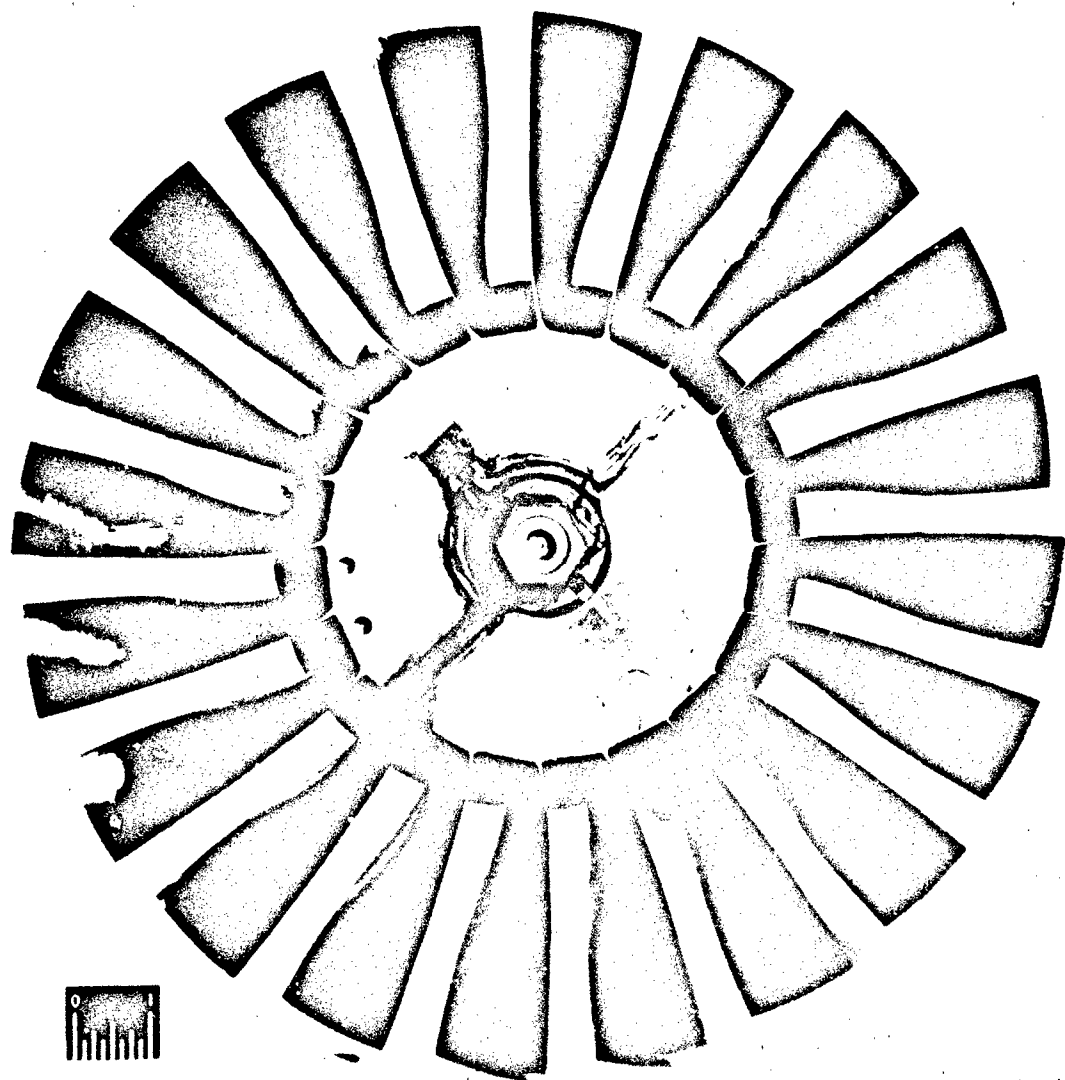


FIG. 41 - PHOTO OF EXPERIMENTAL NACA ROTOR

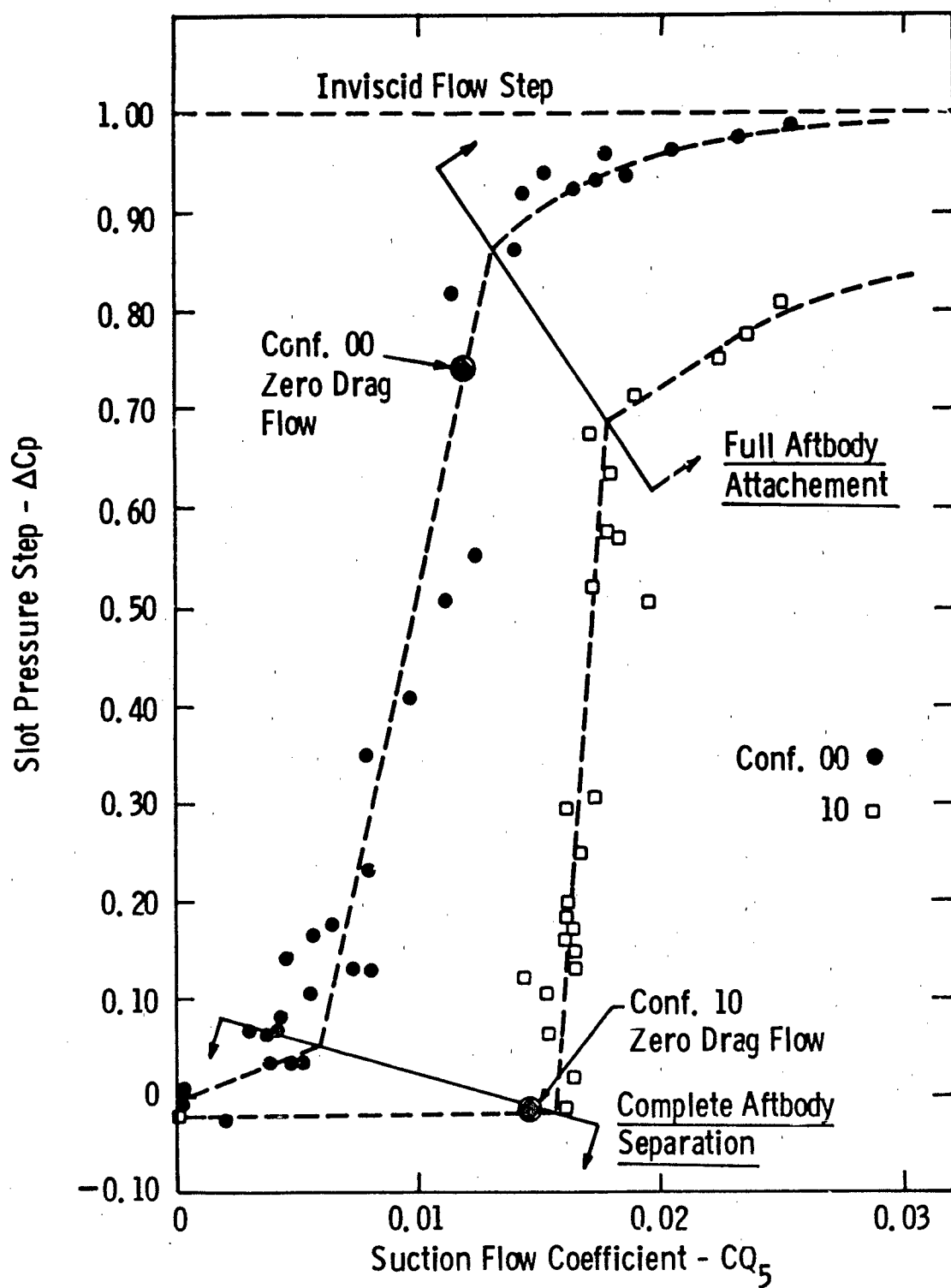


Fig. 42—Correlation of slot pressure-step with suction flow-
configurations 00 and 01

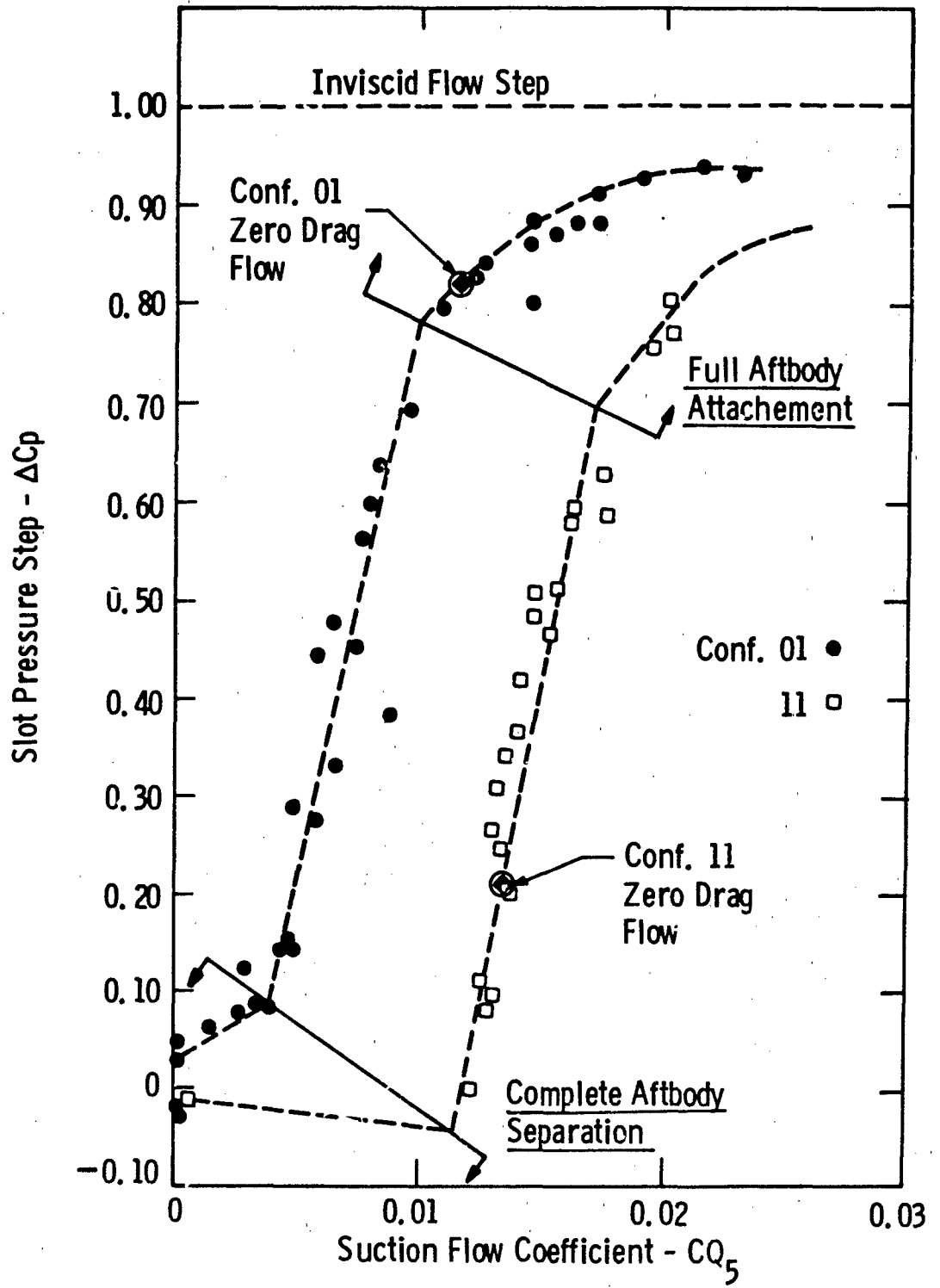


Fig. 43—Correlation of slot pressure-step with suction flow-configurations 01 and 11

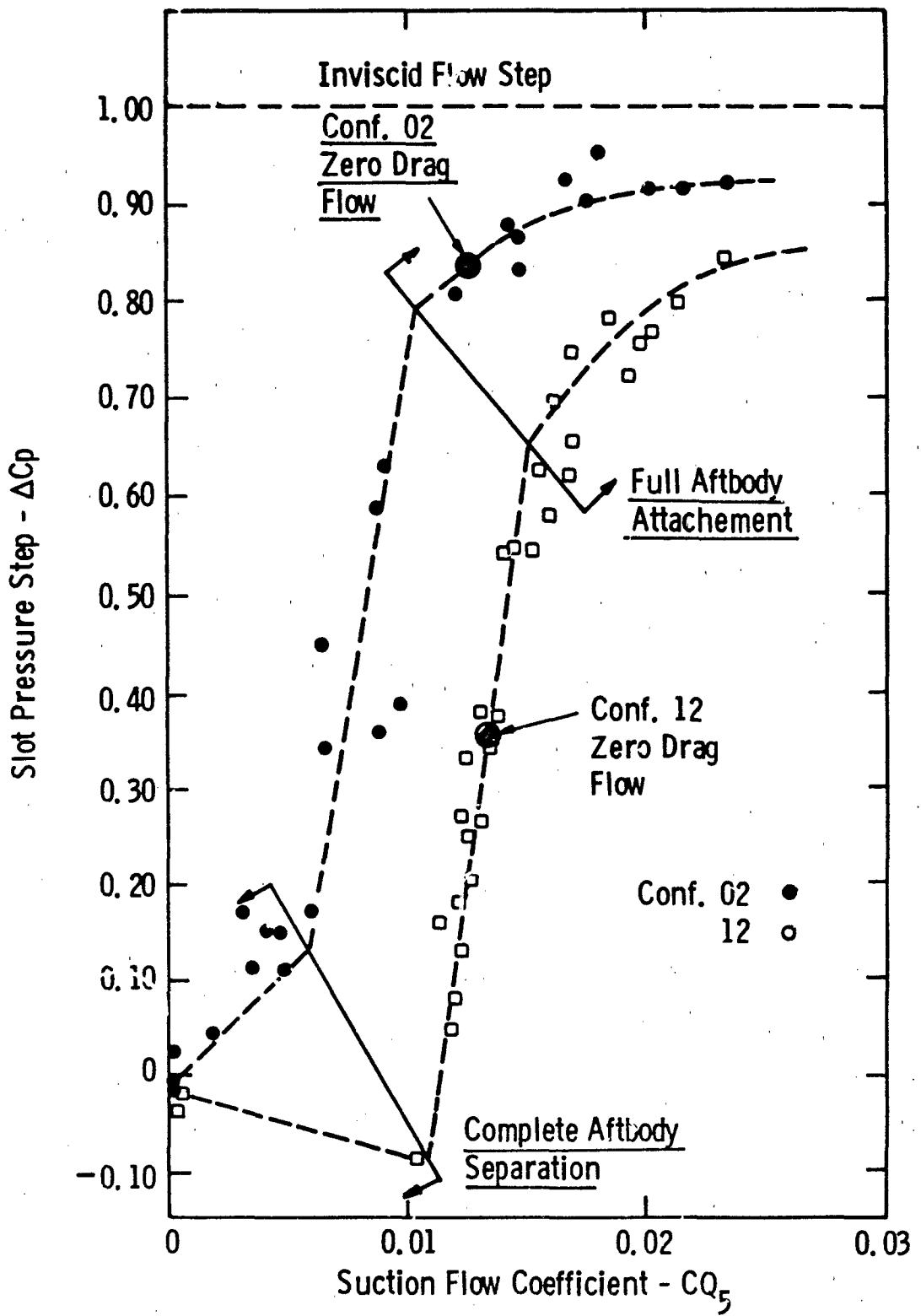


Fig. 44—Correlation of slot pressure-step with suction flow-configurations 02 and 12

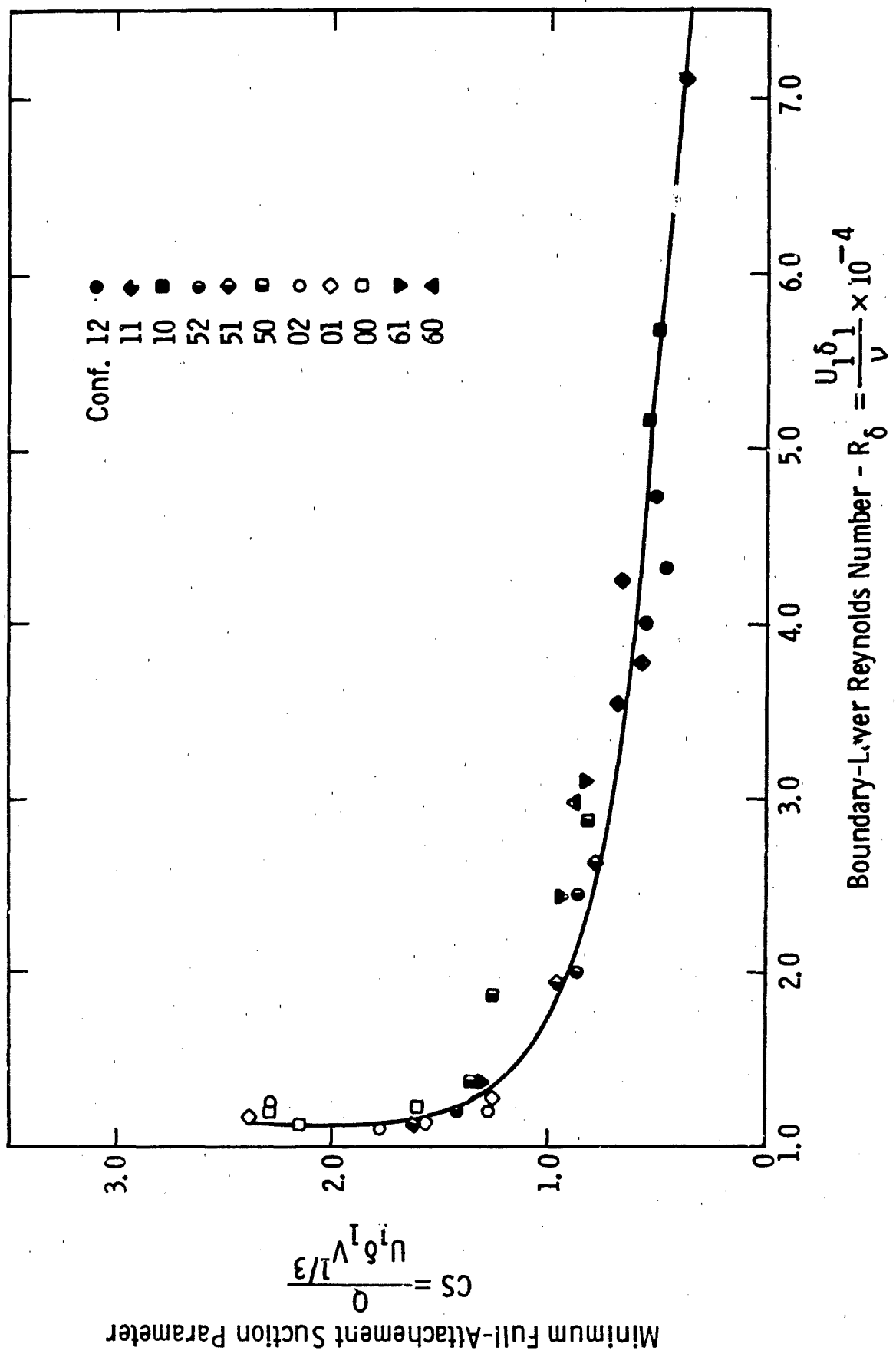


Fig. 45—Correlation of minimum full-attachment suction parameter with boundary-layer Reynolds number

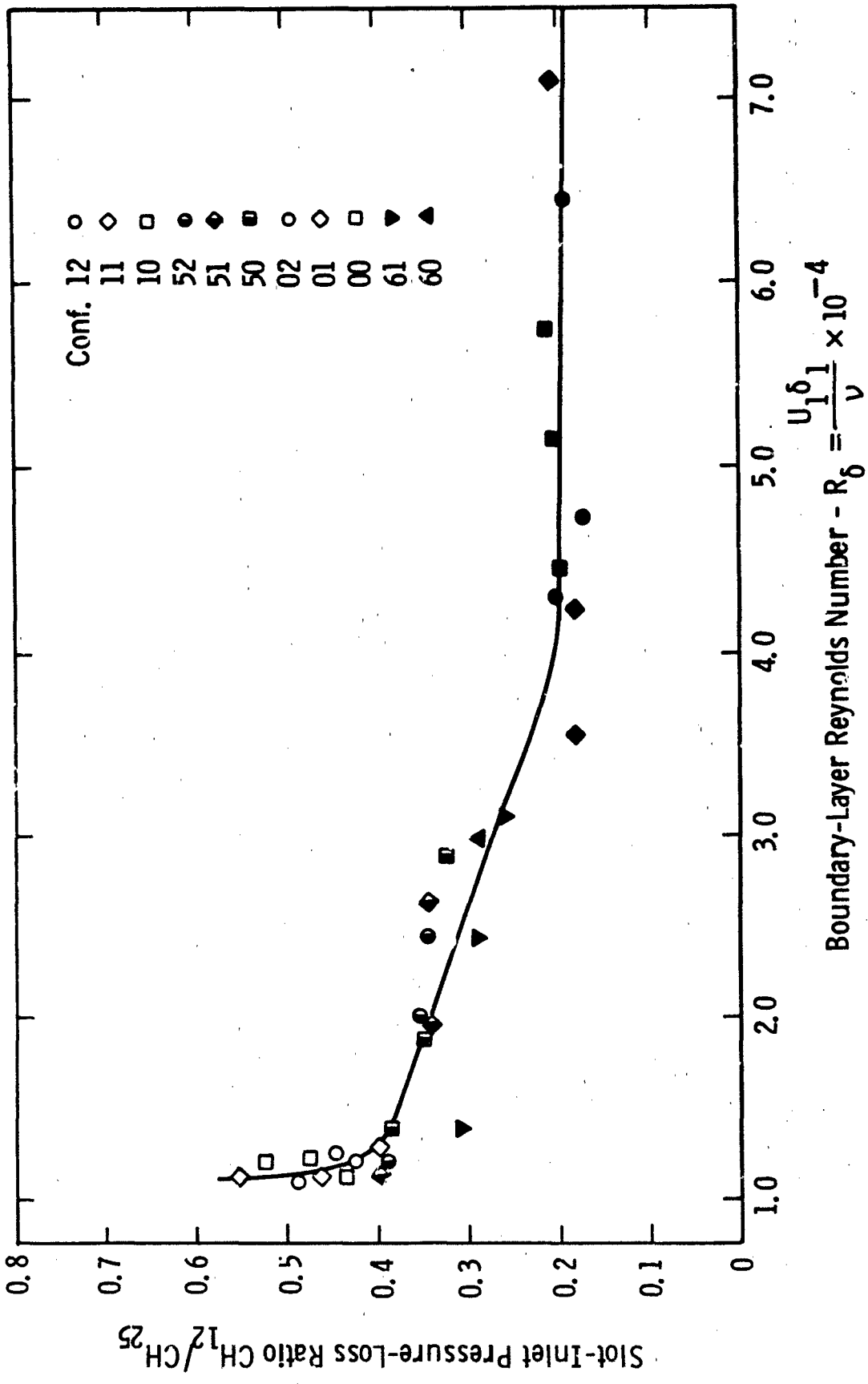


Fig. 46—Correlation of slot-inlet pressure loss ratio at minimum full-attachment suction with boundary-layer Reynolds number

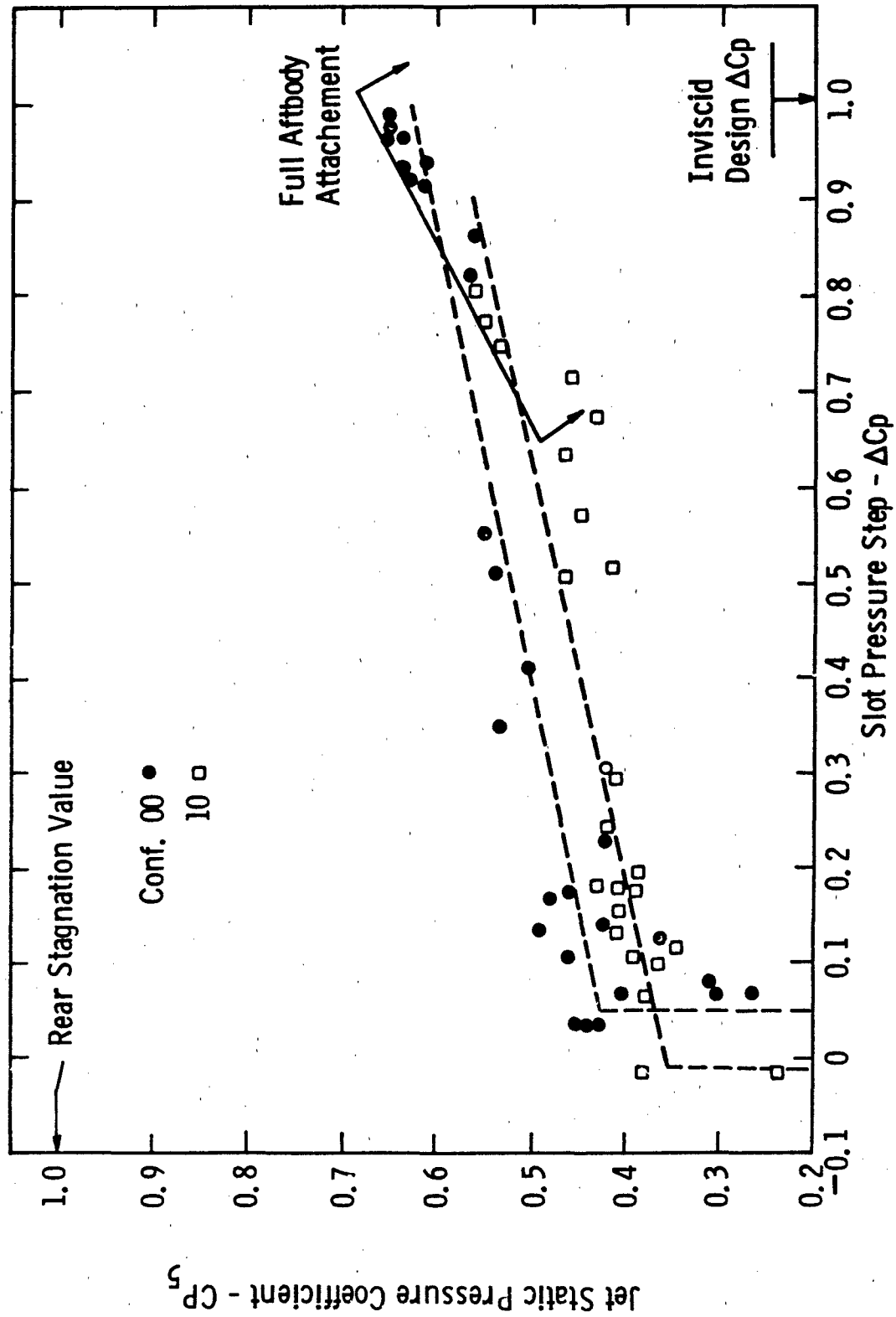


Fig. 47—Correlation of jet static-pressure coefficient with slot pressure step - configurations 00 and 10

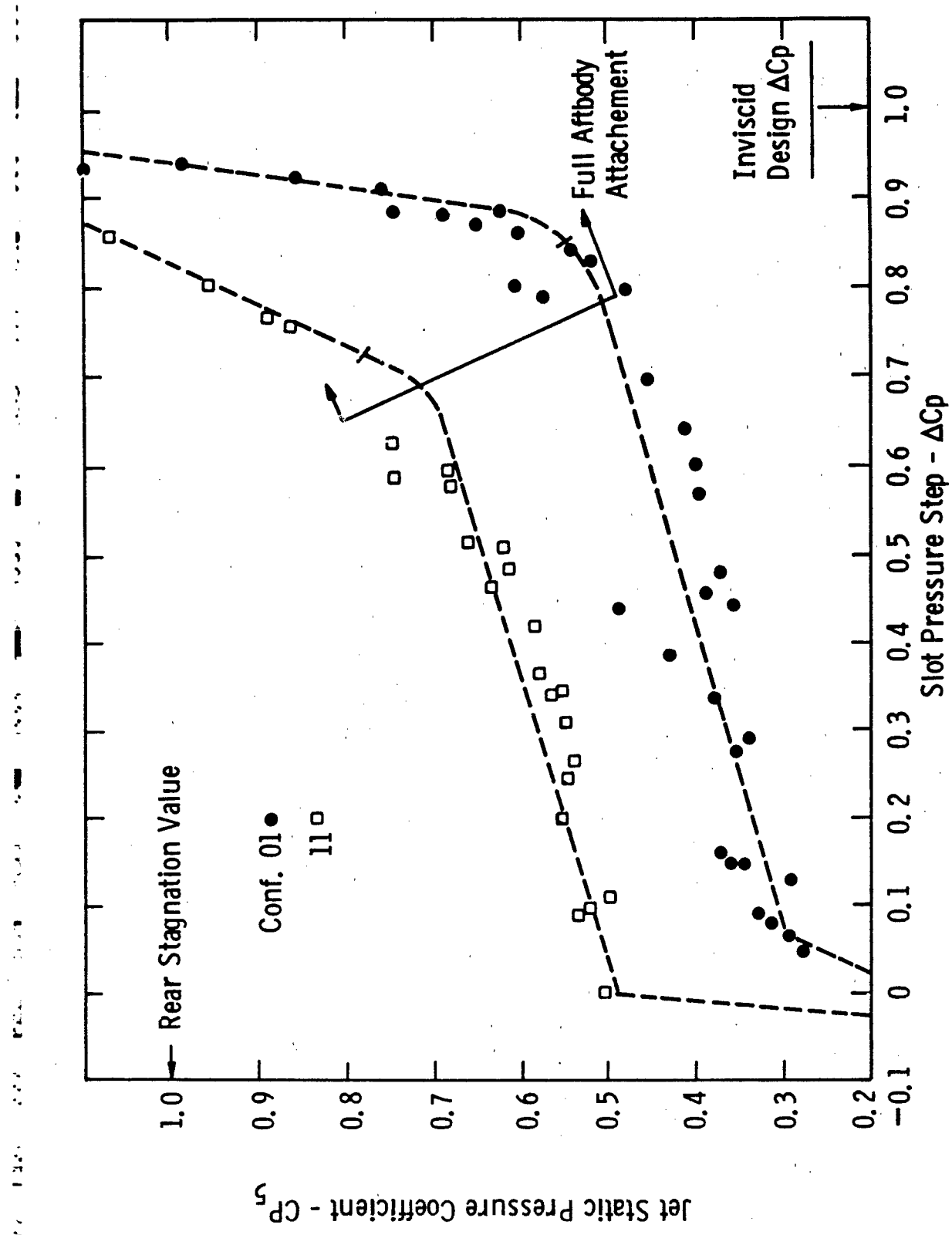


Fig. 48—Correlation of jet static-pressure coefficient with slot pressure step - configurations 01 and 11

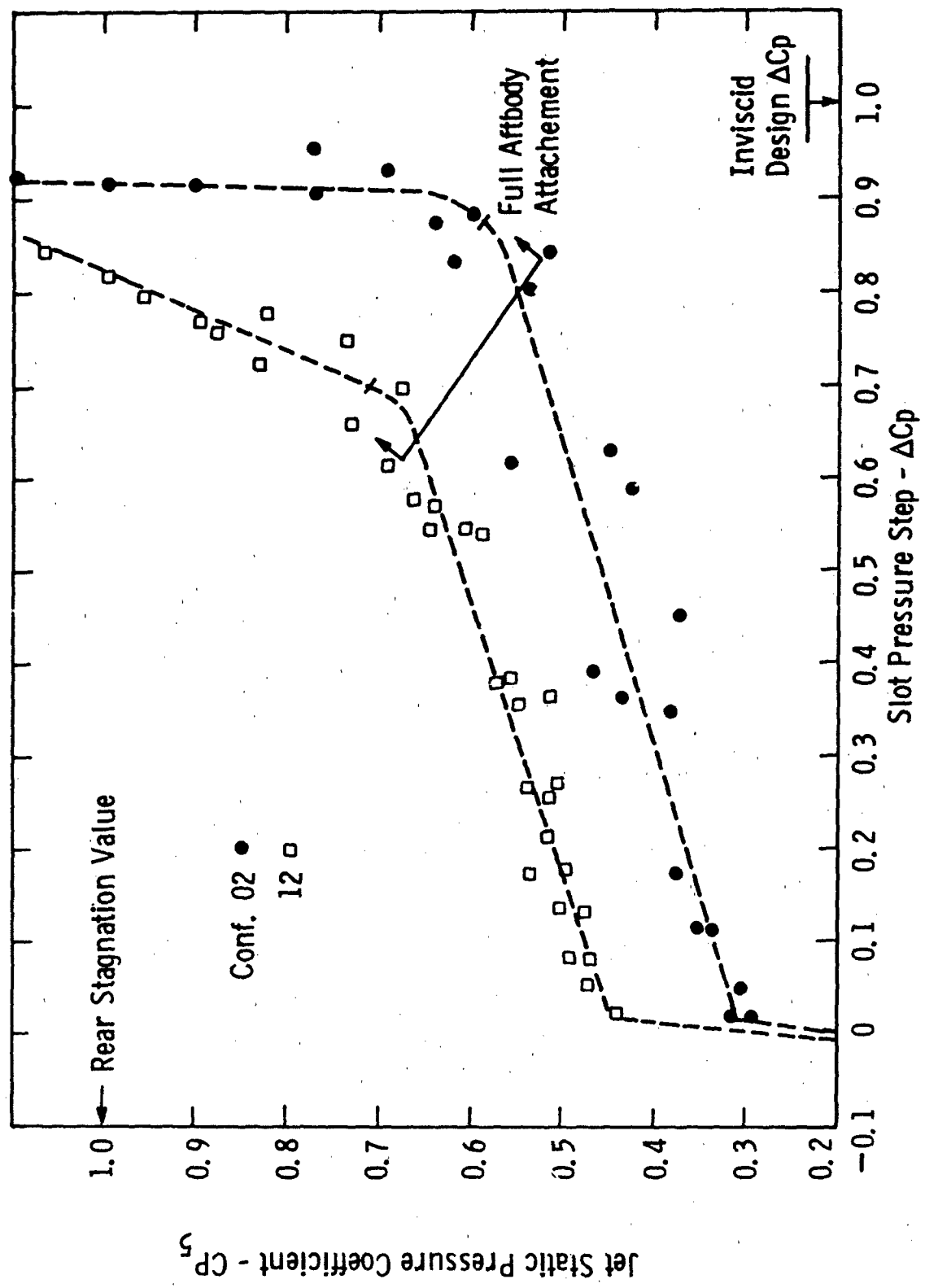


Fig. 49—Correlation of jet static-pressure coefficient with slot pressure step - configurations 02 and 12

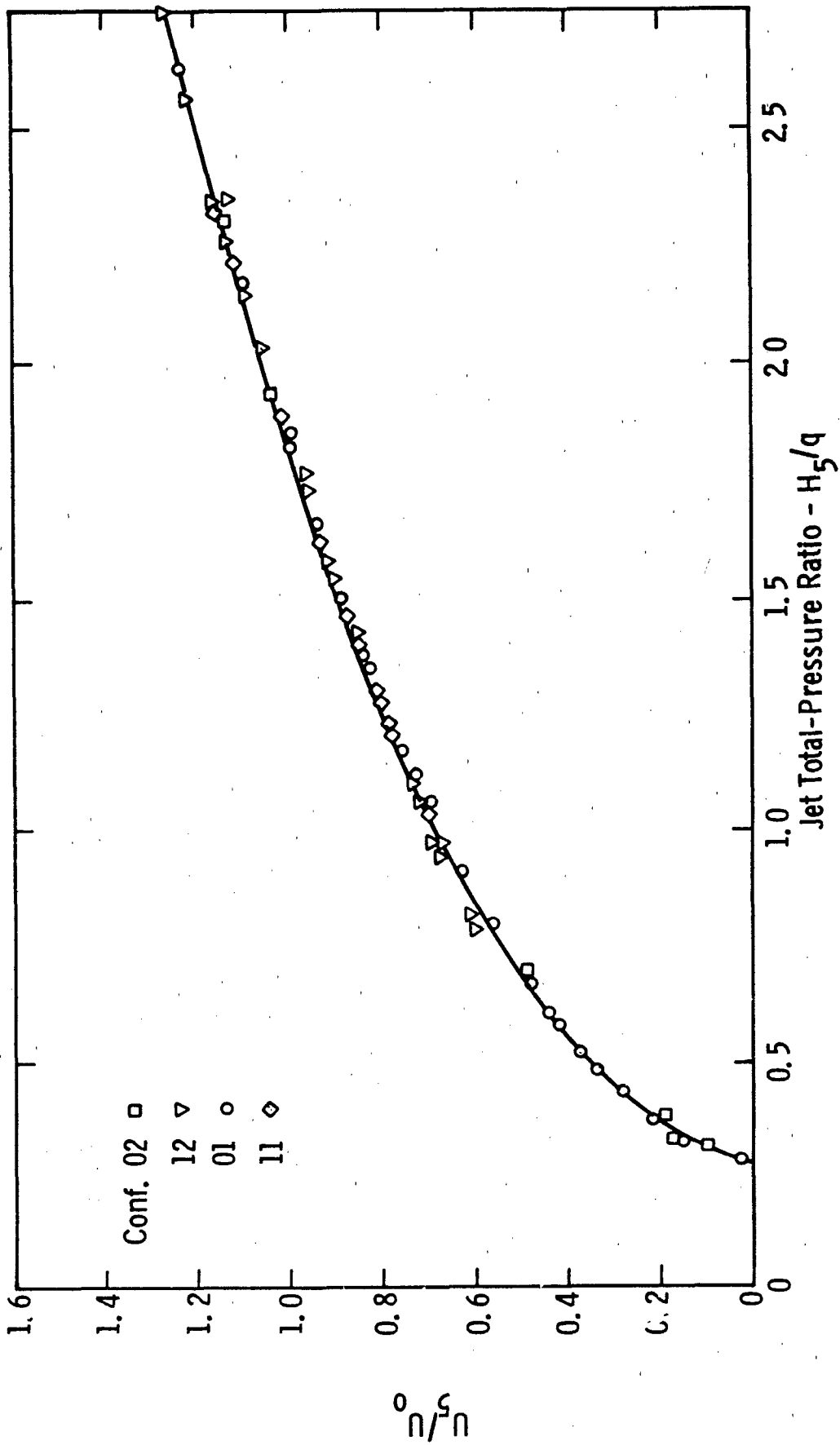


Fig. 50—Correlation of jet velocity-ratio with jet total-pressure ratio - configurations 01, 11, 02 and 12

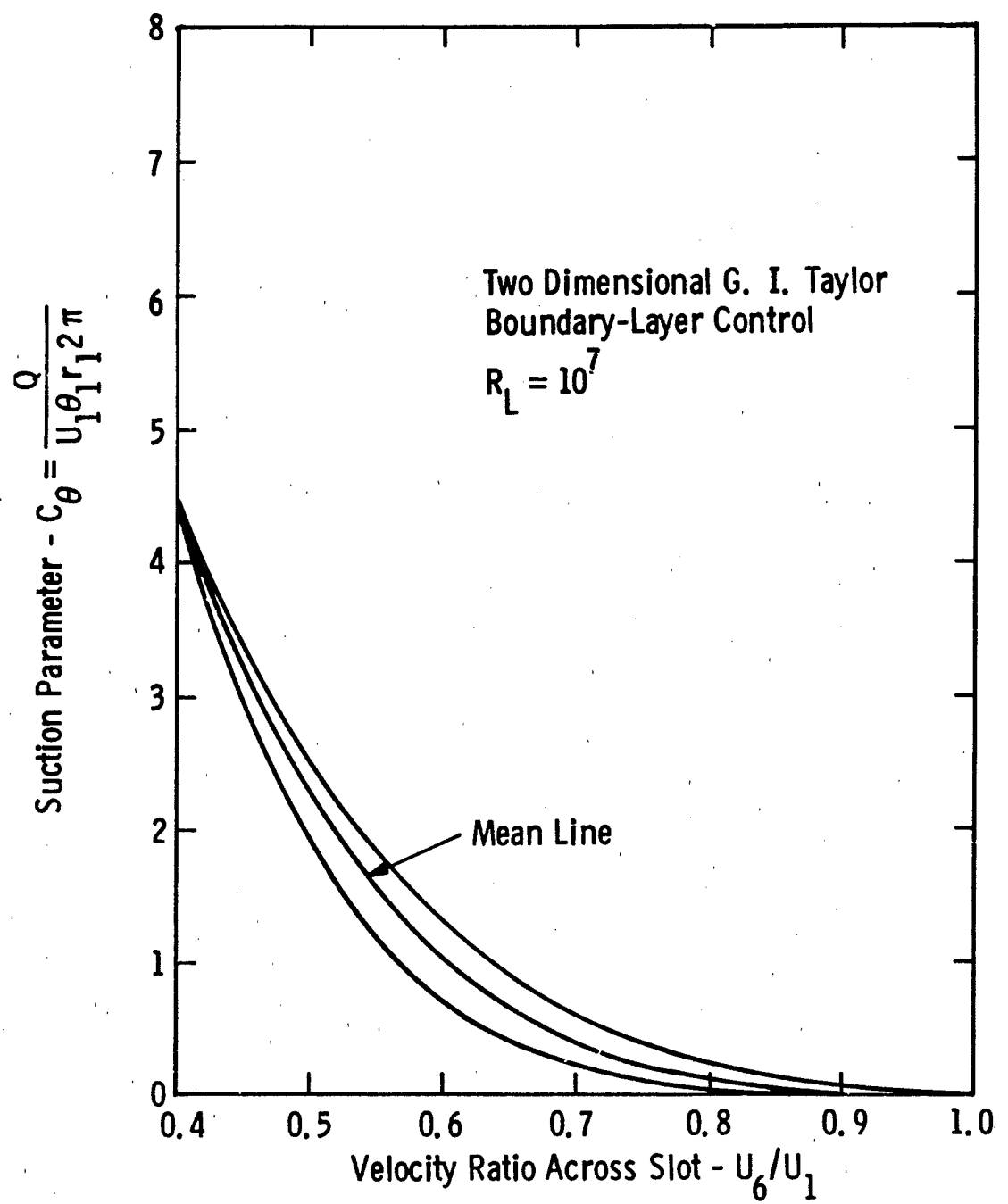


Fig. 51—Plot of boundary-layer control suction parameter vs slot velocity ratio — two-dimensional Taylor theory

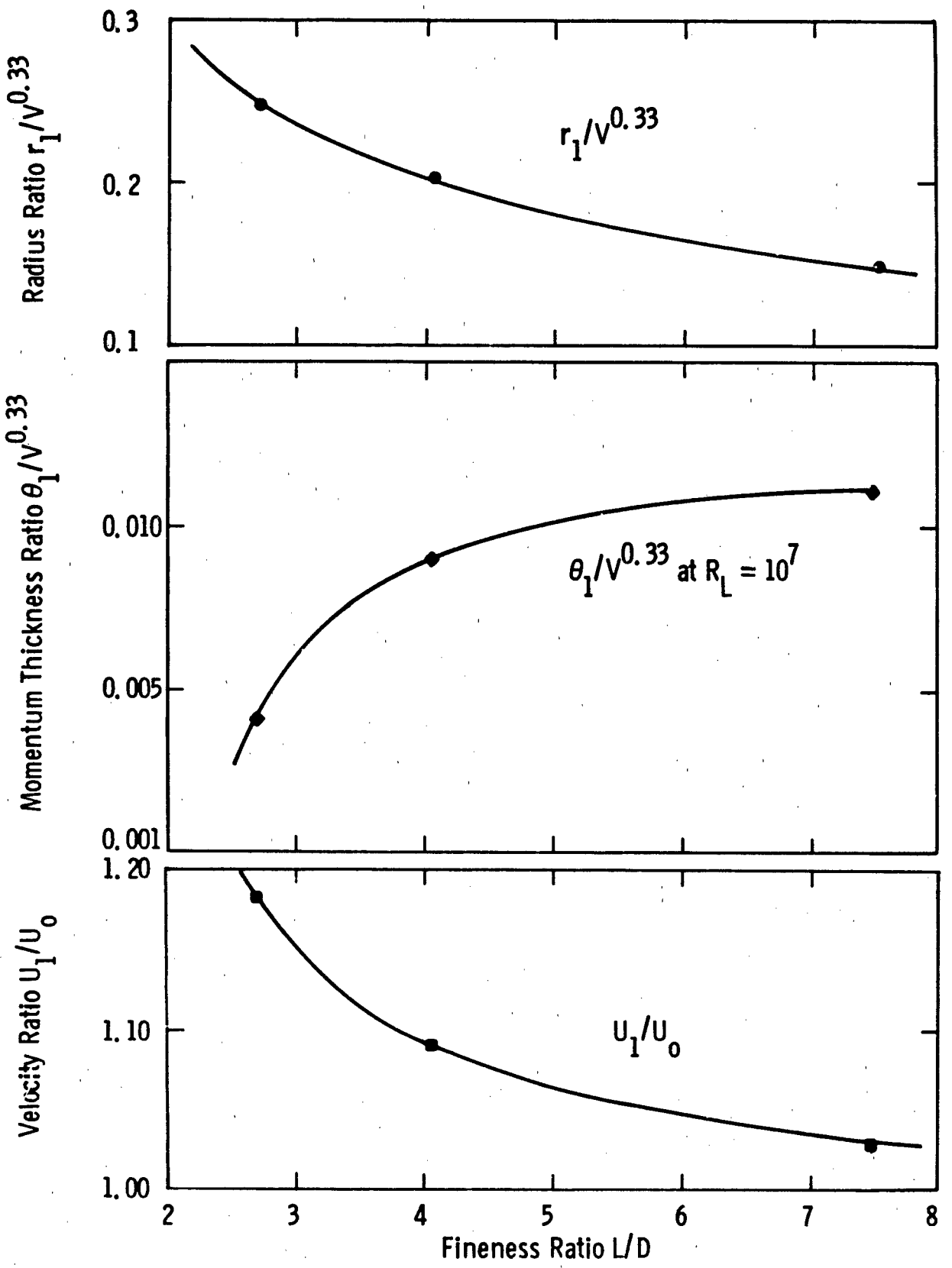


Fig. 52—Correlation of estimated suction parameters with fineness ratio for Reichardt forebodies

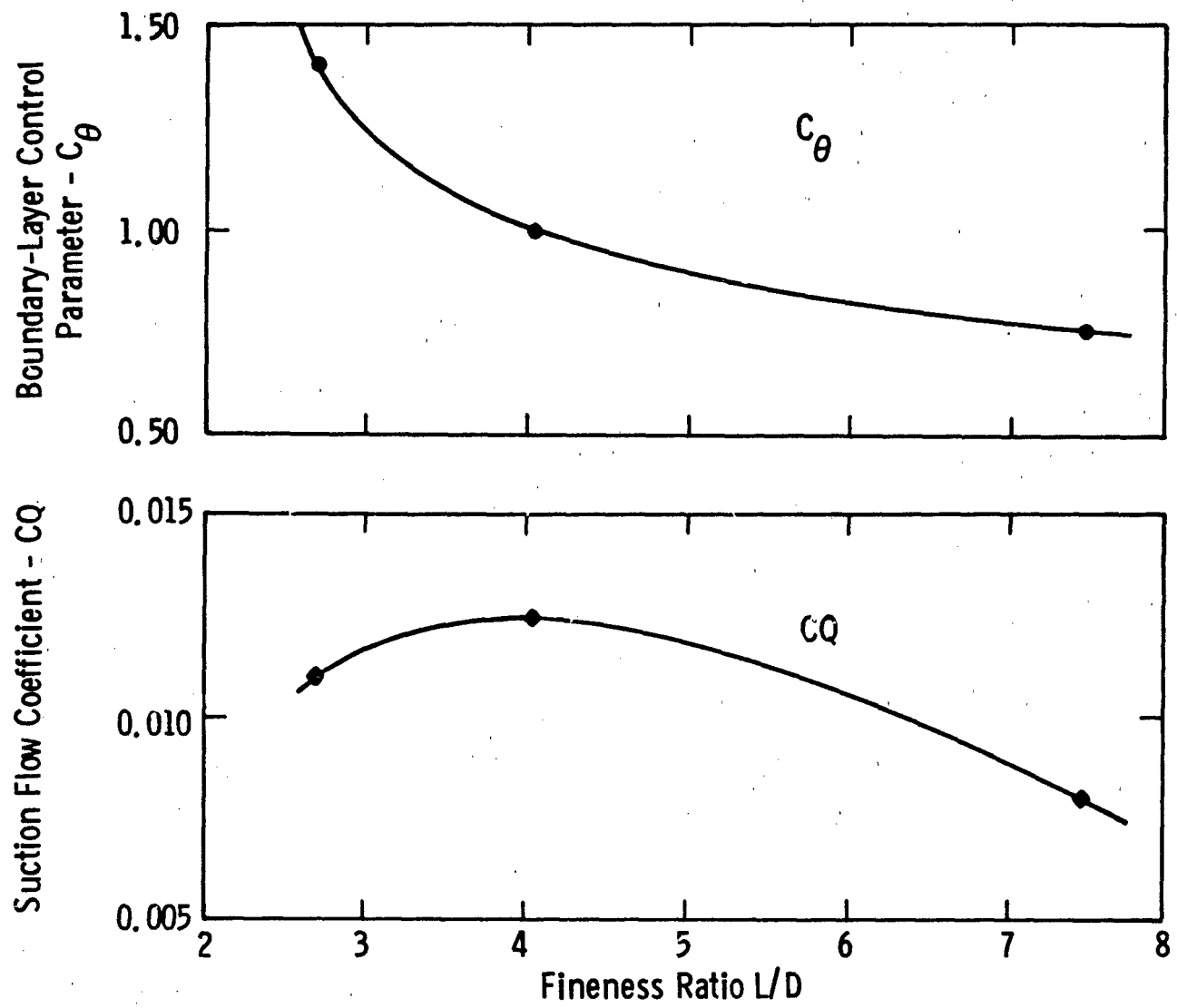


Fig. 53—Correlation of suction and power coefficient with fineness ratio for Reichardt forebodies at $R_L = 10^7$